DEPARTMENT OF PHYSICS
UNIVERSITY OF JYVÄSKYLÄ
RESEARCH REPORT No. 13/2011

STUDIES OF TRANSITION-EDGE SENSOR PHYSICS: THERMAL MODELS AND NOISE

BY
KIMMO KINNUNEN

Academic Dissertation
for the Degree of
Doctor of Philosophy

To be presented, by permission of the
Faculty of Mathematics and Science
of the University of Jyväskylä,
for public examination in Auditorium Kem-1 of the
University of Jyväskylä on December 16, 2011
at 12 o'clock noon

Jyväskylä, Finland
December, 2011

Preface

The work presented in this thesis has been carried out at the Department of Physics and Nanoscience Center at the University of Jyväskylä.

First of all I would like to thank Dr. Arttu Luukanen and my first supervisor, Prof. Jukka Pekola for introducing me to this interesting and challenging topic.

I am deeply grateful to Prof. Ilari Maasilta for later taking on the task of supervising my work, with no prior knowledge of the field. I had some dark times where nothing seemed to work but the patience and support of Prof. Maasilta and the faith in our projects that he showed helped me get through.

A huge thank you goes to the many students (sample slaves) involved in fabrication. Especially Ms. Terhi Hongisto, Mr. Jaakko Leppäniemi, Mr. Antti Nuottajärvi and Mr. Mikko Palosaari, who is hereby officially upgraded into a measurement slave. Antti and Mr. Tarmo Suppula have been invaluable with technical issues and in keeping the Nanoscience Center operational. During these years there have been so many great friends and colleagues in our research group, in NSC and the Physics Department that I cannot list all the names. It has always been pleasant and fun working and/or partying with you all. A big collective thank you to everyone!

I wish to thank everyone at SRON I had the pleasure to collaborate with in the XEUS project. Warm thanks also to Prof. Villy Sundström and Mr. Jens Uhlig at Lund University. I wish you great success in the future with your project.

Financial support from Jenny and Antti Vihuri Foundation, Finnish Cultural Foundation (Central Finland Regional Fund) and The Academy of Finland are gratefully acknowledged.

Finally and most importantly, I want to thank my wife Tuija for support, love, patience and everything and my children Juuso, Niilo and Maisa for keeping my mind off work the few hours a day I have been home lately. Big thanks also to my and Tuijas parents and siblings for helping in so many ways.

Jyväskylä, December 2011

Kimmo Kinnunen

Abstract

Kinnunen, Kimmo
Studies of transition-edge sensor physics: thermal models and noise
Jyväskylä: University of Jyväskylä, 2011
(Research report/Department of Physics, University of Jyväskylä,
ISSN 0075-465X; 13/2011)
ISBN 978-951-39-4588-6
diss.

This thesis focuses on studying the noise in transition-edge sensors (TES). More specifically, the aim is to find an explanation for the observed excess noise that is limiting their performance and has been troubling the TES field in recent years. Several theories have been put forth but a definitive answer is still missing.

In the early stages of this thesis work a novel theory was presented for the noise in a special TES geometry. In our theory the excess noise is caused by correlated fluctuations of superconductivity at the phase boundary between normal and superconducting states. Data from more recent experiments does not give solid support for the theory and in this thesis the validity of the model is discussed.

Measurements of the complex impedance of TES detectors have shown that the thermal circuit of a TES can be complicated and imply the presence of noise caused by internal thermal fluctuations. The thermal circuit can be presented by a block model and in this thesis we try to identify the simplest model that can explain all the measured impedance and noise data. The determination of the thermal model depends on the interpretation of the complex impedance data. The measurement setup has a limited bandwidth and often the TES impedance is such that it is difficult to find the correct high frequency limit of impedance, which is an important parameter. In this work a method was developed that could be used to extract the needed information from DC data only.

We have shown that a three-block thermal model is often sufficient for our data. One of the blocks was identified as originating from the underlying SiN membrane that is used for thermal isolation of the TES. The main result of this thesis is the identification of the other two blocks. These are the normal and superconducting phases inside the TES. According to our model, the observed excess noise arises

from the finite thermal conductance between the two phases, which means that the superconducting part will decouple thermally from the normal part at high frequencies. Our data also shows that the jump in heat capacity at the critical temperature as predicted by the BCS theory may be reduced in thin bilayer films. We discuss possible design choices that could minimize the noise due to the N-S decoupling.

Keywords Transition-edge, detector, noise, impedance, thermal model, x-ray

Author's address Kimmo Kinnunen
Department of Physics
Nanoscience Center
University of Jyväskylä
Finland

Supervisor Professor Ilari Maasilta
Department of Physics
Nanoscience Center
University of Jyväskylä
Finland

Reviewers Dr. Mark Lindeman
SRON Netherlands Institute for Space Research
Utrecht
The Netherlands

Dr. Mika Prunnila
Technical Research Centre of Finland
VTT
Finland

Opponent Dr. Kent Irwin
National Institute of Standards and Technology
Boulder, Colorado
USA

List of Publications

The main results of this thesis have been reported in the following articles:

A.I. A. LUUKANEN, K.M. KINNUNEN, A.K. NUOTTAJÄRVI, H.F.C. HOEVERS, W.M. BERGMANN TIEST AND J.P. PEKOLA, *Fluctuation-Limited Noise in a Superconducting Transition-Edge Sensor*. Phys. Rev. Lett. **90** 238306 (2003).

A.II. K.M. KINNUNEN, A.K. NUOTTAJÄRVI, J. LEPPÄNIEMI AND I.J. MAASILTA, *Reducing Excess Noise in Au/Ti Transition-Edge Sensors* . J. Low Temp. Phys. **151** (2008) 119-124.

A.III. K.M. KINNUNEN, A.K. NUOTTAJÄRVI AND I.J. MAASILTA, *A Transition-Edge Sensor with Two Excess Noise Mechanisms*. J. Low Temp. Phys. **151** (2008) 144-149.

A.IV. I.J. MAASILTA AND K.M. KINNUNEN, *New analysis method for I-V and complex impedance data of transition-edge sensors*. AIP Conf. Proc. **1185** 38 (2009). Note: the published version has an error in the given equations. A corrected version is included with this thesis.

A.V. M.R.J. PALOSAARI, K.M. KINNUNEN, M.L. RIDDER, J. VAN DER KUUR, H.F.C. HOEVERS AND I.J. MAASILTA, *Analysis of impedance and noise data of an X-ray transition-edge sensor using complex thermal models*. J. low Temp. Phys, in press, arXiv:1112.0400v1.

A.VI. K.M. KINNUNEN, M.R.J. PALOSAARI AND I.J. MAASILTA, *Effect of a thin AlOx layer on transition-edge sensor properties*. J. low Temp. Phys, in press, arXiv:1112.2342v1.

A.VII. K.M. KINNUNEN, M.R.J. PALOSAARI AND I.J. MAASILTA, *Normal metal - superconductor decoupling as a source of thermal fluctuation noise in transition-edge sensors* . Submitted for publication, arXiv:1111.4098v1 .

Author's contribution

The author of this thesis has written articles A.III, A.VI and the first draft of A.VII. The author participated in writing A.II, A.IV and A.V. The author had a contribution in characterizing the samples for A.I and participated in discussions that lead to the published theory. The author has developed and built the SQUID readout setup used in A.II-A.VII. The author has measured all of the data in A.II-A.VII. The author has written the computer codes used in data analysis of A.III-A.V and A.VII. The data analysis in A.II and A.V was partly done by the author, and in A.III, A.IV, A.VI and A.VII the author is responsible for all analysis. The author was actively involved in developing the method and derivation of equations for A.IV.

Other publications to which the author has contributed

B.I. K. KINNUNEN, A. NUOTTAJÄRVI, S. PÖYHÖNEN, J. PEKOLA, A. LUUKANEN, H. SIPILÄ, I. SUNI, J. SALMI, H. SEPPÄ AND M. KIVIRANTA, *Sub-Kelvin current amplifier using a DC-SQUID*. Physica B **284-288** (2000) 2117-2118.

B.II. A. LUUKANEN, H. SIPILÄ, K. KINNUNEN, A. NUOTTAJÄRVI AND J. PEKOLA, *Transition-edge microcalorimeters for X-ray space applications* . Physica B **284-288** (2000) 2133-2134 .

B.III. J. PENTTILÄ, A. VIRTANEN, M. NEVALA, K. KINNUNEN, A. LUUKANEN, J. HASSEL, M. KIVIRANTA, P. HELISTÖ, I. MAASILTA AND H. SEPPÄ , *Development of SQUID amplifier and ac-biased bolometer for detection of sub-mm radiation*. URSI/IEEE XXIX Convention on Radio Science, ed. Manu Lahdes, VTT Symposium 235, pp. 139-142, Espoo (2004).

B.IV. I.J. MAASILTA, K.M. KINNUNEN, A.K. NUOTTAJÄRVI, T.I. SUPPULA AND A. LUUKANEN , *Optimizing the operation of transition edge sensors*. in Proceedings of the 6th European Workshop on Low Temperature Electronics, ESA publication WPP-227 (2004) 313 .

B.V. I. MAASILTA, K. KINNUNEN, A. NUOTTAJÄRVI, J. LEPPÄNIEMI AND A. LUUKANEN, *Operation of TES sensors with excess thermal noise*. Supercond. Sci. and Technol. **19** (2006) S242.

B.VI. W. FULLAGAR, J. UHLIG, N. GADOR, K. KINNUNEN, I. MAASILTA, C.-G. WAHLSTRÖM AND V. SUNDSTRÖM , *Lab-based ultrafast molecular structure*. AIP Conf. Proc. **1234** 919 (2010).

B.VII. Z. GENG, K. M. KINNUNEN AND I. J. MAASILTA, *Development of an Inductive NIS Thermometer* . J. Phys. Conf. Ser., in press.

Contents

Chapter 1

Introduction

A transition-edge sensor (TES) is typically a thin superconducting film that can be used as an extremely sensitive thermometer, when it is kept within the narrow region between normal and superconducting states. TES is a very versatile device that can be used to detect radiation in a wide energy range from gamma-rays to sub-millimeter [1]. Measurement of the kinetic energy of massive particles is also possible [2, 3]. In principle, the basic thermometer design can stay the same for different energy ranges, one simply needs to couple it to an absorber that is suitable for the intended application. A TES is a thermal detector, because the absorbed energy causes the temperature of the TES to rise, which is observed as a change in the resistance. When a thermal detector is used to measure the energy of individual photons, it is called a calorimeter. If the flux of incident photons is too large to separate individual photons, the detector is used to measure changes in the flux and is called a bolometer. In this work we will limit ourselves to the study of TES microcalorimeters.

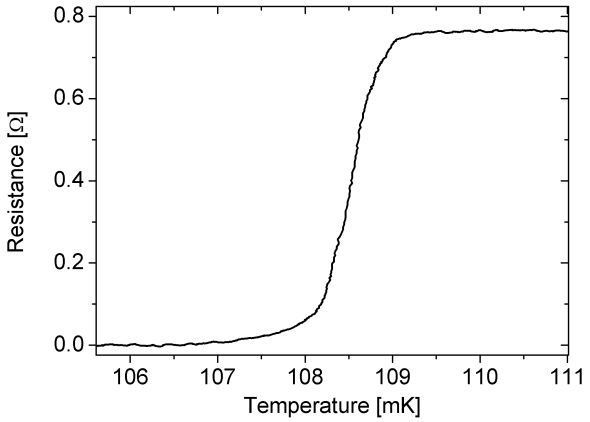

FIGURE 1.1 The transition from normal to superconducting state. A TES is operated in the transition region, where resistance is very sensitive to small changes in temperature.

The first experiments using transition-edge sensors were made already in the 1940's [4, 5]. Technical difficulties in their use kept the TES from gaining popularity until two important advances during the recent years were made. The development of superconducting quantum interference device (SQUID) current amplifiers [6, 7] provided an extremely sensitive, low noise readout that was also suitable for multiplexing. Another important step was the introduction of a voltage biasing scheme [8, 9] that leads to stable self-regulating operation. With the combination of these two techniques, the TES field has seen a tremendously rapid growth with new applications being constantly brought up. TES based detectors have become the leading solution in many research areas, and commercial products employing TES technology have already been introduced. The advances in cooler technologies in the past few years now allow for setups where no cryogenic liquids are needed, making TES technology more appealing for commercial products.

Although the performance of these detectors is already excellent, the theoretical limits in energy resolution have not been reached yet. This is mostly due to excess noise that has been shown to be present in practically all device designs so far. Several candidates for the noise sources have been proposed but a definitive answer is still missing. Before resorting to more exotic sources to explain the observed noise, one should be sure that the known noise mechanisms are fully understood. It is therefore of utmost importance to characterize the detector accurately, both electrically and thermally, to gain understanding on the origin of noise and to determine if truly unknown excess noise is present. The search for the correct explanation of the excess noise is important, because if we were to understand the origin of the noise, we could perhaps be able to come up with new TES designs where the noise either disappears or is minimized. With such improved design, one could then hope to reach energy resolutions that are closer to the fundamental quantum limit than what has been achieved so far.

The main focus of this thesis has been the quest of understanding the "excess" noise in terms of advanced thermal models. As we will show, one part of the noise present in our detectors can be explained by fluctuations in energy exchanged between the TES and the underlying support structure. Another noise term was found to be due to a separation into normal and superconducting phases inside the TES film so that the two phases can be seen as separate bodies in a thermal model, and thus thermal fluctuation noise occurs between them.

1.1 TES applications

During the recent TES boom, the main driving force behind detector and readout development have been the needs of astrophysics and cosmology. There are several ground based and space borne missions either in operation or being prepared. The number of projects is too large to list all of them. In terms of pixels, the biggest one in operation to date is Scuba2 [10] with total TES count exceeding 10000. Micro-X [11] is interesting because it will be the first TES microcalorimeter array in space. Our group at University of Jyväskylä has been involved in the ambitious European Space Agency (ESA) funded technology research program for X-ray Evolving Universe Spectrometer mission (XEUS) [12] that was lead by SRON Netherlands Institute for Space Research. Part of the work reported in this thesis was done under the XEUS project. Note that XEUS was later combined with other missions and it is currently called IXO/ATHENA.

In addition to the above mentioned applications, a growing number of other ground based applications are emerging. These include energy dispersive X-ray microanalysis (EDX) [13], quantum information [14], concealed weapons detection [15], and nuclear proliferation [3].

An interesting new application for TES detectors is time-resolved X-ray absorption fine structure spectroscopy (XAFS) [16] where the chemical processes inside a molecule can be probed with fs accuracy. The author had the privilege to be involved in building and setting up a measurement system in Lund University, Sweden. The experiment is described in article B.VI and will be the subject of an upcoming Ph. D. thesis [17].

In Jyväskylä, we are currently setting up a measurement system for another new application; particle induced X-ray emission (PIXE) [18]. It is similar to materials analysis done in EDX, but in PIXE we will use protons instead of an electron beam to generate X-rays from a target. The advantage of PIXE is a greatly reduced X-ray background. For the last two listed applications, identical state-of-the-art detector setups have been built. They utilize time-domain multiplexing SQUID readout developed by NIST [19] placed in an adiabatic demagnetization refrigerator (ADR). That setup has not been used in the work presented in this thesis.

Chapter 2

Basic calorimeter theory

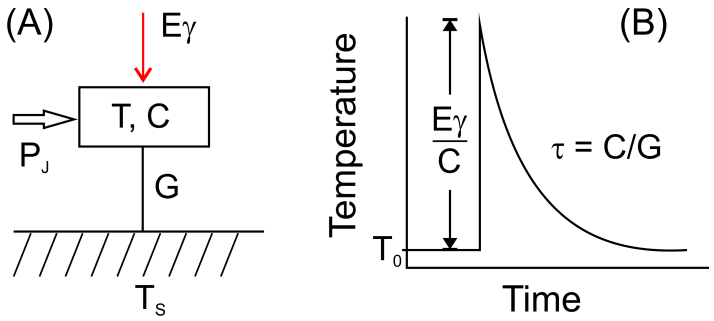

FIGURE 2.1 (A) Simple calorimeter model. (B) Temperature pulse caused by the absorption of a photon.

The basic calorimeter theory is well established by several authors [1, 20–25], here we shall present the important parameters and equations without going into details. A simple calorimeter model is shown in Figure 2.1. A TES with heat capacity C is connected to the heat bath at temperature T_S through a weak thermal link with thermal conductance G. The Joule heating power P_J of the bias current keeps the TES at an elevated steady state temperature $T_0 > T_S$. When a photon with energy E_γ is absorbed, the temperature of the TES rises by E_γ/C and then relaxes back to T_0 in time given by the natural time constant $\tau = C/G$.

The voltage bias circuit is presented in Fig. 2.2, together with a Thevenin-equivalent representation. The thermal and electrical circuits give us two coupled differential equations that describe the response of a TES. Ignoring noise terms, the thermal equation is

$$C\frac{dT}{dt} = -P_{out} + P_J + P_{in}, \tag{2.1}$$

where P_{out} is the power flowing out of the TES, via the heat link into the heat bath,

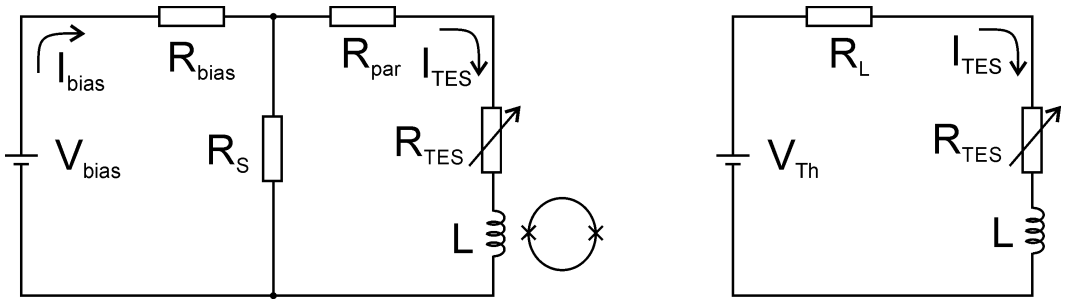

FIGURE 2.2 Left: the circuit used to voltage bias a TES. R_{par} is unwanted parasitic resistance that can exist in the circuit. $R_S < R_{TES} << R_{bias}$. Right: Thevenin-equivalent circuit. $R_L = R_S + R_{par}$ and $V_{th} = V_{bias}R_S/R_{bias}$

and P_{in} is the signal power. A power-law dependence is assumed for P_{out}:

$$P_{out} = K(T^n - T_S^n) \tag{2.2}$$

and the thermal conductance is defined as

$$G \equiv \frac{dP_{out}}{dT} = nKT^{n-1}. \tag{2.3}$$

The electrical differential equation is, also ignoring noise terms:

$$L\frac{dI}{dt} = V_{th} - I_{TES}R_L - I_{TES}R(T, I) \tag{2.4}$$

Because the resistance of a TES is actually a function of both temperature and current, $R(T, I)$, we define two dimensionless parameters that describe the steepness of the superconducting transition: temperature sensitivity

$$\alpha \equiv \left.\frac{\partial \log R}{\partial \log T}\right|_{I_0} = \left.\frac{T_0}{R_0}\frac{\partial R}{\partial T}\right|_{I_0} \tag{2.5}$$

and the current sensitivity

$$\beta \equiv \left.\frac{\partial \log R}{\partial \log I}\right|_{T_0} = \left.\frac{I_0}{R_0}\frac{\partial R}{\partial I}\right|_{T_0}. \tag{2.6}$$

However, the parameter that can be calculated from a measured I-V curve is given by

$$\alpha_{tot} = \frac{T}{R}\frac{dR}{dT}, \tag{2.7}$$

and includes the effects of both α and β. Note that the notation for these parameters varies between authors and care must be taken to avoid using a wrong parameter.

A constant current low-frequency loop gain is defined as

$$\mathcal{L}_I \equiv \frac{P_J \alpha}{G T_0}. \tag{2.8}$$

One can solve the differential equations to find the current response of a TES. We shall not do that here and we simply state that the power to current responsivity,

$$s_I(\omega) = dI/dP_{in} \tag{2.9}$$

is an important parameter that enters directly into many equations that we shall present later in chapter 5 when discussing advanced thermal models. $s_I(\omega)$ gives the theoretical spectral response of the detector to any (photons, thermal noise, ...) input power $P_{in}(\omega)$ and it depends on the used thermal model.

Next we look into the relationship between the three steepness parameters, α_{tot}, α and β. We begin by assuming that we are in the small signal limit, where the TES resistance can be expanded to first order as

$$R(T, I) \cong R_0 + \frac{\partial R}{\partial T}\delta T + \frac{\partial R}{\partial I}\delta I. \tag{2.10}$$

Using Equations (2.5) and (2.6), we get

$$dR = \alpha \frac{R_0}{T_0} dT + \beta \frac{R_0}{I_0} dI \tag{2.11}$$

Similarly, Joule power $P = I_0^2 R_0$ can also be expanded:

$$P(R, I) = P_0 + \frac{\partial P}{\partial R}\delta R + \frac{\partial P}{\partial I}\delta I = P_0 + I_0^2 \delta R + 2 I_0 R_0 \delta I \tag{2.12}$$

$$\Rightarrow dP = I_0^2 dR + 2 I_0 R_0 dI = \alpha \frac{P_0}{T_0} dT + I_0 R_0 (2 + \beta) dI \tag{2.13}$$

From which we get for dI

$$dI = \frac{dP - \alpha \frac{P_0}{T_0} dT_0}{I_0 R_0 (2 + \beta)} \tag{2.14}$$

If we introduce the thermal conductances

$$g_0 = n K T_0^{n-1} \tag{2.15}$$

$$g_S = n K T_S^{n-1} \tag{2.16}$$

we can also write the steady state Joule power as

$$P_0 = K(T_0^n - T_S^n) = \frac{g_0 T_0}{n} - \frac{g_s T_S}{n} = \frac{g_0 T_0}{n}(1 - \frac{g_s T_S}{g_0 T_0}) = \frac{g_0 T_0}{n}(1 - \frac{T_S^n}{T_0^n}) \tag{2.17}$$

We define a new variable ϕ

$$\phi = 1 - \left(\frac{T_s}{T_0}\right)^n \tag{2.18}$$

And from (2.17) we get a useful relation that will be needed later:

$$\frac{g_0 T_0}{P_0} = \frac{n}{\phi} \tag{2.19}$$

Joule power can also be expanded as

$$P_J \approx P_0 + \frac{\partial P_J}{\partial T_0}\delta T_0 + \frac{\partial P_J}{\partial T_S}\delta T_S \tag{2.20}$$

$$\Rightarrow dP_J = nKT_0^{n-1}dT_0 - nKT_S^{n-1}dT_S = g_0 dT_0 - g_S dT_S \tag{2.21}$$

Combining (2.14) and (2.21) we get

$$dI = \frac{(g_0 - \frac{\alpha P_0}{T_0})dT_0 - g_S dT_S}{I_0 R_0 (2+\beta)}. \tag{2.22}$$

Inserting this into Eq. (2.11) and requiring that bath temperature T_S is constant we arrive at

$$dR = (2\alpha + \beta\frac{g_0 T_0}{P_0})\frac{R_0 dT_0}{T_0(2+\beta)}. \tag{2.23}$$

Rearranging Eq. (2.23) we find the connection between α_{tot}, α and β:

$$\alpha_{tot} = \frac{T_0}{R_0}\frac{dR}{dT} = \frac{2\alpha + \frac{n}{\phi}\beta}{2+\beta}. \tag{2.24}$$

2.1 Impedance

The frequency dependent complex impedance of the thevenin equivalent circuit in Fig. 2.2 is

$$Z_{circ}(\omega) = Z_{TES}(\omega) + R_L + i\omega L. \tag{2.25}$$

In the case of the simple thermal model shown in Fig. 2.1, the TES impedance is [1]

$$Z_{TES}(\omega) = R_0(1+\beta) + \frac{R_0 \mathcal{L}_I}{1-\mathcal{L}_I}\frac{2+\beta}{1+i\omega\tau_I}, \tag{2.26}$$

where $\tau_I = \tau/(1 - \mathcal{L}_I)$.

The TES impedance traces a semicircle in the complex plane. In actual detectors, the thermal circuit is often more complicated, which can be modeled by including additional bodies in the circuit. We will return to the advanced thermal models in chapter 5. Here we simply state that when a block is added to the thermal model, it will create a bulge in the impedance curve that extends outwards from that of the simple model, as shown in Fig. 2.3. The shape and size of the new features is determined by the heat capacity of the blocks and the thermal links between them.

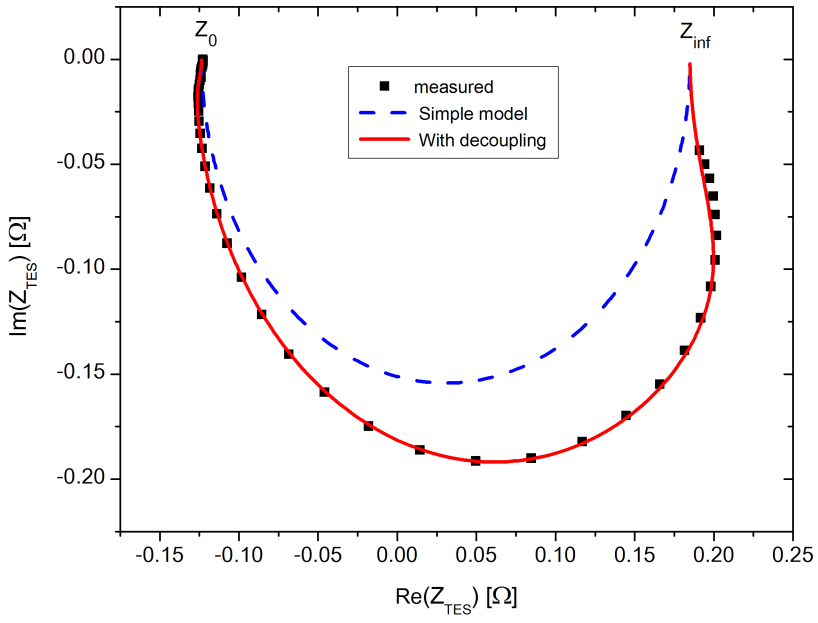

FIGURE 2.3 The impedance of a simple TES model is a semicircle (dashed line) in the complex plane. In real devices the thermal circuit is often more complicated, leading to additional features in the impedance (solid line).

From the impedance we can identify two important parameters: the zero frequency value Z_0 and the high frequency limit Z_∞, which are given by

$$Z_\infty = R_0(1 + \beta) \tag{2.27}$$

$$Z_0 = -R_0 \frac{1 + \beta + \mathcal{L}_I}{\mathcal{L}_I - 1}. \tag{2.28}$$

Regardless of thermal model, in all cases the impedance will approach these limits.

After some algebra we can further write

$$\beta = \frac{Z_\infty}{R_0} - 1 \tag{2.29}$$

$$\mathcal{L}_I = \frac{Z_0 - Z_\infty}{Z_0 + R_0} \tag{2.30}$$

$$\alpha = \frac{n}{\phi}\mathcal{L}_I = \frac{n}{\phi}\frac{Z_0 - Z_\infty}{Z_0 + R_0}. \tag{2.31}$$

To find how α_{tot} can be calculated directly from measured impedance data, we plug the above equations of α and β into Eq. (2.24) to obtain

$$\alpha_{tot,Z} = \frac{n}{\phi}\frac{Z_0 - R_0}{Z_0 + R_0}. \tag{2.32}$$

This should produce exactly the same value as using I-V data and Eq. (2.7). Notice that according to Eq. (2.32), α_{tot} does not depend on Z_∞.

2.2 Negative electrothermal feedback

The voltage bias setup has several advantages [1] that are useful in TES operation. For example, it makes the detector bias point more stable and speeds up the recovery from pulses. To simply describe how the negative electrothermal feedback (ETF) works, consider a TES that is biased in the transition. The system has reached a steady state where the input power from Joule heating of the bias current equals the power flowing out through the thermal link G. When a photon is absorbed, the TES heats up and the resistance starts to increase. Because the TES is voltage biased, the increasing resistance means that the current has to decrease in order to keep voltage constant. Thus, the Joule power $P_J = I^2R$ is decreased, which partly compensates for the temperature increase due to the photon, speeding the recovery back to steady state. The effective time constant due to ETF is given [26] by equation

$$\tau_{eff} = \frac{\tau}{1 + \alpha\phi/n}, \tag{2.33}$$

which shows that the TES will become faster with larger α.

2.3 Noise

There are four main sources of unavoidable noise present in a TES. These are the Johnson noise of the TES, Johnson noise of the load resistors, amplifier noise and

thermal fluctuation noise between the TES and the heat bath, often called phonon noise. The four noise sources have traditionally been taken as the conventional noise and any additional noise is labeled excess.

The power spectral density of the current noise due to Johnson noise is [1]

$$S_{I_{TES}}(\omega) = 4k_B T_0 I_0^2 R_0 \xi(I)(1+\omega^2\tau^2)|s_I(\omega)|^2/\mathcal{L}_I^2, \tag{2.34}$$

where $\xi(I)$ = 1 for normal resistors and for a TES a non-linear quadratic expansion [1,27] gives $\xi(I) = 1+2\beta$. The power spectral density of thermal fluctuation current noise is

$$S_{I_{TFN}}(\omega) = 4k_B T_0^2 G \times F(T_0, T_{bath})|s_I(\omega)|^2, \tag{2.35}$$

where $F(T_0, T_{bath})$ depends on the nature of thermal conductance in the link and typically has values between 0.5 and 1 [20,28].

With the addition of new bodies into the thermal circuit, a new thermal fluctuation noise source is introduced to the system. If an extra heat capacity is brought into contact with the TES so that heat can flow between the bodies, there will inevitably be fluctuations in the energy exchanged through the thermal link between them. The energy fluctuations are seen as noise, just like in the case of phonon noise. The extra body could be an absorber, for example. The thermal conductance could be via the electron or phonon systems, and we shall refer to this noise term as internal thermal fluctuation noise (ITFN) [29]. Thus, when speaking of phonon noise we mean the noise arising from the link between the TES and a heat bath and ITFN refers to any other thermal fluctuation noise that occurs inside the TES. ITFN depends on the thermal model and will be studied in detail later in this thesis.

2.3.1 Excess noise

In addition to the fundamental noise sources, excess noise of unknown origin is seen in many different TES designs. The excess noise often appears to have the same spectral shape as Johnson noise. Several theories to explain the noise have been proposed [29–33] but currently there is no general consensus on a preferred theory. It may of course be possible that different designs exhibit different noise mechanisms and a single universal explanation cannot be found. The excess noise situation is reviewed in more detail in Ref. [1]. An often used method of quantifying the excess noise is by using the M parameter [34], which is the ratio of the excess noise and Johnson noise. Depending on the detector, M has been found to depend in a variety of ways on TES parameters. We note that because the known noise sources are affected by the thermal circuit, one may obtain misleading values of M if the used

thermal model for the TES is not correct.

Article A.I of this thesis presents one theory to explain the excess noise in a special TES geometry. Very briefly said, the excess noise was explained by the fluctuations of the normal-superconducting boundary, or fluctuation superconductivity noise (FSN). The theory was presented in detail in Ref. [35] and in section 6.1 we will discuss the implications of our more recent data on the theory.

2.4 Energy resolution

For calorimeters, the most important figure of merit is the energy resolution. Assuming Gaussian noise sources, it is given by [1]

$$\Delta E_{FWHM} = 2\sqrt{2\ln 2}\left(\int_0^\infty \frac{4}{S_{P_{tot}}(f)}df\right)^{-1/2}. \tag{2.36}$$

$S_{P_{tot}}$ is the total power referred noise that includes all noise sources and is given by

$$S_{P_{tot}}(\omega) = \frac{S_{I_{tot}}(\omega)}{|s_I(\omega)|^2}, \tag{2.37}$$

where $S_{I_{tot}}(\omega)$ is the total current noise.

If the excess noise can be described with the M parameter, a useful approximation is given by [36]

$$\Delta E_{FWHM} = 2\sqrt{2\ln 2}\sqrt{\frac{4k_B T_0^2 C}{\alpha}\sqrt{\frac{nF(T_0, T_{bath})(1+M^2)}{1-(T_{bath}/T_0)^n}}}. \tag{2.38}$$

Chapter 3

Detector design and fabrication

There are several things to consider when designing a calorimetric X-ray detector for a given application. Obviously the intended operating temperature affects the choice of materials to achieve proper critical temperature for the device. The energy range of the radiation to be measured gives constraints on the heat capacity C of the detector. One has more freedom with C if the sensitivity of the TES can be tuned by adding normal metal features, for example. The thermal link G to the heat bath, together with C, determines the speed of the detector. The resistance of the TES may be important for properly coupling it to the SQUID readout. Requirements on absorbtion efficiency affect the thickness of absorbers and filling factor in the case of detector arrays.

3.1 TES materials, controlling critical temperature

The critical temperature T_c is one of the most important parameters for a TES as the operating temperature affects for example the thermal conductance, heat capacity and noise. There are several elemental superconductors that have critical temperatures in the correct range, but for various reasons only a few have been used in TES detectors. The main metals used are Mo ($T_c \approx 0.9$ K), Ti (0.4 K), W (15 mK), Nb (9.2 K), Ir (0.11 K) and Al (1.2 K). We limit our discussion to temperatures below 4 K and thus exclude any devices using high-T_c superconductors. Note that even though W has a very low bulk T_c, it can be tuned over a wide range for thin films [37].

There are some important temperature regions where the detectors are often aimed at, determined by the used refrigeration setup. The simplest solution is to operate at 4.2 K, the liquid Helium temperature. For example, Nb has been used in 4 K bolometer applications [38]. With the emergence of cryogen-free mechanical coolers, this region may become more important in the future for some applications. 300 mK

is the next temperature, achievable by $^3\mathrm{He}$ cryostats. Finally, using either adiabatic demagnetization or dilution refrigerators, 100 mK is a very common target for T_c. The sensitivity of a TES gets better with decreasing temperature, but as long as the resolution is limited by noise in the measured signal, higher bath temperatures are enough.

Devices made of elemental superconductors have been succesfully used in several applications. However, they have disadvantages such as high resistivity or high T_c. To overcome this, a commonly used trick is to take advantage of the proximity effect [39, 40]. When a superconducting metal layer with thickness of the order of the superconducting coherence length of the material is covered by a normal metal, T_c is suppressed. The strength of the effect depends on the ratio of the layer thickness of the normal and superconducting metals so by varying the metal thicknesses, one can tune T_c. In addition to changing T_c, the normal metal layer can reduce the normal state resistance of the device. The most widely used normal metals are Au, Cu and Ag. Another method to control T_c is the implantation of magnetic impurities [41].

Currently the leading solutions in the TES field are Mo/Cu, Mo/Au and Ti/Au. The best reported results [36] so far have been obtained using Mo -based detectors. Unfortunately we do not have a Mo sputtering system in Jyväskylä. This leaves us with Ti/Au as the material of choice if we wish to reach 100 mK T_c using the equipment present in our cleanroom. This is not to say that Ti/Au is a bad choice as it is still widely used. Compared to Mo, the Ti-based detectors tend to have higher resistances and possibly higher excess noise, as shown in this thesis.

In theory, it is possible to predict T_c for a given combination of materials [42, 43]. In practice, the result can depend on many different factors in the fabrication process, and often a more viable solution is to obtain an experimental calibration for each system. As reported in article B.II, we have observed an approximately linear dependence for T_c as a function Au/Ti thickness ratio. In addition to our process, the original calibration also included data from similar SRON detectors at that time. Interestingly, a group in Italy also reported data that agreed with our result [44]. Our old data [B.II] is shown as the solid line in figure 3.1 together with data from more recent pixels.

Although many detectors have a T_c near the old result, there is significant scatter in the results. We believe this is largely due to changes in the cleanness of our UHV evaporation system. The evaporator is used by several research groups for many different materials and it seems to be gradually contaminated over time. Immediately after service where the system is cleaned, the results often follow the "real" calibration for a while. Another important factor is the resist used – it seems

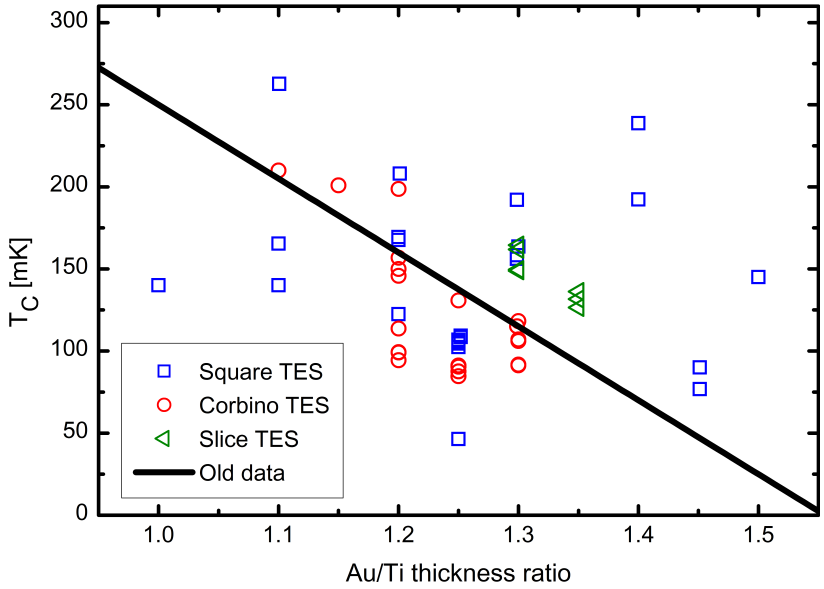

FIGURE 3.1 Obtained critical temperature as a function of Au/Ti thickness ratio. The solid line is the assumed correct calibration for a clean evaporation system. There are several devices where no transition was seen (down to 50 mK) which are not shown in this plot. Old data refers to results reported in article B.II.

that there may be some outgassing during metal deposition that degrades the film quality. We have tested this hypothesis by fabricating identical detectors on two chips with different resist brands in the same evaporation run, and the obtained critical temperatures were different. Other possible source for the variations can be small changes in the details of the fabrication process steps.

Most of our pixels have had Ti thickness around 40 nm and the thickness ratio was tuned by changing Au thickness. This results in relatively large variation in detector resistance, and in hindsight it might have been better to use a fixed Au thickness. Only very recently we have begun to use thicker layers to reduce the resistance of the detectors, in order to meet the L/R time constant requirements of the SQUID readout of our new ADR setup. The slice TES data in figure 3.1 has Ti thicknesses up to 70 nm.

Although we usually talk of bilayers, our TES design actually consists of four layers. The bottom layer is a few nm thick Ti film to improve adhesion to the substrate. Second layer is the thick Au film. The main Ti film is deposited next and it is covered by a 10 nm thick layer of Au that passivates the TES surface and helps in obtaining good electrical contact to the bias lines and the absorber. We have found that if the main Ti layer is deposited before Au, it seems to getter impurities during the time it takes to change the evaporation target in the evaporator. Impurities in the interface between Ti and Au weaken the proximity effect and we had trouble

reaching critical temperatures below 150 mK.

We should also comment on the stability of our Ti/Au films. We have some detectors that were measured many times, during a time span of several years and no shift in T_c was observed. Thus, they seem to have a good shelf life when nothing is done to them. Unfortunately, heating usually leads to a downward shift in T_c. A resist baking step can have an effect, but the biggest problem is the absorber deposition. We have had several detectors ruined by the absorber fabrication process. The degradation does not happen every time, which is somewhat puzzling. One reason for the changing T_c can be diffusion of Au inside the TES or impurities in the Ti/Au interface.

3.2 Controlling the thermal link

The weak thermal link to the heat bath is typically achieved by placing the detector on a thin SiN membrane. Thermal conductance can be controlled by changing the size or thickness of the membrane. Additional tuning can be done by cutting the membrane to restrict heat flow, see for example [45–47].

Our detectors are fabricated on <100> Si wafers with low-stress SiN grown at the UC Berkeley LP-CVD facility. Because we have not had a specific application for our detectors yet, we have not really tried to optimize the thermal conductance to any target value. Because of the limited cooling power of our cryostat (see section 4.1) we generally aim to keep G rather low to avoid large bias currents. We often use 300 nm thick SiN but 750 nm and 1 μm membranes have also been used. A typical size of a membrane is 700 μm$\times$ 700 μm.

3.3 Electron beam lithography

We fabricate our devices using standard electron-beam lithography processing, see references [48,49] for details. Figure 3.2 outlines the basic steps of the e-beam lithography process to produce a basic TES. The figure does not show the first step, which is the processing of the SiN membrane by a standard wet etching of <100> Si in KOH [50]. We also perform an oxygen plasma clean in a reactive ion etch (RIE) chamber after every resist develop step to remove any residual organic materials.

We typically operate on small chip level, with 2-4 separate pixels on a chip. It is slow to pattern large areas by e-beam and secondly, we cannot fit very large chips inside our ultra-high vacuum (UHV) evaporation system. One could name several reasons why optical lithography would be more preferable, but at least our small

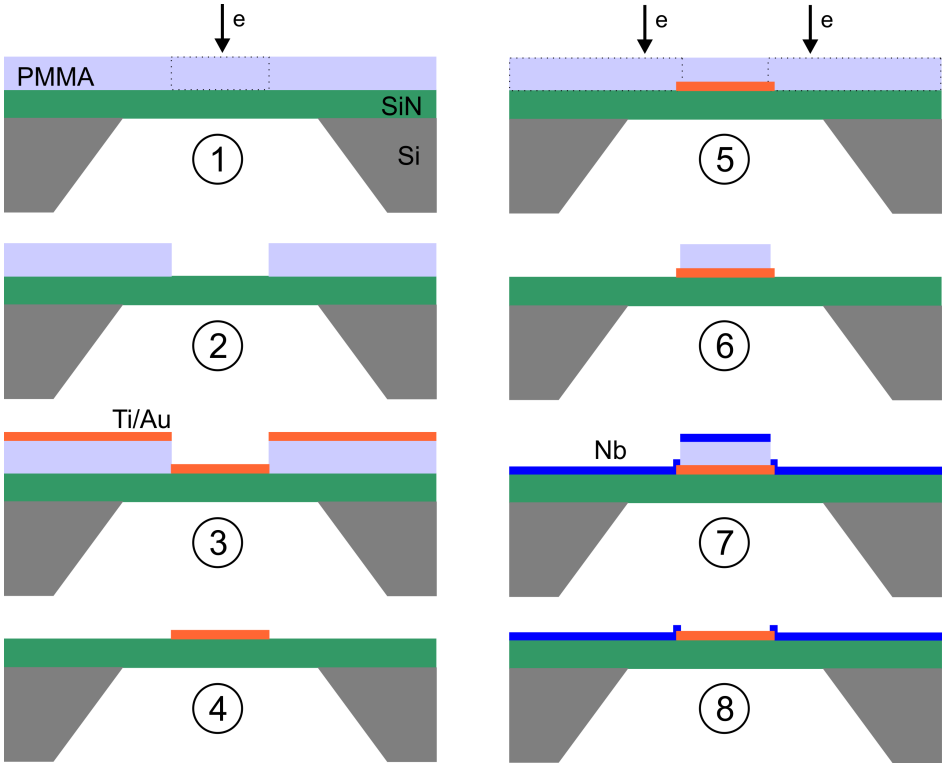

FIGURE 3.2 Overview of the lithography process for a simple square TES. 1) An e-beam resist has been spun onto a chip and is patterned by e-beam. 2) The exposed resist is removed in a developer. 3) TES layers are deposited by e-beam evaporation. 4) Lift-off of the remaining resist. 5) New resist layer is spun and bias lines are patterned. 6) Develop. 7) Bias lines (Nb) are deposited by evaporation. 8) Lift-off. The process can be continued in similar steps to deposit an absorber.

scale production has the benefit of being able to quickly produce new designs. On the downside, the unpredictable T_c control means that when we manage to achieve the desired T_c, there is only a small number of pixels available.

3.4 Basic square TES

A square is the most widely used TES geometry. Apart from the size and materials of the TES film, variation between research groups is seen in the choice of material and geometry of the bias lines. We use Nb in our detectors and the T-shape of the contact prompted us to label our square detectors "TTES". The design is shown in figure 3.3.

The 300 μm size was originally chosen to match the design of SRON because of our collaboration with them. We have not bothered to change the design since and actually in recent years we have not studied the square detectors very intensively.

A new development for us is the addition of normal metal features on top of

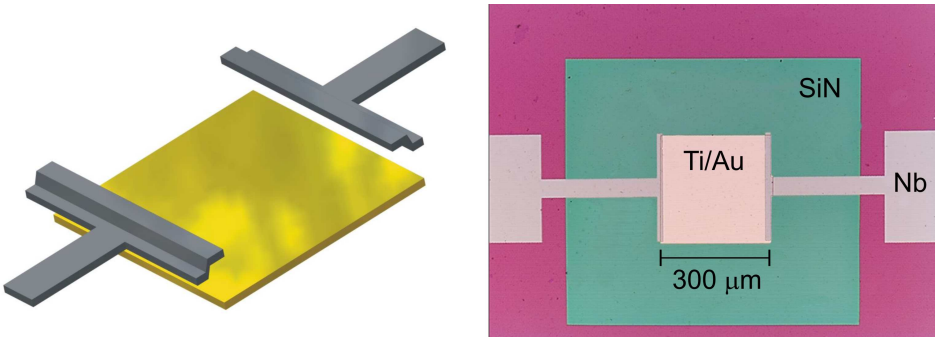

FIGURE 3.3 Our square TES (TTES). Left: a schematic view and right: an optical microscope image of an actual device.

the TES film to tune the TES properties as done by other groups [36, 51, 52]. We have fabricated one such TES, shown in figure 3.4, and checked that it had a good transition but no further characterization has been performed yet.

FIGURE 3.4 A square TES with interdigitized Au bars on top.

3.5 Corbino geometry

The Corbino TES, or CorTES, is a device with cylindrical symmetry where current flows radially outwards from a central contact and is collected at the outer perimeter, as shown in figure 3.5. The original motivation for developing the CorTES was to ensure the absence of edge effects that were reported in square detectors [53]. As reported in article A.I, the CorTES turned out to be a noisy design. Despite the noise, CorTES is an appealing device to study because it is the only TES geometry where we know how the superconducting transition develops. Because the current distribution is radial, the current density is higher in the center which creates a "hot spot" of normal metal. We can determine the phase boundary radius r_b from the measured

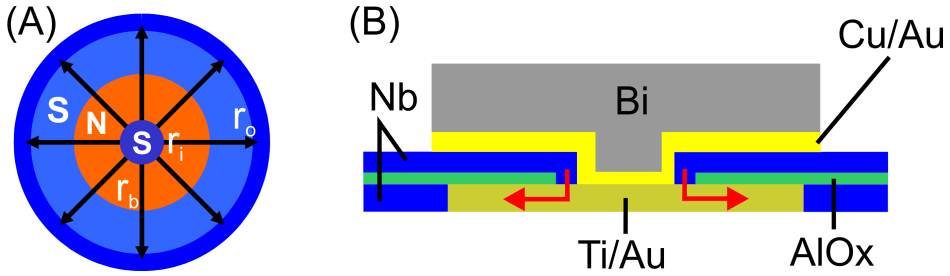

FIGURE 3.5 (A): radial current distribution and phase separation of a CorTES into normal (N) and superconducting (S) regions. The bias contacts are superconducting Nb with r_i and r_0 the radii of the inner and outer contacts and r_b is the radius of the hot spot. (B): schematic side view of a CorTES with an absorber on top. Arrows indicate the direction of current flow.

resistance R in transition, which depends logarithmically on r_b:

$$R \ln\left(\frac{r_o}{r_i}\right) = R_N \ln\left(\frac{r_b}{r_i}\right) \Leftrightarrow r_b = r_i \left(\frac{r_o}{r_i}\right)^{R/R_N}, \tag{3.1}$$

where R_N is the normal state resistance of the device. Once we know the size of the N and S phases, their expected theoretical heat capacities can be calculated as well. This level of theoretical description is not possible with square shaped TES devices.

A CorTES geometry also provides a convenient way to couple the TES to an absorber as shown in figure 3.5B. Notice how the absorber can be put into good electrical contact with the TES film without affecting the T_c of the active area except for possible lateral proximity effects [51, 54]. We assume that heat in the absorber cannot escape via the superconducting bias leads.

Figure 3.6 shows the layer structure of a CorTES. The bottom Nb is usually covered with a few nm thick Au film to passivate the surface. We assume that the extra Au does not affect heat conductance or heat capacity of the TES significantly. The insulation layer prevents the top Nb from short circuiting the TES. The AlOx thickness is typically 100 - 120 nm to ensure there are no pinholes. This thickness is very close to being too much, because we often have step coverage troubles where the top Nb layer cracks. The purpose of the small Ti adhesion layer is to minimize the chance of Nb breaking at the step. The hole in the middle of the top bias contact allows good electrical contact between an absorber and the TES film. With the hole in the top Nb, we have seen that external magnetic field can have a small effect on the transition, whereas with a full Nb top layer there was no field dependence observed [A.I].

To study the noise of the CorTES design, we have fabricated detectors where the TES film is divided into parallel segments, as shown in Fig. 3.7. The idea behind

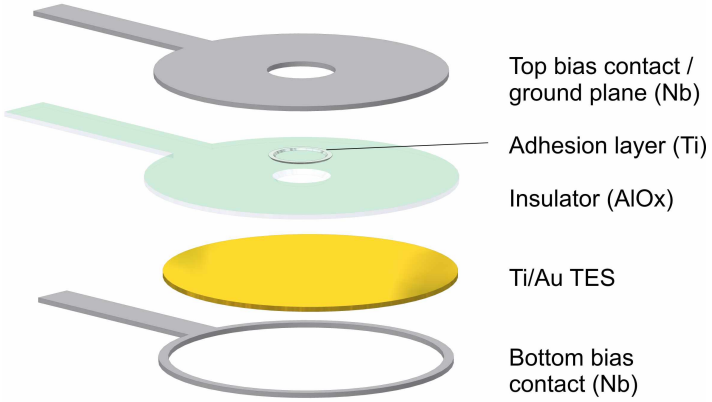

FIGURE 3.6 Schematic view of the CorTES structure. The fabrication process is similar to the square TES, there are just more process steps because of the extra layers.

this design will be discussed in more detail in section 6.1. We have not investigated what effect the slicing has on the internal magnetic field, for example. When the different versions are fabricated in the same evaporation run, both STES and XTES usually have lower values of α_{tot} than OTES.

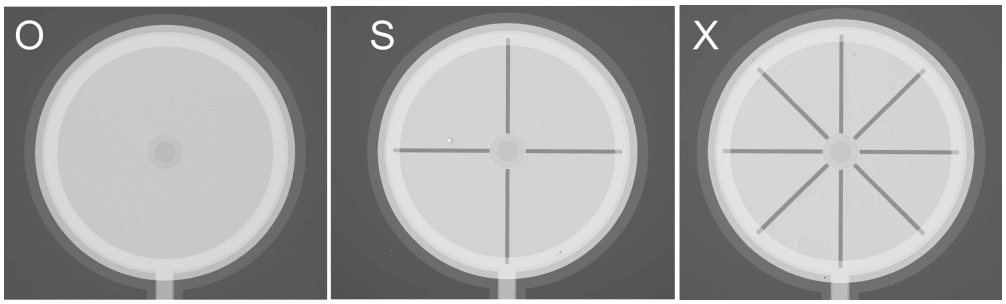

FIGURE 3.7 Scanning electron microscope images of different CorTES devices. The diameter of the detectors is 300 μm. We have labeled the full cortes shown on the left OTES. The middle one is sliced into four quadrants and is called STES. XTES on the right is a CorTES divided into eight parallel slices. Note that the top Nb layer is not sliced.

One benefit of the CorTES design is that it is simple to tune the resistance of the TES. One only needs to increase the radius r_i of the inner contact. We note that if r_i is very large, we approach the region where we may encounter a phenomenon where the TES acts as a weak link [51,54,55]. We have not yet studied this kind of detectors systematically but have begun fabricating them. Further decrease in resistance can be obtained by adding normal metal on top of the TES, and we have achieved R_N = 16 $\mathrm{m}\Omega$, a significant reduction from the standard CorTES whose resistances are usually 200 $\mathrm{m}\Omega$ or more.

3.5.1 Slice TES

An important late addition to our TES designs has been the slice TES or CTES, shown in Fig. 3.8. It is simply just one section of an STES, without the insulator and ground plane. We expect it to retain the property of clearly dividing into normal and superconducting phases like the CorTES. The slice TES results will be discussed in section 6.3.3.

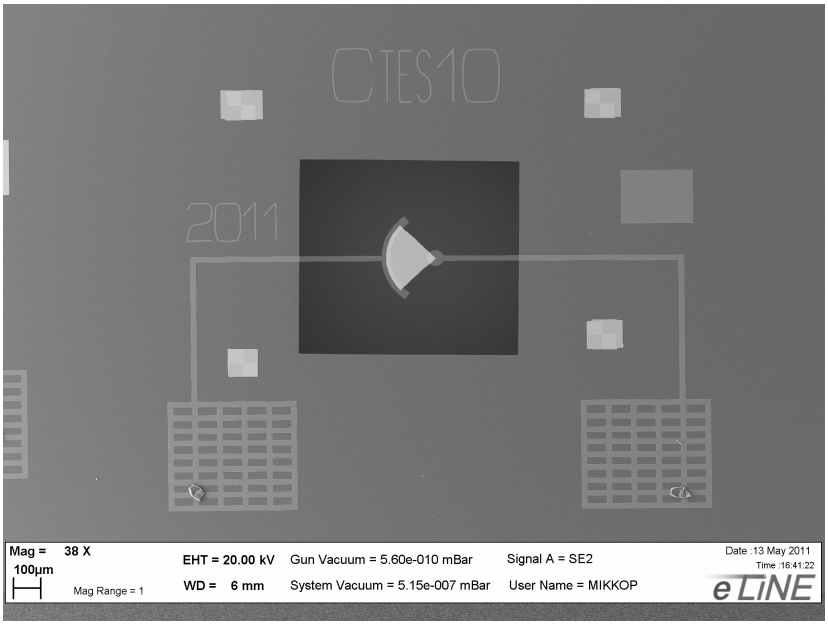

FIGURE 3.8 Scanning electron microscope image of a slice TES, codenamed CTES.

3.6 TES Array

With the setup used in this work we are limited to studying single pixels. After the arrival of our new ADR system we are now able to measure larger detector arrays. Our Raith e-LiNE e-beam writer system allows patterning of large chips with long wiring. The biggest concern is T_c uniformity across a large area. We have fabricated a 32 pixel square TES prototype array to test the feasibility of the process in our cleanroom. The array design and R-T measurement results are shown in Ref. [56]. Out of the 13 pixels measured so far, most were inside a 2 mK T_c window, but there were a few slightly worse pixels.

3.7 Absorber

Although absorber development is not a main topic of this thesis, we shall nevertheless go through some important issues because an absorber is such a crucial part of a microcalorimeter. In the XEUS project considerable effort was put in investigating suitable absorber designs because of the challenging requirements for the planned detector array (90 % efficiency at 6 keV). We have also continued to experiment with ways to improve absorber properties at NSC after our involvement in XEUS ended.

The main criteria for choosing an absorber material are the X-ray stopping power, heat capacity and thermal conductance. Compatibility with the fabrication process is also important. The main materials that have been used so far are Bi, Cu and Au. In the following we present data on these candidates. We only consider single pixels – for arrays the total efficiency is affected by the filling factor. Table 3.1 lists some relevant constants that have been used in the following calculations.

TABLE 3.1 Material specific constants from literature. γ values are taken from [57].

Material	Bi	Cu	Au	Ti
Atomic Weight a	208.98	63.546	196.665	47.88
Mass density ρ_m [$\mathrm{kg/m^3}$]	9800	8920	19200	4500
Coefficient of specific heat γ [$\mathrm{J/K^2m^3}$]	3.926	97.531	65.38	328.86

When designing the absorber geometry it is important to take into account the proximity effect. If the absorber is made of Au or Cu and is put into direct contact with the TES bilayer, it will strengthen the proximity effect and the TES areas under the absorber will most likely stay in normal state. Thus the contact area needs to be restricted by design [46,58]. On the other hand, Bi is a semimetal and has only little, if any, proximitizing effect on a TES. A TES can be completely covered by a Bi layer and the T_c will not be affected strongly.

3.7.1 Efficiency

The absorption efficiency of the absorber tells us the probability with which an incident photon is absorbed. In Fig. 3.9 we present the absorption as a function of photon energy for the relevant materials. We used a 1 $\mu\mathrm{m}$ layer thickness in order to directly compare the materials. SiN is listed to show that it has some stopping power at lower energies, which means that care should be taken to prevent the possibility of events in the membrane or rejecting them in data analysis. Notice that the TES bilayer will also absorb radiation and may result in different pulse shapes

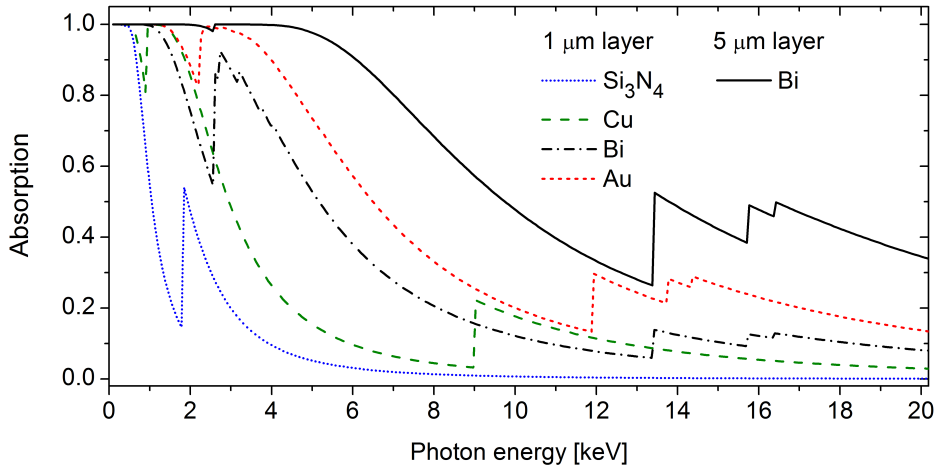

FIGURE 3.9 X-ray absorption for selected materials. Data taken from online database [59].

compared to events in the absorber. Data for the thicker Bi layer is shown because it meets the XEUS requirements for a single pixel. To reach the same efficiency with Au, a 2.7 μm layer would be needed and with Cu it would have to be 22.7 μm thick.

From the absorption curves we can conclude that Au has the best stopping power and Cu is not very good. Also evident is the large decrease in absorption towards higher energies. If an application requires high efficiency above 6 keV, the absorber will need to be very thick, increasing heat capacity. There is also a practical limit to how thick layers can be fabricated using standard lithographic methods, and going much above 5 μm may be difficult.

There exists a number of superconducting materials with good stopping powers such as Nb, Ta, Sn and Pb. The benefit of a superconducting absorber would be low heat capacity but thermalization speed is an issue due to low thermal conductance of a superconductor well below T_c. Sn has been successfully used in detection of γ-radiation [60] but some anomalous behaviour has been reported.

3.7.2 Heat capacity

The specific heat of a crystalline material at low temperatures can be written in the form

$$c = \gamma T + AT^3, \tag{3.2}$$

where γT is the electronic heat capacity and AT^3 is the phonon contribution. For metals at low temperatures, the electronic part dominates and the T^3 term can be ignored. The electronic contribution can be expressed in units [J/KgK] using equation

$$c_{el} = \gamma T/\rho_m \tag{3.3}$$

Assuming a square detector with side length L and thickness t, the heat capacity of a metal can be calculated using equation

$$C = \gamma T L^2 t. \tag{3.4}$$

In the calculations presented here, we use our standard square TES size with $L = 300\ \mu\mathrm{m}$ and assume the absorber to have the same size. In table 3.2 we list some calculated values for the relevant materials. The heat capacity of the TES film is dominated by Ti. Assuming the TES stays at T_c throughout the transition, C will have the normal metal value at the onset of superconductivity and gradually increase to the superconducting value, which is 2.43 times the normal state value as predicted by the BCS theory [61]. Notice that for proximity Ti/Au bilayers, Ref. [62] predicts a jump in heat capacity that is only 73 % of the BCS value.

TABLE 3.2 Calculated heat capacity C for materials of interest at 100 mK and assuming 300 μm$\times$ 300 μm square geometry. The 1 μm values help in comparing the absorber candidates and the larger values correspond to the thickness that provides 0.9 absorption at 6 keV photon energy.

Material	thickness [μm]	C [10^{-13} J/K]
Bi	1	0.35
	4.8	1.69
Cu	1	8.78
	22.7	199
	0.2	1.76
Au	1	5.88
	2.7	15.89
TES Ti	0.04	1.18 - 2.88
TES Au	0.055	0.32 - 0.79

3.7.3 Thermalization

When a photon is absorbed in a (normal) metal, in our typical photon energy range the result is usually the ejection of a photoelectron. This photoelectron quickly loses its energy via electron-electron and electron-phonon interactions, finally producing a heat pulse in the electron system in the vicinity of the absorption event [63]. The electrons quickly spread the heat throughout the metal film until equilibrium is reached. The thermalization time should be as fast as possible, and it is determined mainly by the thermal conductivity of the material which in turn depends

on the electrical resistivity ρ of the metal (see Eq. 3.5). The resistivity data in literature is usually given for bulk materials, but at low temperatures the values for thin films can strongly depend on the film thickness. In addition, the quality of the film may depend on the deposition conditions. It is therefore often necessary to explicitly measure the resistivity of the material for the intended film thickness.

We have found that the grain structure of Bi films depends on the evaporation speed and this also affects resistivity. We have measured values between 700 - 1000 $\mu\Omega\mathrm{cm}$ at 4 K for 2 $\mu\mathrm{m}$ thick Bi deposited at NSC by e-beam evaporation. Resistivity of Cu is strongly affected by the layer thickness. For 200 nm films a value of approximately 1 $\mu\Omega\mathrm{cm}$ was measured and for Au layers near the TES bilayer thickness we have measured about 2.3 $\mu\Omega\mathrm{cm}$.

The thermal conductivity κ_T of a metal at temperature T can be estimated using the Wiedemann-Franz law

$$\kappa_T = \frac{\pi^2 k_b^2 T}{3e^2\rho} \tag{3.5}$$

and thermal diffusivity D [64] can be calculated using equation

$$D = \frac{\kappa_T}{\rho_m c_{el}}. \tag{3.6}$$

The characteristic diffusion time associated with a length scale L is

$$\tau_{diff} = \frac{L^2}{\pi D} \tag{3.7}$$

TABLE 3.3 Parameters for materials of interest at low temperature and assuming 300 $\mu\mathrm{m}\times$ 300 $\mu\mathrm{m}$ square geometry. The ρ values were measured on film thicknesses 2 $\mu\mathrm{m}$, 200 nm and 45 nm for Bi, Cu and Au, respectively.

Material	ρ [$\mu\Omega\mathrm{cm}$]	κ_T [W/Km]	D [m^2/s]	τ_{diff} [μs]
Bi	700	$3.49\cdot10^{-4}$	$8.88\cdot10^{-4}$	32.3
Cu	1	0.244	0.025	1.14
Au	2.3	0.106	0.016	1.77

Table 3.3 gives the calculated parameters based on the measured resistivity values. Of the three materials, Cu has the fastest diffusion time and Bi is roughly 30 times slower. Here we have found the biggest drawback of Bi. We should remember that τ_{diff} is not the time when the absorber has reached equilibrium. Instead, complete thermalization can take several times longer and if fast detectors are required, this can become a problem with Bi. Note that because Bi is a semimetal, the phonon

contribution to thermal conductance may have to be taken into account. The effects of diffusion in absorbers on detector performance was studied in Ref. [65].

If we consider the dimensions of the absorber, we realize that the vertical and lateral diffusion times are very different. If Bi is directly on top of a TES, heat will reach the TES surface well before the absorber itself is thermalized. We suspect this is the reason for the shape of the measured X-ray pulses that we present later in section 6.6.

Taking all the relevant parameters (C, τ_{diff} and efficiency) into account we can conclude that Cu alone would be a bad absorber, but it provides the fastest thermalization layer. This suggests a combination of Bi and Cu where Bi is used for stopping radiation and a thin Cu layer under it is used to speed up thermalization. The 200 nm layer thickness used in calculations above was chosen for this reason. Of course there could be several thin layers of Cu inside a thick Bi film. Engineering the heat capacity is readily achieved by changing Cu thickness. For the design example used here, we would end up with roughly 0.5 pJ/K heat capacity at 100 mK for a single pixel with 0.9 absorption at 6 keV. An all Au absorber has the benefit of being efficient and fast but the heat capacity may become an issue if high absorption is required.

3.8 Improving the properties of a Bi absorber

Even if a Cu or Au thermalization layer is used under Bi, one may wonder if it is enough for thick absorbers. It would be desirable to make sure the whole Bi layer is thermalized fast enough, which requires an improvement in resistivity. We have done experiments where a thick Bi layer was deposited on a thin Au film after which the samples were annealed in a vacuum oven. When the annealing temperature was close to (or slightly over) the melting point of Bi, from SEM images of the Bi surface we observed that the structure had changed noticeably and it seemed that Au had diffused inside the Bi layer. Resistivity measurements were done before and after the annealing step and a clear drop in the overall resistivity was observed as a result of the annealing. The results are reported in more detail in Ref. [56], here we only show one plot from the annealing experiments, where a 2.7 μm thick Bi strip was on top of a 13 nm Au film. The data shown in Fig. 3.10 suggests that if the TES would survive a heating step to about 270 $^{\circ}$C, we could possibly improve the Bi absorber thermalization speed by adding thin Au layers inside the Bi layer and annealing.

Another possibility to affect the properties is to grow Bi by electrodeposition. We have observed considerably larger grain sizes with electrodeposition when compared to e-beam evaporated films, but we do not have more data on such films yet.

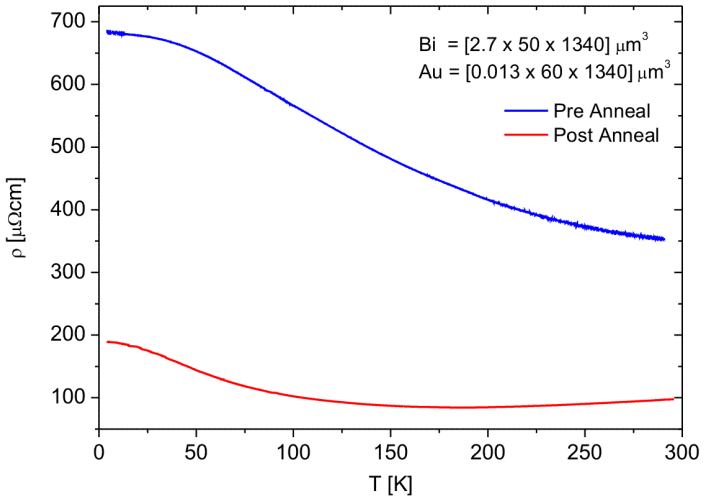

FIGURE 3.10 Resistivity versus temperature of a Bi on Au sample before and after annealing at about 270 °C.

We note that electroplated and evaporated Bi and Bi+Au absorbers are compared and also results on annealing effects are reported in Ref. [66].

Chapter 4

Experimental setup and methods

In this chapter we will present the equipment and go through the various experimental methods that were used during this work. All the measurements were carried out inside an electromagnetically shielded room. A PC for controlling the experiments and recording data sits outside the room and communicates via an optical link with a National Instruments PXI 1002 chassis which is inside the room. The PXI module houses two data acquisition (DAQ) cards and a GPIB interface for communicating with other measurement instruments. One of the DAQ cards (NI PXI-6115) is intended for measuring fast signal (x-ray pulses) at up to 10 MS/s speed but has limited accuracy. The other one (NI PXI-6281) is slower and more accurate and is used to measure everything else. The measurements were done using specialized Labview programs.

4.1 Cryogenics

All of the low temperature experiments that were performed in Jyväskylä were carried out using a small plastic dilution refrigerator (PDR) [67] built in-house, shown in fig. 4.1. The operation of a dilution refrigerator is based on the special properties of a mixture of ^{3}He and ^{4}He isotopes [68, 69]. Our cryostat cools typically to a base temperature slightly below 50 mK. It is designed to fit inside a standard liquid Helium transport dewar. The benefit of using such a compact cryostat is that it is very quick to cool down. It has also proven very reliable and easy to service. On the downside, the cooling power is rather low and the limited space available for wiring and sample stage can become a problem.

The sample stage has evolved through a few iterations and presently we have two different versions in use. The primary stage is made of Cu and is shown in figure 4.1C. The second stage, shown in figure 4.2, is made of Al with a small Cu part for

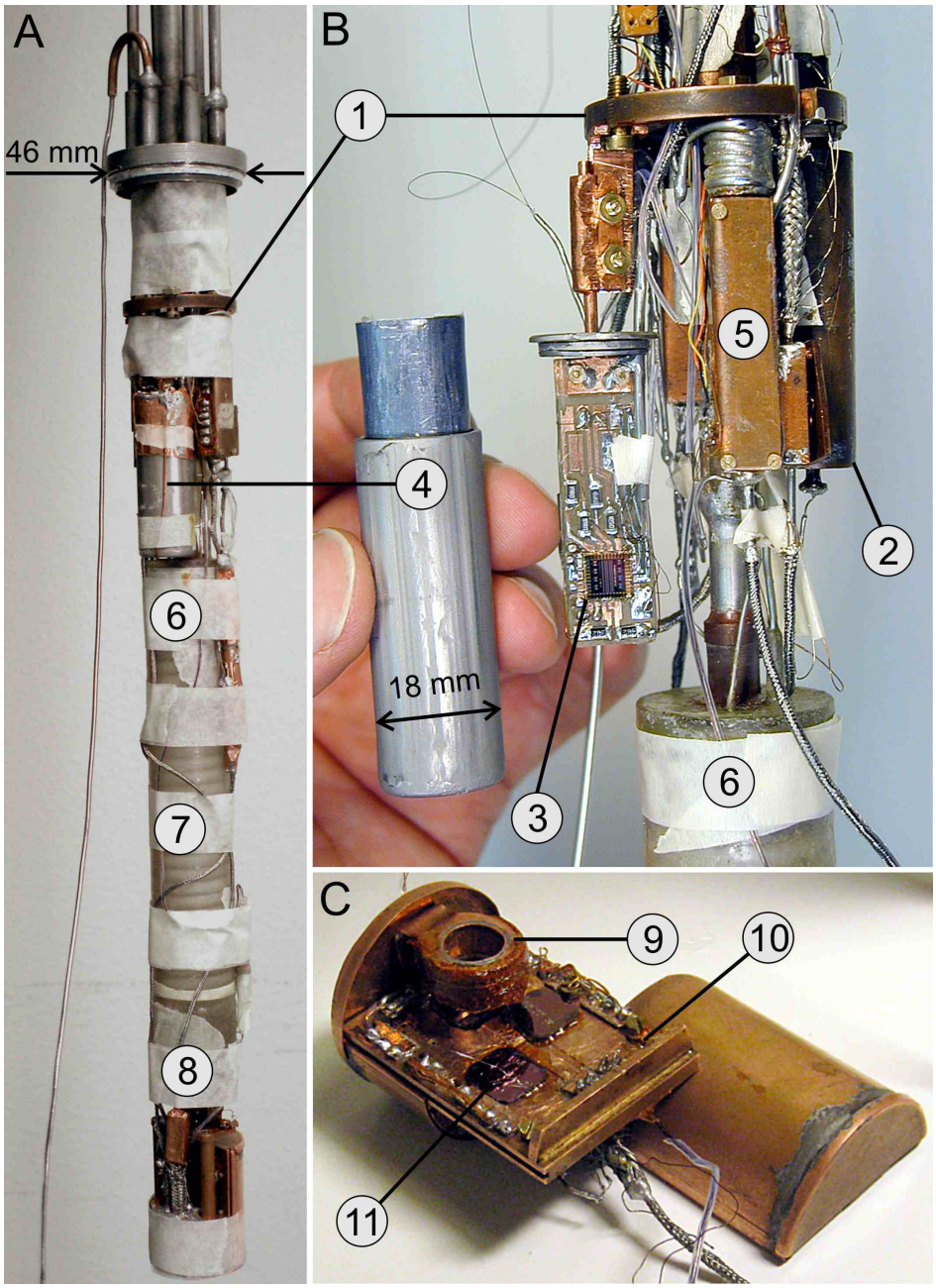

FIGURE 4.1 A) A photograph of the low temperature part of the cryostat. B) Close-up on the 1 K area with the SQUID chip visible. C) Sample stage with the top cover removed. The parts indicated by numbers are: 1) 1.5 K plate, 2) pot, 3) SQUID, 4) Cryoperm + Pb magnetic shield for SQUID, 5) thermalization box for wiring, 6) still, 7) continuous heat exchanger, 8) mixing chamber, 9) superconducting coil, 10) RuO thermometer and 11) detector chip.

thermalizing the detector chip. The Al stage offers better protection against external magnetic fields, but has less space available for samples. A small superconducting coil can be installed inside both setups. We also have a mu-metal (Cryoperm) shield that can be installed over the sample stages to improve magnetic shielding. The cryostat has four separately shielded sets of wiring. There are 12 general purpose lines for four-probe and other measurements. For the SQUID setup, we have separated the feedback lines from bias lines. The fourth set of wires is for the TES bias. A rough schematic of the setup can be found in article B.V.

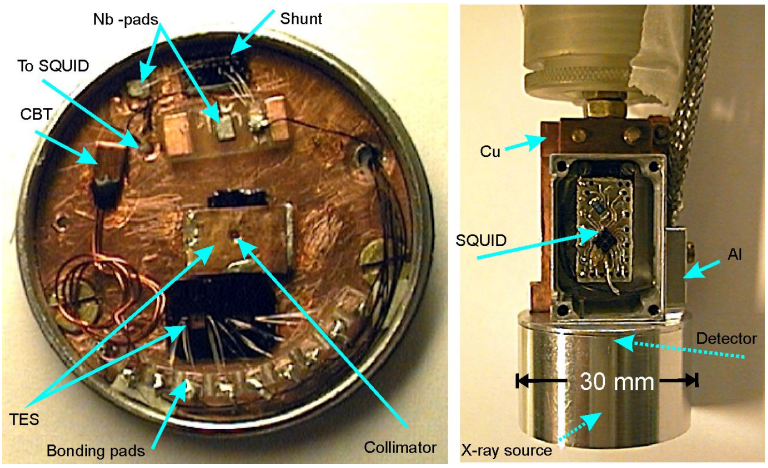

FIGURE 4.2 The Al sample stage with a VTT SQUID.

The temperature of the sample stage is measured using a RuO resistor, which was calibrated against a commercially calibrated Ge thermometer. The resistance of the thermometer is read out by a resistance bridge (Picowatt AVS-47). An additional resistor attached to the sample stage is used as a heater to regulate the temperature. We have a commercial temperature controller (Picowatt TS-530) but it seems to generate large unwanted noise peaks in the SQUID measurements so generally we try to avoid using it if possible. Recently we began using a in-house made Labview PID program using the voltage output of our DAQ card as the heater current source, obtaining more satisfactory performance.

4.2 SQUID readout

When this work began we started with a single stage SQUID from VTT Technical Research Centre Finland. The SQUID [70] was originally designed for magnetoencephalography and modified by VTT to operate at sub-Kelvin temperatures. A special noise cancellation technique [71] was used. The SQUID can be seen in figure 4.2 and more details about the old setup can be found in article B.I. The problem with

the SQUID was its limited dynamic range, and an input coil that was not floating. Partly because of the limitations in the SQUID and also because our setup was still far from optimal in the early stages, the best resolution we reached was 40 eV at 6 keV. This is not a very impressive result and we decided a new SQUID setup was needed.

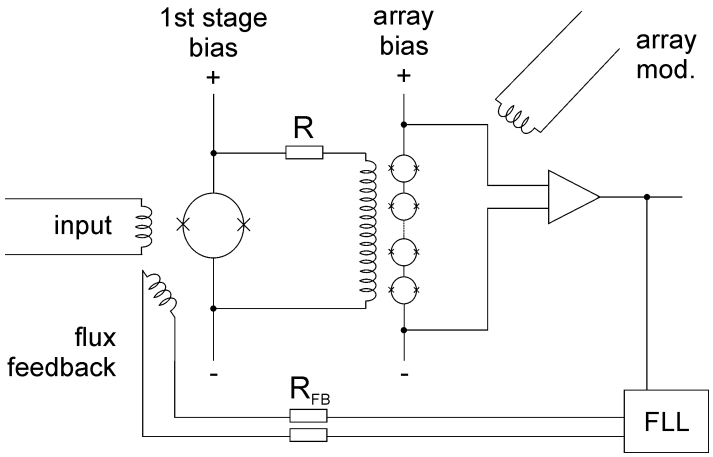

FIGURE 4.3 Schematic of the two-stage SQUID readout. In our setup the array modulation coil is not connected. The FLL box represents the flux lock loop circuit.

We received a two-stage SQUID from NIST with eight multiplexable input channels and a 100 SQUID series array second stage on the same chip [72]. We only use one input channel at a time, so we can measure just one TES in a cooldown. A schematic view of the SQUID is given in figure 4.3. The benefit of using the SQUID array to read out the first stage is, among other things, improved impedance matching to room temperature electronics. The drawback in our case is that 100 SQUIDs dissipate so much power that the SQUID chip cannot be placed in the low temperature stage of our cryostat. Therefore we had to install the SQUID at the 1.5 K stage, as shown in figure 4.1B. This means that the length of the wiring between TES and SQUID input is roughly 30 cm, which makes it more prone to noise pickup and the input inductance is increased. Also, the higher temperature increases the noise originating from the SQUID and related resistors.

Because the output voltage of a SQUID as a function of magnetic field is periodic [6], we need a way to linearize the output in order to use the SQUID as a current amplifier and to increase the dynamic range. This is achieved by the so-called flux lock loop (FLL) technique. As illustrated in Fig. 4.4, the user can choose a bias point in the open-loop modulation curve and tell the FLL unit in the readout electronics to hold the SQUID output voltage at that level. If there is now a change in the current passing through the input coil, the FLL unit sends a current through the feedback

coil that exactly cancels out the change of field from the input coil, thus keeping output voltage constant. Then the measured signal is the voltage fed to the feedback coil, which is directly proportional to the current in the input coil.

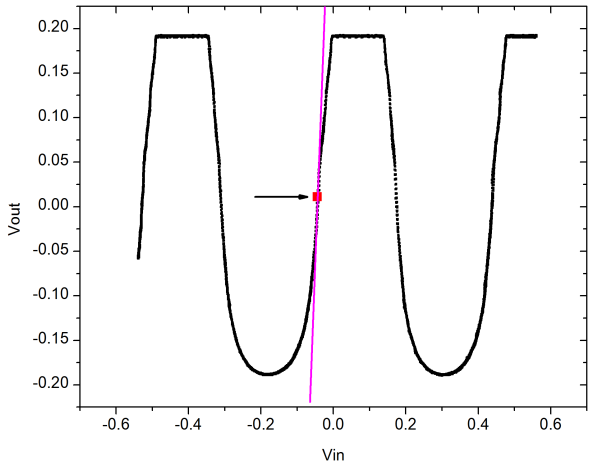

FIGURE 4.4 SQUID array output voltage as a function of field, tuned here by voltage into the first stage feedback coil. The black symbols give the modulation in open loop. The arrow indicates the point where the flux is locked, creating a linearized response shown as the solid line.

Our room temperature SQUID readout and control electronics was designed at SRON. Part of the system (feedback controller) is a modified version of a circuit designed by Hypres Inc. The electronics consists of a preamplifier module that is attached directly to the cryostat, and a remote control system that provides SQUID biasing. The preamplifier has three different amplification modes: direct, I-V and full amp. The direct mode has the lowest amplification and I-V mode has increased gain with freely adjustable output offset level. Full amp has the highest gain and the output is offset near the negative output limit to allow for largest possible voltage swing when X-rays are measured. The circuit also includes a 4 Hz high-pass filter. A photograph of the setup is shown in figure 4.5.

If we consider the TES bias circuit of figure 2.2, it is highly desirable to have all the wiring in the TES branch superconducting to avoid the parasitic resistance R_p. Because our SQUID sits at a temperature where Al bonding wires are still in normal state, we had to manually build a contact between the superconducting input wire (Cu-clad NbTi) and SQUID bonding pads using In, which is superconducting at 1.5 K. Because we need to be able to detach the sample stage from the cryostat, the input wire has to be resoldered for every cooldown. This can cause small variation in R_p as the solder joint probably has some resistance. The bonding pads on the sample stage are made of Cu so there will be an additional resistance that varies depending on how the bonds are placed. Typically we have measured a parasitic resistance on

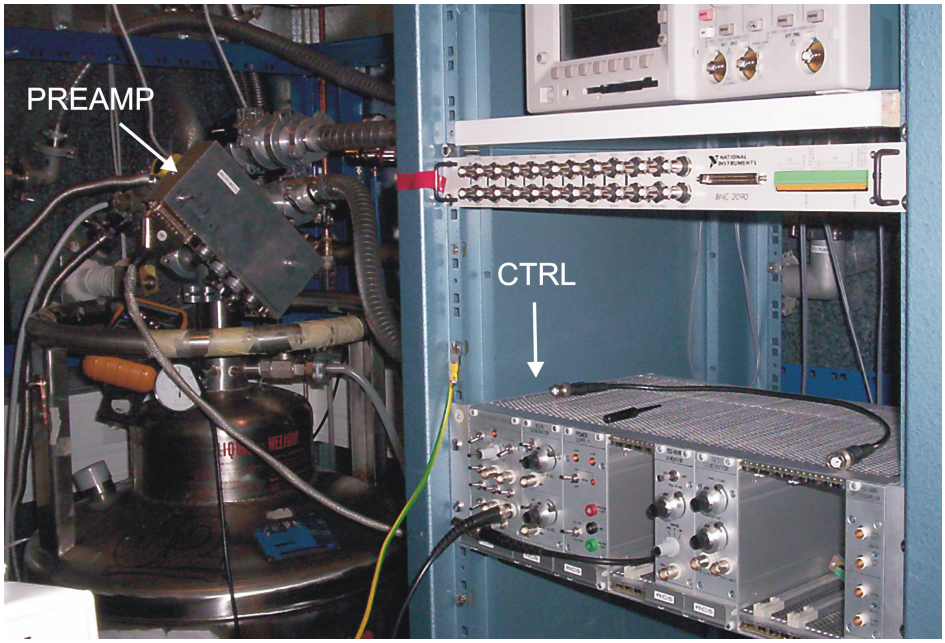

FIGURE 4.5 Picture of the experimental setup. The preamplifier box for SQUID readout is attached to the cryostat and the remote control unit provides bias voltages and signal outputs.

the order of few tens of $\mu\Omega$.

As a final comment about the SQUID we should mention that it had a fabrication error so that the connection between first and second SQUID stages was broken. We were able to fix it by adding an extra Al bond on the chip. This may have some effect on the performance of the SQUID. The magnetic couplings could be affected and the bonding wire adds a small unknown resistance in the circuit. Overall our setup has functioned satisfactorily but as will be discussed in section 4.7.1, there are some concerns in determining a transfer function for the readout which may be related to this issue.

4.3 R-T measurement

The characterization of a new TES begins with the measurement of its R-T curve. We use a standard four-probe lock-in measurement technique to measure the resistance and slowly sweep the cryostat temperature to find the critical temperature. We use a SRS 810 digital lock-in amplifier and Ithaco 1201 voltage amplifier. Typically we use a 17 Hz excitation current of 0.5-1 μA (RMS) to make sure we do not affect the result by excessive Joule heating.

Ideally, one should find the critical temperature at zero magnetic field. In practice it is difficult to cancel out every component of earth and stray fields. In the case

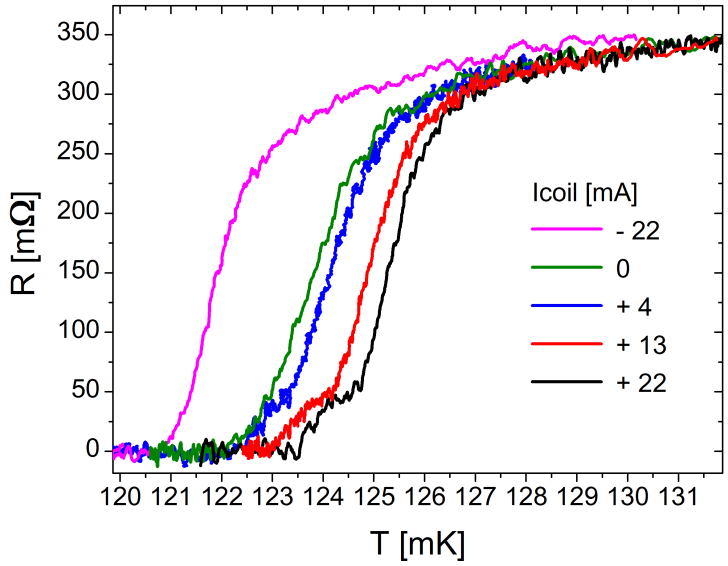

FIGURE 4.6 The effect of external magnetic field on the superconducting transition of a square TES. Earths field is canceled with coil current +22 mA. The data is from SRON pixel 13, discussed in section 6.4.2.

of a CorTES, the Nb layer shields well against external fields, for example from our nulling coil, and we are stuck with whatever field was pinned in when the Nb layer turned superconducting. The effect of magnetic field on the transition of a square TES is shown in figure 4.6.

In addition to T_c, an important parameter we obtain in this measument is the normal state resistance R_N of the TES. At a bath temperature well above T_c we use a larger measurement current and average the signal over several minutes to obtain R_N. Sometimes when TES resistance is low, we also check R_N by the so-called delta pulse method, which is a four-probe measurement using a current source (Keithley 6221) and nanovoltmeter (Keithley 2182A). The source alternates the signal polarity, canceling out possible thermoelectric effects.

We also try to look for temperature dependence of the resistance before T_c by doing a long sweep preferably starting from 4 K but sometimes from 1 K down. If the TES features a significant slope in R_N, it is troublesome for I-V and impedance analysis. Our CorTES devices usually have a fairly flat resistance before the transition. Square pixels with extra normal metal features, at least if made of Cu, are more troublesome in this regard.

4.4 I-V measurement

After the R-T measurement, a TES is connected to the SQUID readout and the voltage bias circuit as was shown in figure 2.2. Because the shunt resistance R_s is much

smaller than the bias resistor R_{bias}, we can approximate the Thevenin equivalent voltage V_{Th} and load resistance R_L as

$$R_L = R_{par} + R_s \tag{4.1}$$

$$V_{Th} = \frac{V_{bias} R_s}{R_{bias}} \tag{4.2}$$

where R_{par} is unwanted parasitic resistance in the circuit and the DC current I_{TES} is given by

$$I_{TES} = \frac{V_{Th}}{R_L + R_{TES}} = \frac{V_{bias} R_s}{R_{bias}(R_L + R_{TES})} \tag{4.3}$$

We only know R_{TES} in two situations: it is R_N in normal state and zero when the TES is superconducting. To calculate the current in the transition, we need to know the gain of the SQUID amplifier. The variables that we can directly measure are the output voltage V_{out} of the SQUID readout and the input bias voltage V_{bias}. Gain in units V/A is given by

$$Gain_{SQUID} = \frac{dV_{out}}{dI_{TES}} = \frac{dV_{out}}{dV_{bias}} \frac{dV_{bias}}{dI_{TES}}. \tag{4.4}$$

From Eq. 4.3 we get:

$$\frac{dV_{bias}}{dI_{TES}} = R_{bias}(R_{TES} + R_L)/R_s. \tag{4.5}$$

We can obtain dV_{out}/dV_{bias} from the measured raw data as the slope of the linear regions that correspond to the two known TES resistances, as demonstrated in figure 4.7(A).

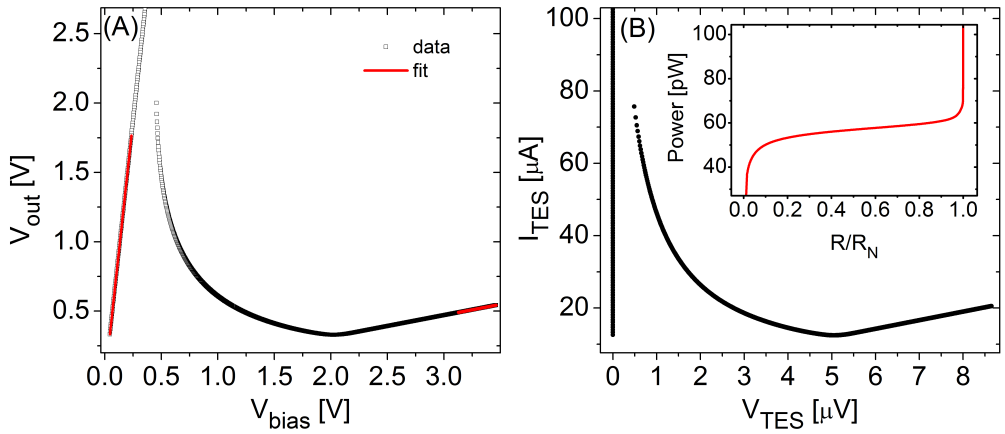

FIGURE 4.7 (A) Raw I-V measurement data. Fits to the linear regions are done to determine the gain of the SQUID readout. (B) I-V curve of a TES. Inset: calculated power dissipation showing the almost constant power in the transition. The data is from the TTES discussed in section 6.3.4.

We should get the same gain from the two different regions. If the values disagree, it indicates an error in one of the resistances (R_{bias}, R_{TES}, R_s, R_{par}). On the other hand, if one is confident that the other parameters are well known, we can quite accurately determine R_N if it was not measured beforehand in a separate R-T measurement. After an arbitrary SQUID output offset is removed from the raw data, we can use the SQUID gain to calculate I_{TES} from V_{out}. The voltage over the TES can then be calculated using

$$V_{TES} = V_{Th} - R_L I_{TES}. \tag{4.6}$$

An example of the resulting TES I-V curve is shown in figure 4.7B. One can calculate many useful parameters from the I-V curve. TES resistance and dissipated power are trivially given by $R_{TES} = V/I$ and $P = VI$. A convenient parameter that we use often in plots to express the bias point is the scaled resistance R_{TES}/R_N. From Eq. 2.2, TES temperature T_0 can be calculated as

$$T_0 = \left(\frac{P}{K} + T_S^n\right)^{(1/n)} \tag{4.7}$$

and the dynamic thermal conductance to heat bath is given by Eq. 2.3.

The R-T curve obtained from I-V is different from the lock-in measurement due to the current dependence of resistance, as shown in figure 4.8(A). Finally, taking a derivative of the calculated R-T and using Eq. 2.7 we find the total α of the TES, shown in figure 4.8B. To distinguish from the total α obtained from impedance measurements, we call this $\alpha_{tot,IV}$.

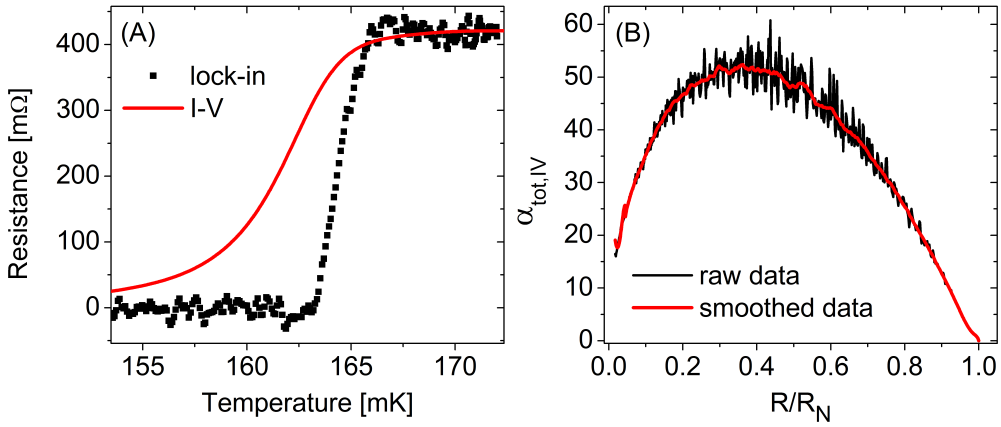

FIGURE 4.8 (A) Comparison of R-T curves measured using different methods. Lock-in measurement is performed using very low current and by sweeping the bath temperature. In contrast, the R-T curve obtained from I-V is measured at low bath temperature and large current, which means that the effect of β shifts the transition. (B) Total α calculated from I-V. The data is from the TTES discussed in section 6.3.4.

While $\alpha_{tot,IV}$ is a useful indicator of how good a TES might be as a detector, the numerical differentiation can result in noisy data. In our plots we usually show data that has been gently smoothed. This may cause some error if a TES has sharp changes in the transition steepness, but luckily such features are not very common. The spiky nature of the $\alpha_{tot,IV}$ curve in our measurements comes from the method used in the I-V measurement. We have a custom made low-noise battery powered voltage source that can be controlled by a computer. The measurement software increases the voltage in small steps and for each step the bias voltage and SQUID output are averaged for a desired time. By doing this we can average out the effect of temperature fluctuations of the cryostat, and because a really good measurement can take as long as 20 minutes, we are guaranteed to be truly in the DC limit.

As a final comment about $\alpha_{tot,IV}$ we should point out that in the older publications (A.II, A.III) of this work we did not use the R-T data for calculating the total α. Instead, we used the equation

$$\alpha_{tot,IV} = \frac{n}{\phi}\left|\frac{\frac{I_0}{V_0} - \frac{dI}{dV}}{\frac{I_0}{V_0} + \frac{dI}{dV}}\right| \tag{4.8}$$

which can be shown to be equal to Eq. 2.7. The reason to mention this is that we used an approximation $T_s \ll T_0$ and ignored the ϕ term. In practice when operating at 50 mK and T_c is 100 mK, ϕ is roughly 0.9 and should not be ignored. Therefore, the plots in article A.III, where this total α is used have values that are possibly too small. In A.II this was compensated by using n = 4 which is likely too large.

4.5 Measurement of the thermal properties of SiN

The thermal conductance of the link between the TES and the heat bath is an important design parameter. The material specific parameters K and n are in an important role in many equations describing TES physics. Unfortunately, it is also quite difficult to measure them accurately. Typically, a series of I-V curves is measured at several different bath temperatures, and the dissipated power P_0 is calculated. Then a fixed point in resistance R_0 (at temperature T_0) is chosen and the power at that bias point is plotted against bath temperature T_S, as shown in figure 4.9. Equation $P = K(T_0^n - T_S^n)$ is then fitted to the data and parameters n, K and T_0 are obtained.

We usually select a bias point very high in the transition to minimize the effect of the β parameter, as we often see that the fit results change if the chosen bias point is brought too low. We shall return to the results and possible problems later in sec-

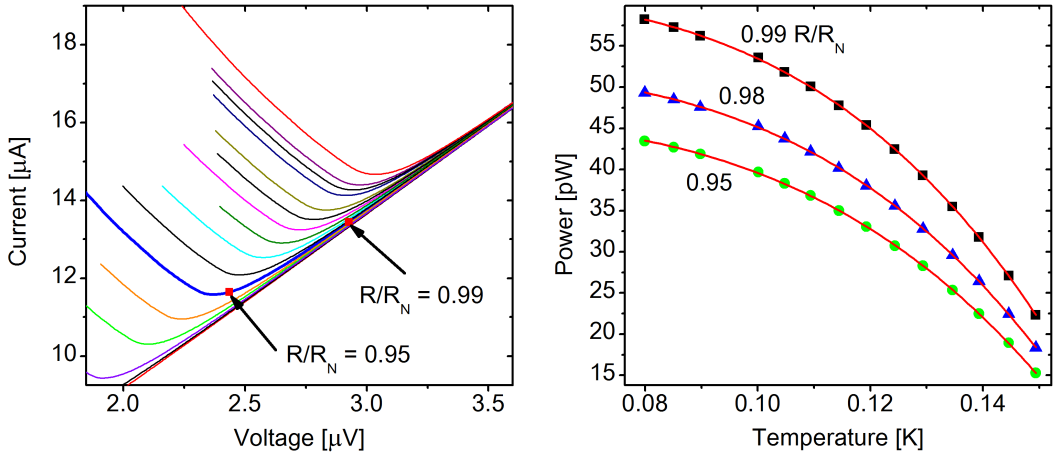

FIGURE 4.9 Example of the method to measure n and K for SiN membranes using a TES. Left: A set of I-V curves measured at various bath temperatures between 150 mK and 80 mK. The lowest bath temperature corresponds to the transition that begins at the highest voltage. A bias point very high in the transition if preferred. Right: a fit to the power equation yields the desired parameters. In this example the obtained parameters were different for each shown bias point: n = 3.92, 3.84, 3.74 for R/R_N = 0.99, 0.98, 0.95, respectively.

tion 6.5. The possible shortcomings of this method are discussed in Ref. [73] where a new, more complicated method for extracting the parameters is also introduced.

4.6 Noise measurement

The noise measurements are done with the SQUID preamplifier in the full amp mode using an Agilent 89410A spectrum analyzer. We usually record data between 4 Hz and 1 MHz and take the measurements in several pieces, changing the frequency span in decade increments. While this method may be somewhat slow, it ensures we have good quality spectra. In figure 4.10 we present an example of a typical noise spectrum where we can see the peaks of 50 Hz mains and multiples and some extra peaks from unknown sources. Those features are usually always there, and if they are not seen in some of the plots presented in this work, it is because we have cut them out to improve the readability of the plots – especially when several spectra are shown in the same graph.

We note that we have not observed any $1/f$ type of noise component in our measurements, either because it does not exist in our devices, or because it would only be seen at very low frequencies and the high-pass filter of the readout hides it. There is, however, a phenomenon that would give us a large error unless we pay attention to the measurement when looking at the spectrum below 1 kHz. We usually see pulses in the SQUID output, as if radiation was being absorbed. This

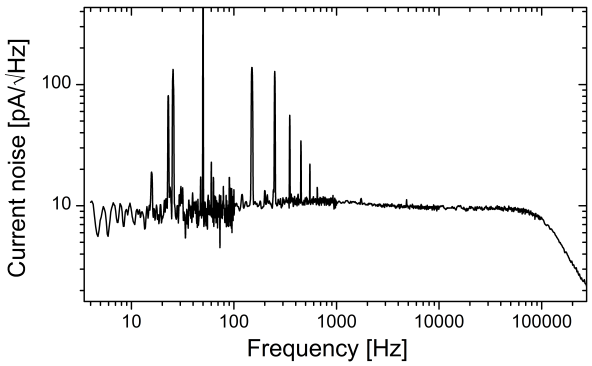

FIGURE 4.10 An example of a typical noise spectrum.

happens when an x-ray source is not present and with detectors without absorbers. The pulses come at seemingly random intervals but the time between them is often too short to obtain a long average of the noise. They are only observed when the TES is biased in the transition, so we think it is not originating from the SQUID or the readout electronics. The pulses could be caused by cosmic rays or some radioactive material inside our cryostat that we are not aware of, or by some processes in the detectors that randomly release energy. The pulses do not affect the noise data shown in this work because the noise measurements are restarted if a pulse is observed and the affected data is discarded.

4.7 Impedance measurement

The frequency dependent complex impedance Z of a TES has quickly become a standard analysis tool in the TES field. It provides insight into the electronic and thermal circuits and allows the extraction of important parameters such as α, β and heat capacity. During this work we have used two slightly different methods for measuring Z. First we started with a method where white noise is fed into the TES bias as described in reference [74], with the exception that we used a spectrum analyzer instead of an oscilloscope. Additionally, our measurement bandwidth is much larger because in our Ti/Au detectors most of the interesting action happens at higher frequencies. Our measurement setup is presented in figure 4.11.

Because in the noise method the amplitude of the input noise needs to be larger than the intrinsic noise sources, there is a reason to be worried about overheating the TES, especially considering the wide frequency range that we have to use. If the TES is heated during the Z measurement, its operating point will be shifted. When that happens, the measured noise and corresponding Z data are effectively not at the same bias, which can cause problems in using a thermal model to fit for noise

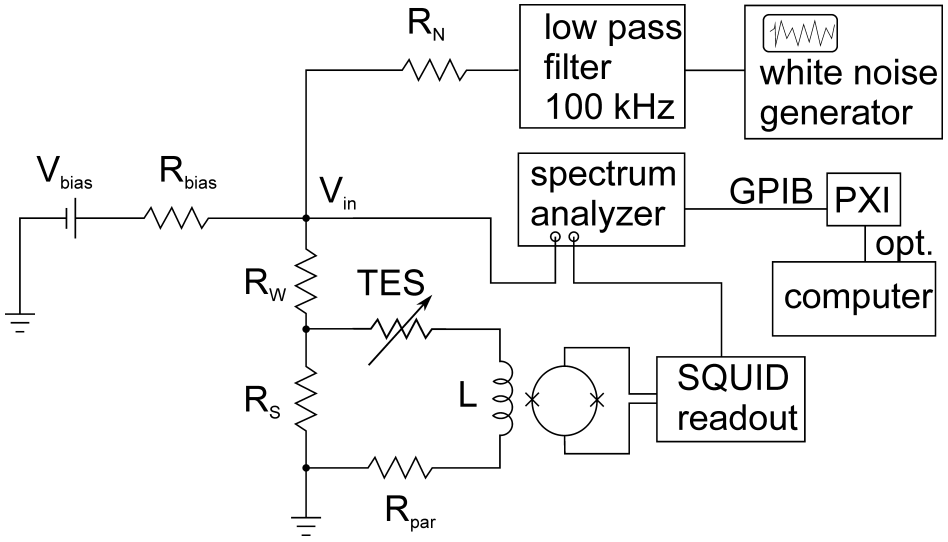

FIGURE 4.11 Setup for measuring circuit impedance using white noise method. The spectrum analyzer measures the real and imaginary parts of both the input and output noise. Simultaneous snapshots of the noise are taken so that input and output are correlated and circuit impedance is calculated from an average of the snapshots. R_W = 201 Ω is the resistance of cryostat wiring. R_S = 8.92 $\mathrm{m}\Omega$, R_{bias} is varied between 2-10 $\mathrm{k}\Omega$ and R_N was usually > 10 $\mathrm{k}\Omega$.

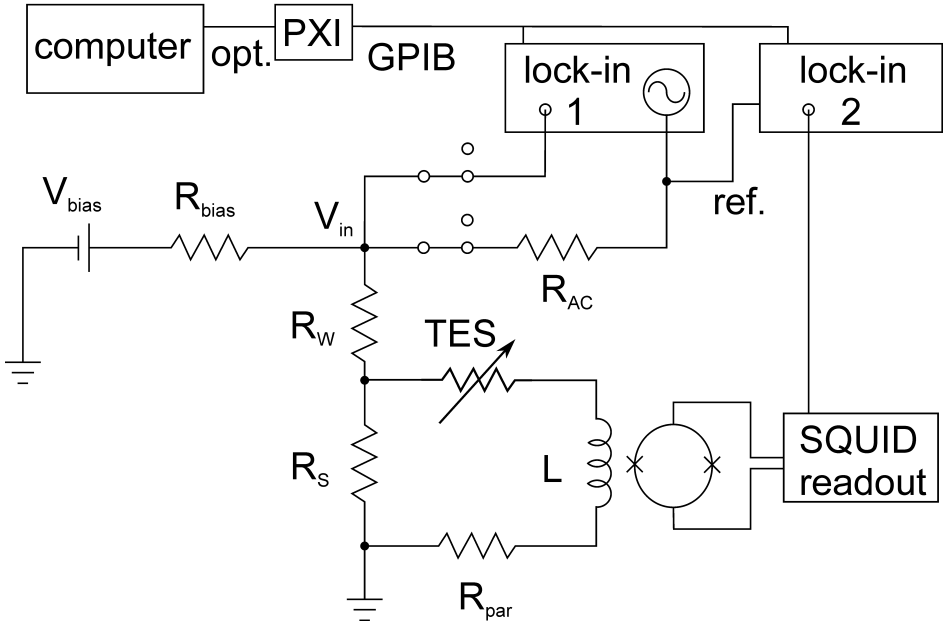

FIGURE 4.12 Setup for measuring Z using lock-in amplifiers. A computer controls the output frequency of an internal signal generator in lock-in 1 and reads out the measured amplitude and phase of the signal from both amplifiers. The frequency is swept in logarithmic steps between 10 Hz and 100 kHz and for each frequency the signals are sampled until a satisfactory level of averaging is obtained. Resistor values were as in Fig. 4.11.

and Z. For this reason, we switched to a technique where a swept frequency sine wave is used instead, and signals are read out with lock-in amplifiers as described in reference [75]. The measurement setup is presented in figure 4.12.

One possible way to check for the heating effect of Z measurement is to compare the total α from Z and I-V data which should give the same values. As shown in figure 4.13, we often see deviation with the noise method while lock-in data is typically more consistent.

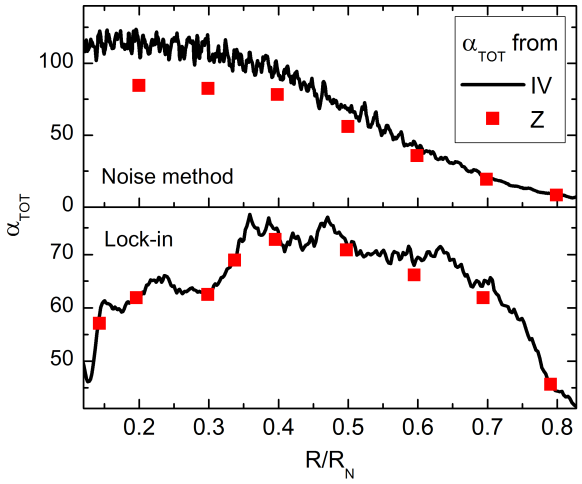

FIGURE 4.13 Total α calculated from Z and I-V data. Noise Z method fails to match I-V. The slight discrepancy in lock-in results may be due to smoothing applied on the I-V data. Top and bottom data are from different detectors.

What we get as a result of the Z measurement in an ideal case is the impedance of the circuit in figure 2.2(b), given by Eq. 2.25. In reality there will be additional effects coming mainly from the SQUID readout and possible extra inductances in the circuit. To obtain the true Z_{TES} we need a way to remove these effects from the measured data. This can be achieved by determining a frequency dependent transfer function $G(\omega)$ for the system.

4.7.1 Transfer function

Taking the transfer function $G(\omega)$ into account, we can write the measured impedance as $Z_{meas} = G(\omega)Z_{circ}$, and if $G(\omega)$ is known, the circuit impedance is given by

$$Z_{circ} = Z_{meas}/G(\omega). \tag{4.9}$$

We can find the transfer function by taking advantage of the two known resistances of the TES. By taking the ratio of the measured impedance in normal and supercon-

ducting states, we cancel $G(\omega)$ and end up with

$$\frac{Z_{meas,N}}{Z_{meas,SC}} = \frac{R_N + R_L + i\omega L}{R_L + i\omega L} \tag{4.10}$$

When the above equation is fitted to the ratio of the measured impedances as shown in figure 4.14, we obtain the values for L and either R_N or R_L, depending on which is "more unknown" – in our case usually R_L. We see that the fits are good, showing that the simple bias circuit model is a good approximation. Armed with the correct circuit parameters we obtain the transfer function using

$$G(\omega) = \frac{Z_{meas,N}}{R_N + R_L + i\omega L} \tag{4.11}$$

or alternatively using superconducting data.

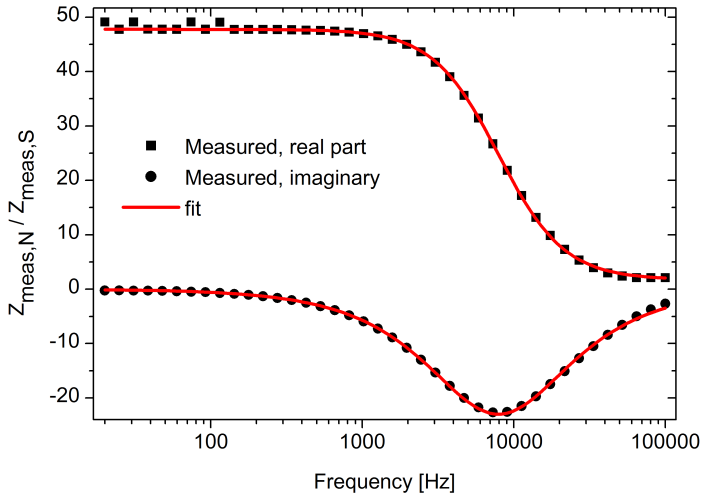

FIGURE 4.14 Fit to the ratio of measured impedance in normal and superconducting state to find L and R_L.

Equation 4.9 is used to calculate Z_{circ} and finally we obtain TES impedance:

$$Z_{TES} = Z_{circ} - R_L - i\omega L. \tag{4.12}$$

The method described here requires that the transfer function is stable. That is, it should be the same with all TES resistances. Another issue to consider is how the measurement is performed, as it can be done with the TES biased and at low bath temperature or unbiased at high temperature (for normal state) [75]. If the TES resistance has observable slope in resistance far above T_c, the unbiased method may be better, but then one has to be sure that the shunt (and parasitic) resistance is not affected by temperature.

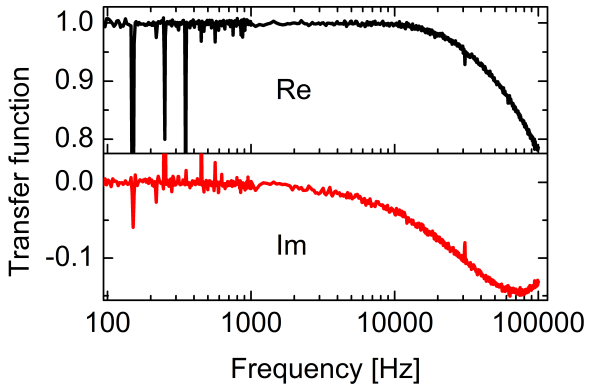

FIGURE 4.15 An example of a typical transfer function for our system.

We have observed that the fitted L varies between measurements, depending on the TES and possibly the shunt resistor. The value of L is typically near 200 nH, whereas the geometric inductance for our SQUID is about 300 nH. This is typical for FLL operation, as discussed below in section 4.7.2. Another observation is that the normal and superconducting data produce a slightly different $G(\omega)$. This is illustrated in figure 4.16. As can be seen, the data calculated using SC transfer function deviates from N data at high frequencies ($f > 50$ kHz).

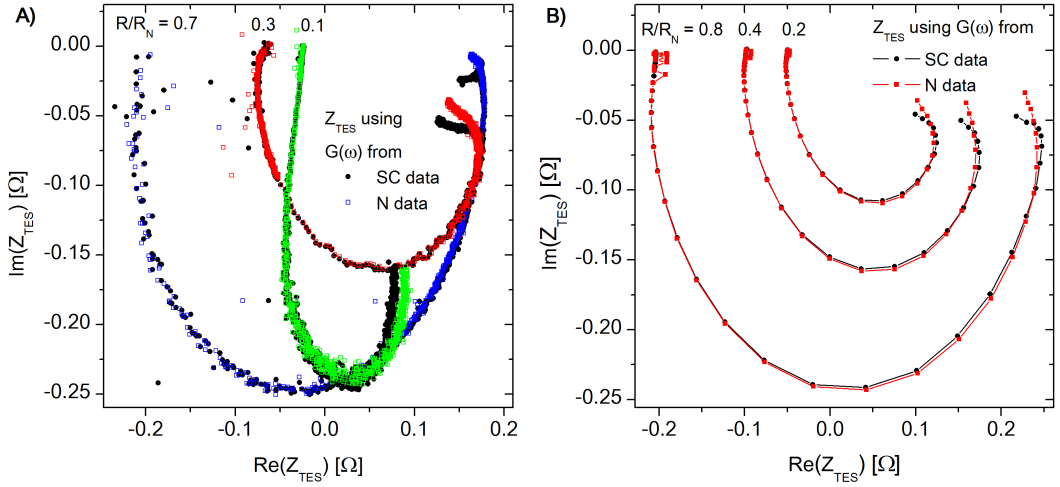

FIGURE 4.16 Comparison of Z_{TES} results obtained using $G(\omega)$ from normal (N) and superconducting (SC) data. (A) Noise method. Black circles are the SC data. The data is from the OTES discussed in section 6.3.1. (B) Swept sine method. The data is from the STES discussed in section 6.3.2.

Whatever the reason is for the difference, we have chosen to trust the normal state data more, and usually use that for the $G(\omega)$ calculation. We justify this choice by the fact that the normal state data is much less sensitive to variations in L. To conclude, there remains some uncertainty that should be kept in mind when the impedance data is used in fits to thermal models.

4.7.2 Effect of the SQUID circuit on impedance and transfer function

Part of the observed trouble with $G(\omega)$ is possibly explained by the fact that the SQUID effective input impedance is more complicated [76,77]. Instead of a purely inductive part, while operating in FLL mode the impedance of the SQUID input is [77]

$$Z_{in} \approx i\omega L_{in}(1 + k^2_{IN,SQ} g_{J\phi} + l_{FB}) + \omega^2 L_{in} \tau_{FLL} l_{FB}, \tag{4.13}$$

where

$$l_{FB} \approx -k^2_{IN,SQ} g_{J\Phi} - \frac{k_{IN,SQ} k_{FB,IN}}{k_{FB,SQ}}, \tag{4.14}$$

L_{in} is the geometric inductance of the input coil, and $1/g_{J\Phi}$ is the dynamic inductance of the SQUID. The factors $k_{IN,SQ}$, $k_{FB,IN}$ and $k_{FB,SQ}$ are the couplings between the input, feedback and SQUID inductances. The imaginary part of Eq. 4.13 gives an effective inductance that is smaller than L_{in}. The real part is a new resistive term that is usually negative [77]. To simplify Eq. 4.13, we define variables $L_{eff} = L_{in}(1 - k_{IN,SQ} k_{FB,IN}/k_{FB,SQ})$ and $R_{in} = L_{in} \tau_{FLL} l_{FB}$. The circuit impedance then becomes

$$Z_{circ} = Z_{TES} + R_L + \omega^2 R_{in} + i\omega L_{eff}. \tag{4.15}$$

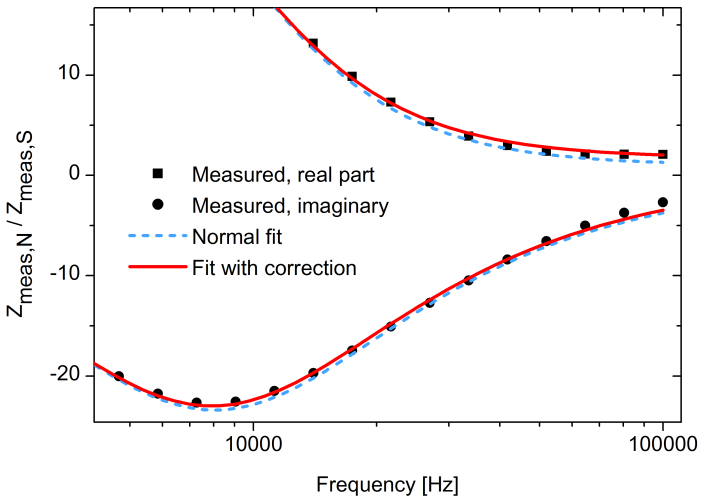

FIGURE 4.17 The fit to the ratio of normal and superconducting state impedance is slightly improved when a correction to SQUID input impedance is used.

Now we can use the same procedure as in the previous section and fit to obtain the circuit parameters, see figure 4.17 . The corrected transfer function is then (using

normal state data as an example)

$$G(\omega) = \frac{Z_{meas,N}}{R_N + R_L + \omega^2 R_{in} + i\omega L_{eff}}. \tag{4.16}$$

To obtain the TES impedance in transition, we can use the corrected transfer function as before to find Z_{circ} and finally calculate Z_{TES} using Eq. 4.15. The small correction by R_{in} does seem to help in bringing Z_{TES} obtained from N and SC transfer functions closer, especially lower in the transition as shown in figure 4.18. The value of R_{in} is very small and varies a lot between experiments. Again, the effect is smaller for the N based $G(\omega)$. Although this correction seems promising, so far we have not had the confidence to use it extensively in modeling, apart from some comparative tests.

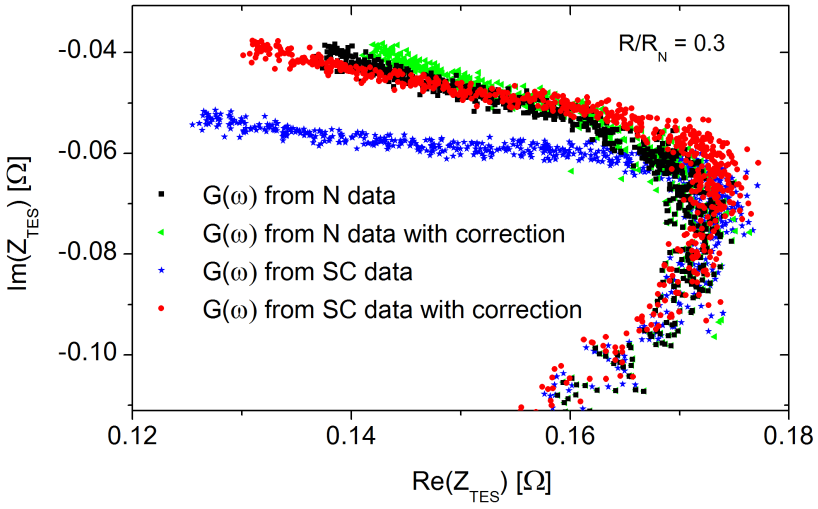

FIGURE 4.18 Zoom into the high frequency region of TES impedance showing the effect of corrected SQUID input impedance. This example is one of the best results, in terms of having the two different transfer functions produce similar Z_{TES} curves. The data is from the OTES discussed in section 6.3.1.

4.8 Determining Z_∞ from low frequency data

A constantly occurring problem in analyzing our impedance data is the difficulty in fixing Z_∞. It would be very useful to know with certainty where the high frequency limit is, because it directly gives β which is an important parameter. Furthermore, knowing Z_∞ greatly helps in selection of a thermal model to describe the system. In some measurements it can be almost impossible to say with confidence where Z_∞ is located. Even data that looks simple can be well fitted using very different models

that lead to completely different conclusions about the system and possible noise sources. The problem is illustrated in figure 4.19.

Depending on the detector, there can be effects that are only seen at very high frequencies but we are limited by the electric cut-off of the measurement circuit to frequencies below 100 kHz. It would be useful to have a way to determine β from low frequency data alone. The traditional $\alpha_{tot,IV}$ alone is not enough, as is evident from Eq. 2.24. In article A.IV we have presented an idea for a new method that could be used to obtain α and β. Our idea is based on performing a measurement of dI/dT_s. That is, the change of TES current when bath temperature T_s is changed, with the TES voltage bias held constant. An example of the measurement is shown in figure 4.20.

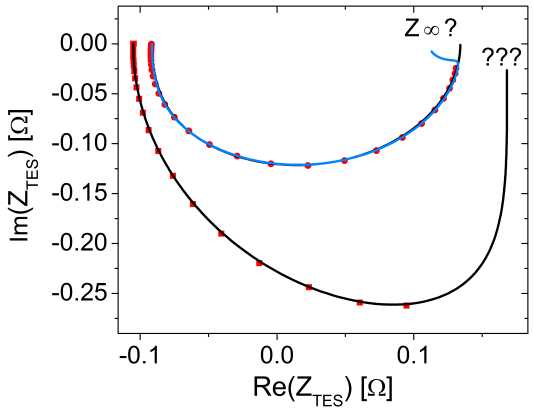

FIGURE 4.19 Examples of the problem of finding Z_∞. Red symbols are measured data up to 100 kHz and lines are fits calculated up to 2 Mhz. The datasets are from different pixels. The inner curve looks simple and can be explained equally well by two different thermal models with different Z_∞. The outer curve shows how deciding which Z_∞ to use is sometimes a difficult judgement call.

We note that in reference [78] a whole three dimensional surface was measured but here we are only interested in probing a single point with certain T_s and bias V_0. This point would of course correspond to settings used in measuring impedance and noise data.

It can be shown after some algebra that the derivative is given by

$$\frac{dI}{dT_s} = -\frac{g_s}{V_0}\left[1 - \frac{R_s}{R_0} + \frac{n}{\alpha\phi}\left(\beta + 1 + \frac{R_s}{R_0}\right)\right]^{-1}, \tag{4.17}$$

which can be used with Eq. 2.24 to solve for α or β that only depend on DC param-

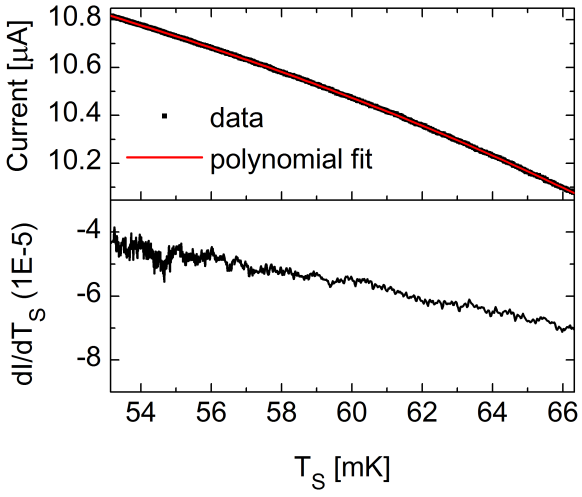

FIGURE 4.20 Determining the effect of bath temperature on TES current with constant voltage bias. The derivative dI/dT_s can be obtained directly from the measured data (bottom) but less noisy results are obtained by first fitting a polynomial to the data and taking a derivative of the fitted curve.

eters. For example, the solution for α is

$$\alpha = \frac{n}{\phi}\left[\frac{\mathcal{L}_{tot}(1 - R_s/R_0) + 1 + R_s/R_0}{(\mathcal{L}_{tot} - 1)\left(1 - R_s/R_0 + g_s/V_0\frac{dI}{dT_s}\right) + 2}\right] \tag{4.18}$$

where we have introduced a "total loopgain" $\mathcal{L}_{tot} = \alpha_{tot,IV}n/\phi = g_0T_0/\alpha_{tot,IV}P_0$. Finally, β can be calculated using Eq. 2.29. We can also find dI/dT_s in terms of the Z limits by inserting Equations 2.29 and 2.31 into 4.17:

$$\frac{dI}{dT_s} = \frac{g_s}{I_0}\frac{Z_\infty - Z_0}{(Z_\infty + R_0)(Z_0 + R_s)} \tag{4.19}$$

and then solve for Z_∞, assuming that Z_0 can be measured accurately:

$$Z_\infty = \frac{R_0I_0\frac{dI}{dT_s}(Z_0 + R_s) + g_sZ_0}{I_0\frac{dI}{dT_s}(Z_0 + R_s) - g_s} \tag{4.20}$$

Unfortunately, the equations turn out to be very sensitive to changes in the parameters. This means that all data has to be measured very carefully to obtain accurate values. The biggest problem is the high sensitivity to n. It is doubtful if we could ever determine it accurately enough. On the other hand, if one is confident that Z_∞ can be measured with reasonable accuracy, the logic can be reversed and the above equations can be used to determine n (and K) instead. The benefit of this trick would be the ability to check n at each bias point, if there is a reason to suspect

that it is not constant through the transition.

4.9 Thermal model fitting

The actual models that have been used will be discussed in the next chapter. The measured impedance and noise data are fitted *simultaneously* to the equations of a chosen model. We emphasize that the fitting is done by eye, and free fit parameters are varied manually, as high-dimensional non-linear least-squares fitting would be demanding to implement. We try to obtain fits where all of the Z and noise features are explained by the thermal model but in some cases it is not possible. In those cases we have quantified the remaining excess noise (if possible) as excess Johnson noise using the M-parameter [34]. Apart from the M parameter, the noise calculations have no free parameters, everything is fixed by the fits for impedance.

Note also that although we only show the complex plane plots of Z, we make sure that the real and imaginary parts fit separately as a function of frequency. Included in the fits, but not shown in the plots because of their small values, are the Johnson noise of the shunt resistor, and the equivalent white input noise of the SQUID (4 pA/$\sqrt{\text{Hz}}$). We have also used the equation for the non-equilibrium TES Johnson noise [27] in the analysis for all the devices. Even though Z is measured only up to 100 kHz, the theory curves are always calculated up to (at least) 2 MHz, in order to see the high-frequency behavior of the fitted models.

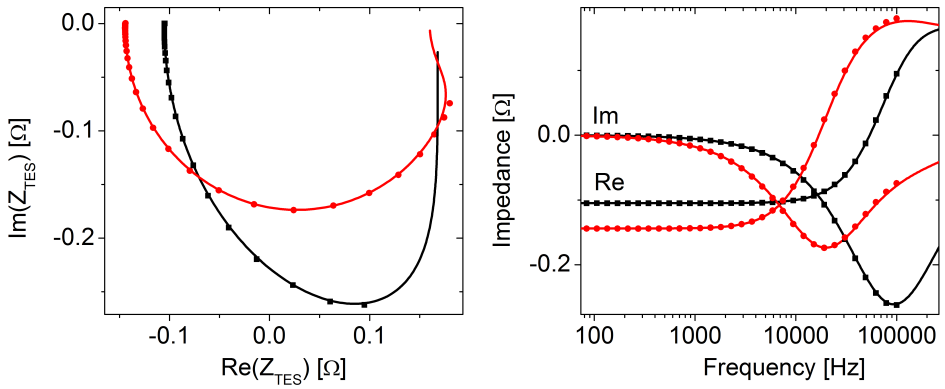

FIGURE 4.21 Although we usually only show Z data in the complex plane (left), during fitting we also make sure that the frequency dependence of real and imaginary components (right) is correct.

Chapter 5

Thermal models

In this chapter we present thermal models that can be used to describe a TES more accurately than by using the simple model of Fig. 2.1(a). There are several reports where various models are presented, which indicate that at least two [79–81] and often even more [60, 82–86] blocks are needed to fully fit the measured impedance and noise data. The problem with increasing the complexity of a model is that the number of free parameters quickly becomes so large that it is either very difficult, or simply impossible to obtain reliable values. Then one has to rely on theoretical calculations to estimate some parameters, or use other experimental methods to find them. Also, the more complex a model is, the easier it may be to fit the measured data even though the fitting parameters can actually be wrong.

It is therefore desirable to keep the used model as simple as can be physically justified and then maintain a certain amount of healthy skepticism towards the obtained fit parameters. This is especially true if the system under study has two (or more) additional thermal bodies whose heat capacity and thermal links to the TES are close to each other (see for example Fig. 5.6(b)). In such cases it may be impossible to separate the effects of the blocks and one could get misleading results by fitting to measured data using a model that only has one extra block, for example.

Another problem could be the presence of noise sources that have only a weak effect on the impedance. If such excess noise term is not a dominating one, it may still be easy to find a reasonable thermal model that fits both impedance and noise data. This is something that we need to keep in mind, because in this work we are trying to explain all the observed features in measured data by a relatively simple model. Sometimes we do have measurements where all the noise cannot be accounted for by ITFN noise arising from our thermal model, assuming there are no errors in data or analysis. In those instances we have used the M term to quantify the remaining excess noise level, although it sometimes fails to produce the correct frequency dependence for the noise. If such unexplained noise is present in some

measurements, one may wonder if it exists in all data – we may simply be unable to see that it is there.

A possible answer to these worries is presented in Ref. [87], where the authors have introduced the concept of an equivalent bolometer. In this method one does not obtain information about the internal details of the system. Instead, everything is lumped into a single frequency dependent heat capacity. The lumped model can then be used to predict the largest possible ITFN noise that can be produced by the system and if the result is less than the actually measured noise, one may conclude that there is some excess noise. While the equivalent bolometer model can provide useful information, it is unclear at this stage if it actually holds for every possible model (when all blocks are not at the same temperature).

5.1 Two blocks

The first extension of the simplest calorimeter model is obtained by adding one block either hanging from the TES or between TES and heat bath as illustrated by figure 5.1. Analytical equations have recently been developed for thermal models with two and three blocks. The details and derivation of our models will be published elsewhere [88]. We will not present the equations for the two-block models here, as they can be taken as limits of the three-block equations that will be given in section 5.2.

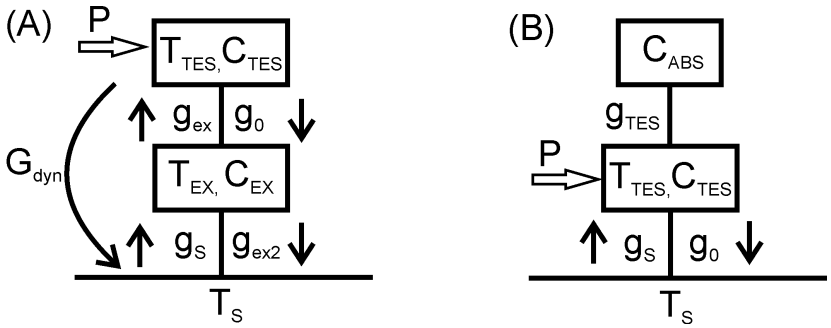

FIGURE 5.1 Thermal block models for (A) TES with an intermediate heat capacity and (B) hanging, or dangling, heat capacity attached to a TES. The Joule power P of the TES bias current is dissipated inside C_{TES}. The intermediate body could be the SiN membrane or the TES phonon system, for example. The hanging block could represent an absorber or other extra structures on top of a TES. In (A) G_{dyn} is the conductance that can be calculated from $I - V$, in (B) $g_0 = G_{dyn}$

We have found that the two-block models are usually too simple to explain our data. Before jumping to more advanced models we discuss some aspects of our

models here because the same logic will hold for other models where these blocks are included.

5.1.1 Intermediate body

We label the intermediate thermal mass with "EX" (as in excess) and it is characterized by its temperature T_{EX} and heat capacity C_{EX}. We emphasize that we do not make the simplifying assumptions that $T_{EX} = T_{TES}$ or that $T_{EX} = T_{bath}$, when the TES is biased. Associated with the intermediate block, we have thus not only two, but *four* dynamic thermal conductances $g_{ij} = dP_i/dT_j$. The parameters $G_{dyn} = dP/dT_{TES}$ and T_{TES} can be calculated from measured $I - V$ curves, as discussed before.

In our fitting procedure we use T_{EX}, C_{EX} and g_0 as the free parameters. The other unknown conductances g_{ex}, g_s and g_{ex2} are then calculated using the free parameters and the known values of T_{TES} and G_{dyn}, as [88] $G_{dyn} = g_0 g_{ex2}/(g_{ex} + g_{ex2})$. To simplify the model and to minimize fitting parameters, it is also assumed that the links on both sides of the intermediate block have the same thermal exponent n, i.e. we use $g_0 = AT_{TES}^{n-1}$, $g_{ex} = AT_{EX}^{n-1}$, $g_{ex2} = BT_{EX}^{n-1}$, and $g_s = BT_{bath}^{n-1}$. This is physically reasonable if all the conductances are dominated by the phononic transport properties of the SiN membrane. Our data so far is consistent with the assumption that the intermediate body is really related to the membrane.

It is worthwhile to discuss one simplification to the thermal model that is done at this stage. It could be argued that the phonon system of the TES (and an absorber if present), should be included in the model. The situation, however, is not entirely simple. At sub-Kelvin temperatures, the phonon wavelengths can be longer than the TES film thickness and it is unclear if the TES phonon system exists as a separate entity or if it is directly coupled to the phonons of the underlying SiN lattice. Because the heat capacity of the TES phonon system is very small, we simply lump it into the intermediate heat capacity together with SiN. If there is a significant contribution to g_0 from electron-phonon coupling or from Kapitza resistance between the phonon systems, our values for g_0 will be a combination of the series conductances. It may be possible to probe for the role of electron-phonon coupling by looking for changes in g_0 when TES film thickness is varied or when a thick absorber is added.

As an example why good I-V data at the true DC limit, together with dI/dT_s data, is valuable in the analysis, we point out the situation shown in Fig. 5.2. There we illustrate how we cannot take even the position of Z_0 as trivially obtained from low frequency Z data. We could use realistic values for the parameters to model an impedance curve that exhibits a sudden kink inwards just at the lowest frequency of

our measurement so that we would not be able to observe it with our current Z data taken down to 10 Hz. The noise data would also show a decrease at low frequency that we would not be able to see. If we now settle for the apparent Z_0, we end up with α that is too small (57 instead of 87 from the "real" Z_0 in this example). C_{EX} value used in the calculation was $1 \cdot 10^{-10}$ J/K and $g_0 = 1.9 \cdot 10^{-9}$ W/K when G_{dyn} was $1.25 \cdot 10^{-9}$ W/K. The thermal model restricts us so that we can only use values of g_0 that are larger than G_{dyn}. For cases where an additional body can be justifiably attached to the intermediate body (dangling from it or in series), we could perhaps be able to move the kink to even lower frequency. We note that if one observes thermal cross-talk between pixels in closely packed arrays [89,90], it means that the other pixels can be thought of as part of the thermal circuit of any one pixel and could possibly cause such a low frequency feature to the impedance.

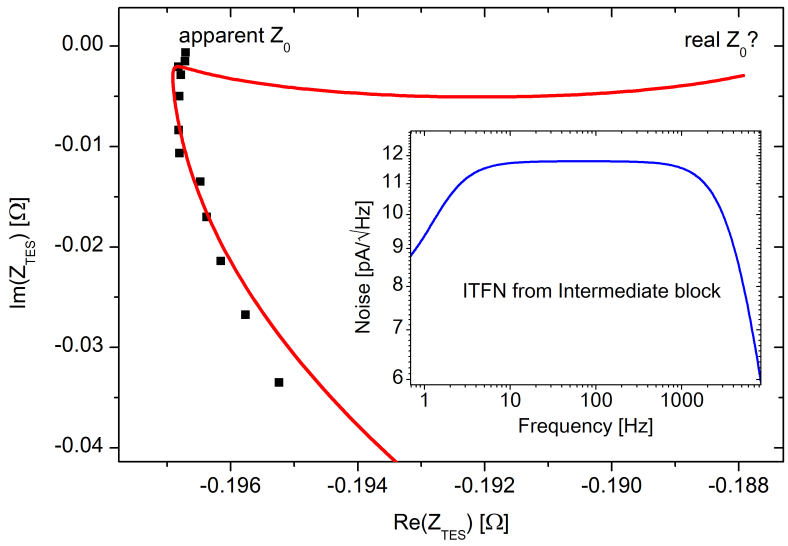

FIGURE 5.2 Possible complication in determination of Z_0 caused by the intermediate body. The sharp kink in calculated Z (red line) happens at 10 Hz in this example.

5.1.2 Hanging body

In contrast to the intermediate body, in case (B) the possible heat capacity C_{ABS} is hanging, which means that no steady state power flows through it, and the average values of T_{TES} and T_{ABS} are equal. This simplifies the description in comparison to the intermediate body, as only one thermal conductance g_{TES} is required. The Joule power of the TES bias current is all assumed to be dissipated inside C_{TES}.

In real X-ray and γ-ray devices with thick absorbers on top of the TES film, as shown in article A.V and for example Ref. [60], C_{ABS} could well be the absorber. In such cases g_{TES} describes the thermal conduction between the TES and the ab-

sorber. In devices without an absorber (most samples in this work), g_{TES} models the thermal conduction within the TES film.

We note that in the case of an absorber, the assumption of equal temperatures does not hold when a photon is absorbed. During the event T_{ABS} can temporarily be higher than T_{TES} and an increase in the ITFN noise may be observed, leading to degradation of achieved energy resolution.

To give a feel of how the impedance and ITFN noise from C_{ABS} depends on some of the parameters, we present calculated Z and noise curves that are based on one measured dataset, and we vary one parameter at a time, but keep the bias point constant. The effect of g_{TES} is shown in Fig. 5.3. We can clearly see how the ITFN level goes down when the link gets better (higher conductance) and how it starts to look like a white noise component within the bandwidth of the measurement. The plot is slightly misleading because it includes the electrical cut-off of the read out circuit, which masks the true roll-off of ITFN at high frequency. If the circuit effect was removed, we would see that as the noise level comes down, the roll-off moves to higher frequencies. With large enough g_{TES} the impedance curve starts to resemble that of the simplest model and only a small kink is seen at the highest frequencies well above 100 kHz.

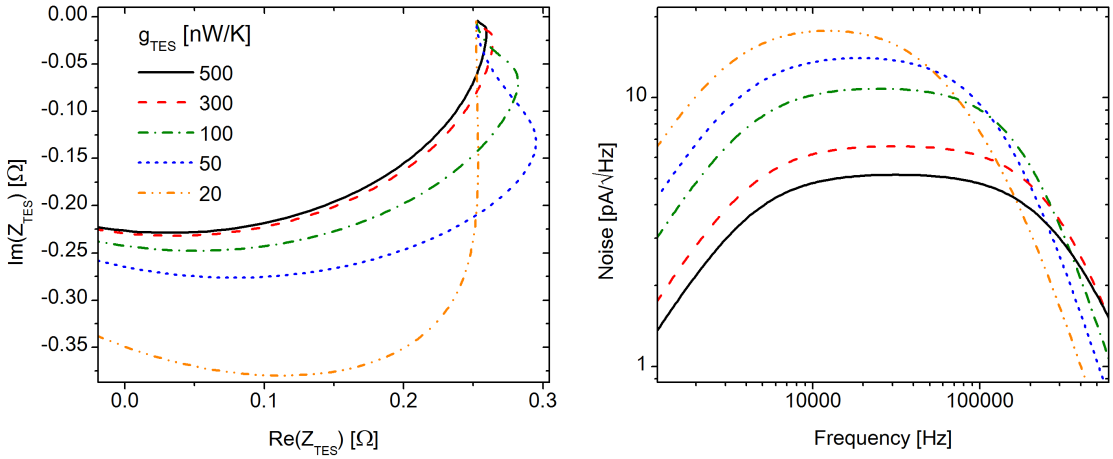

FIGURE 5.3 The effect of g_{TES} on the impedance (left) and ITFN noise component (right). C_{TES} was held constant at 0.15 pJ/K and C_{ABS} was 0.36 pJ/K. In this case α was 58.

Figure 5.4 illustrates how increasing C_{ABS} brings ITFN noise up and moves the rising slope towards lower frequencies. Here g_{TES} was low enough that it determines the high frequency roll-off. With a large value the Z data becomes very distorted. The effect of changing C_{TES} is given if Fig. 5.5. Now the noise level goes up if C_{TES} becomes smaller, and if it is small enough we can observe an interesting peak at high frequency, which we shall discuss more in section 5.3

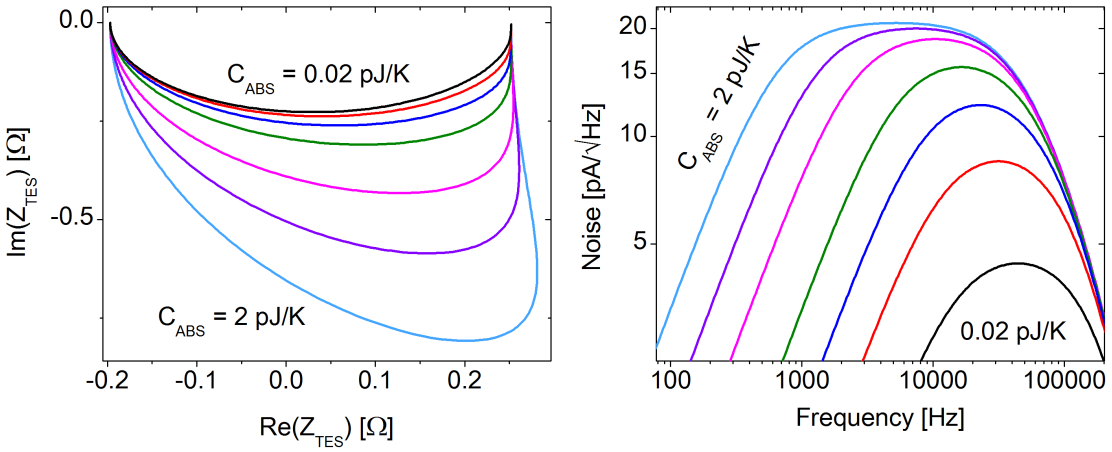

FIGURE 5.4 The effect of C_{ABS} on the impedance (left) and ITFN noise component (right). The values of C_{ABS} were 2, 1, 0.5, 0.2, 0.1, 0.05 and 0.02 pJ/K. C_{TES} was held constant at 0.15 pJ/K and g_{TES} was 20 nW/K.

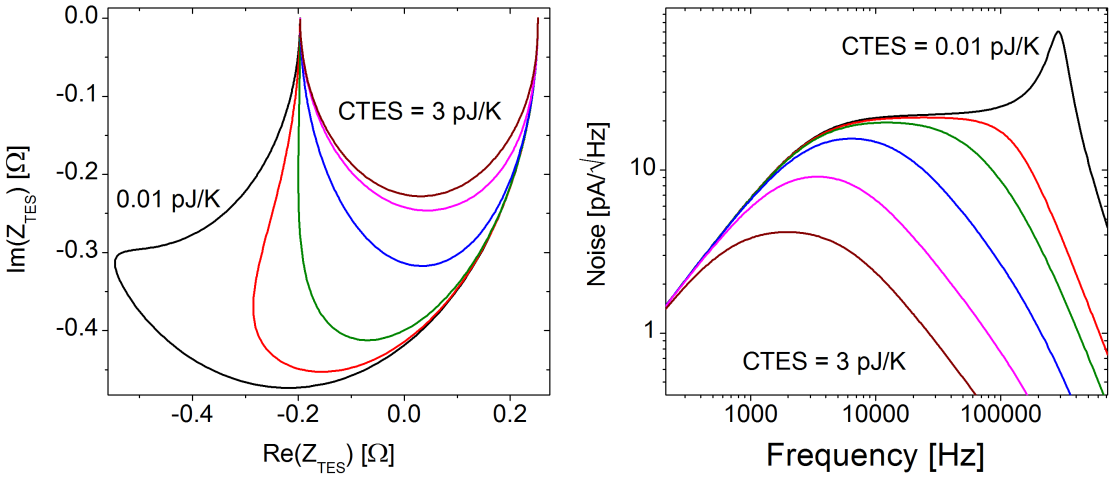

FIGURE 5.5 The effect of C_{TES} on the impedance (left) and ITFN noise component (right). The values of C_{TES} were 3, 1, 0.3, 0.1, 0.05 and 0.01 pJ/K. g_{TES} was held constant at 10 nW/K and C_{ABS} was 0.3 pJ/K.

5.2 Three blocks

A thermal model with three bodies is often seen to fit our data well. Figure 5.6 shows the simplest two models for three blocks. Equations for impedance and noise have been derived for both cases but we only show the intermediate + hanging (IH) model here. The equations were derived by writing down the electrical differential

equation for the TES (Eq. 2.4) and thermal differential equations for each block i, $C_i dT_i/dt = \sum_j P_j$, where P_j are the different power inputs and outputs, linearizing them with respect to temperature, and solving them analytically. More detail will be presented in a future publication [88].

Typically the measured data can be fitted equally well with either model, and only the obtained parameter values will be slightly different. We argue that it is more difficult to physically justify the model of two hanging blocks (2H), especially in the case of a TES without absorber or other extra features. We operate under the assumption that the intermediate block originates from the SiN membrane and the hanging one shall remain unspecified for now.

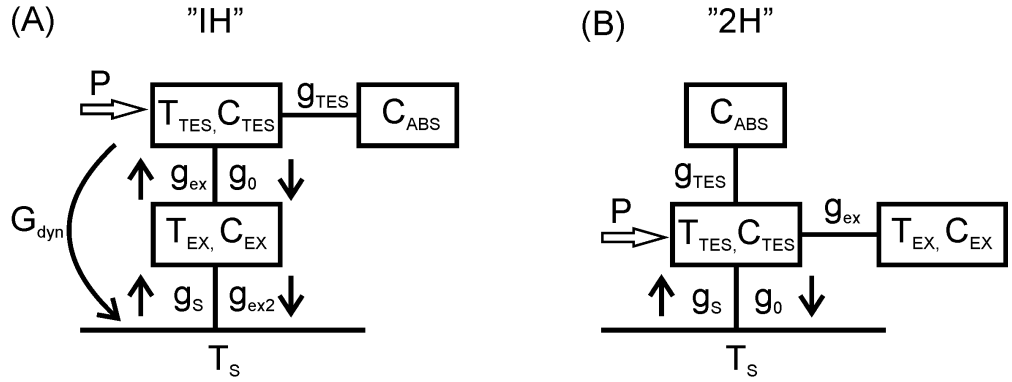

FIGURE 5.6 Three-body thermal models used in this work. The IH (Intermediate + hanging) model is the one that has mainly been used in this work.

The complex impedance of the IH model can be shown [88] to be

$$Z_{TES} = R_0(1+\beta) + \frac{\mathcal{L}}{1-\mathcal{L}} \frac{R_0(2+\beta)}{1 + i\omega\tau_I - A(\omega) - B(\omega)}, \tag{5.1}$$

where

$$A(\omega) = \frac{1}{1-\mathcal{L}} \frac{g_{tes}}{(g_{tes}+g_0)} \frac{1}{1+i\omega\tau_{abs}} \tag{5.2}$$

$$B(\omega) = \frac{1}{1-\mathcal{L}} \frac{g_0 g_{ex}}{(g_{tes}+g_0)(g_{ex}+g_{ex2})} \frac{1}{1+i\omega\tau_{ex}}, \tag{5.3}$$

and the loopgain and time constants are defined as $\mathcal{L} = P_0\alpha/[(g_{tes}+g_0)T_0]$, $\tau_I = \tau_{tes}/(1-\mathcal{L})$, $\tau_{tes} = C_{tes}/(g_{tes}+g_0)$, $\tau_{abs} = C_{abs}/g_{tes}$ and $\tau_{ex} = C_{ex}/(g_{ex}+g_{ex2})$.

For noise, we discuss here three major classes of unavoidable noise sources: the power fluctuations in the thermal circuit, the electrical thermal noise of the detector (Johnson noise), and the Johnson noise of the shunt resistor. We disregard correlations between fluctuations in the thermal conductances.

The frequency dependent current responsivity $s_I(\omega)$ for power input in the TES heat capacity C_{tes} can be written [88] as

$$s_I(\omega) = -\frac{1}{Z_{circ} I_0} \frac{Z_{TES} - R_0(1+\beta)}{R_0(2+\beta)}, \tag{5.4}$$

where Z_{circ} is the Thevenin equivalent circuit impedance given by Eq. 2.25. Now the thermal fluctuation current noise terms (one phonon noise term and two ITFN terms) are

$$|I|^2_{ph} = P^2_{ph} |s_I(\omega)|^2 \frac{g^2_{ex}}{(g_{ex} + g_{ex2})^2} \frac{1}{1+\omega^2\tau^2_{ex}}, \tag{5.5}$$

$$|I|^2_{ITFN,ABS} = P^2_{tes} |s_I(\omega)|^2 \frac{\omega^2\tau^2_{abs}}{1+\omega^2\tau^2_{abs}}, \tag{5.6}$$

$$|I|^2_{ITFN,EX} = P^2_{ex} |s_I(\omega)|^2 \frac{g^2_{ex2}/(g_{ex2}+g_{ex})^2 + \omega^2\tau^2_{ex}}{1+\omega^2\tau^2_{ex}}, \tag{5.7}$$

where $P^2_{ph} = 2k_B(g_{ex2}T^2_{ex} + g_s T^2_s)$, $P^2_{tes} = 4k_B g_{tes} T^2_0$ and $P^2_{ex} = 2k_B(g_0 T^2_0 + g_{ex} T^2_{ex})$. By writing the noise powers P^2_{ph} and P^2_{ex} this way, we implicitly assume a discrete model with a sharp temperature drop between blocks. However, if some of the thermal links describe an effective network model (diffusive case) these noise powers are modified, as discussed in Ref. [88].

The non-equilibrium Johnson current noise [27] in the TES film is given by

$$|I|^2_J = V^2_\omega \Bigg/ \left| R_0(1+\beta) + R_L + i\omega L + \frac{\mathcal{L}(R_0 - R_L - i\omega L)}{1 + i\omega\tau_{tes} - (1-\mathcal{L})(A(\omega) + B(\omega))} \right|^2, \tag{5.8}$$

where $V^2_\omega = 4k_B T_0 R_0(1+2\beta)$. Or alternatively, using impedance that we get from fits to the Z data:

$$|I|^2_J = V^2_\omega \Bigg/ \left| Z_\infty + (R_0 - R_L - i\omega L) \frac{Z_{TES} - Z_\infty}{Z_{TES} + R_0} \right|^2 \tag{5.9}$$

The Johnson noise due to the shunt and parasitic resistances is simply

$$|I|^2_{sh} = V^2_{\omega,sh} / |Z_{circ}|^2, \tag{5.10}$$

with $V^2_{\omega,sh} = 4k_B T_{sh} R_L$ if both the parasitic resistance and the actual shunt are at temperature T_{sh}.

Depending on the details of the thermal circuit, it could be difficult to distinguish the two ITFN noise terms from each other. Fortunately, in our data they fall

on clearly different frequency ranges and their effects can be observed. The intermediate block is partly responsible for the low frequency noise level and sometimes a bump in the mid-frequencies (typically 1 kHz - 10 kHz in our case). The effect of C_{EX} can be difficult to see, but sometimes it is easily observed, as shown in figures 5.7 and 5.8. A high frequency component (above 10 kHz) is also always present and this can be modeled with the hanging body. The difference between ITFN and M noise for the high frequency noise component is subtle, as shown in Fig. 5.7. However, because M does not show up in impedance, we can in many cases argue that because a three-block model is needed, ITFN is the correct choice to explain the noise.

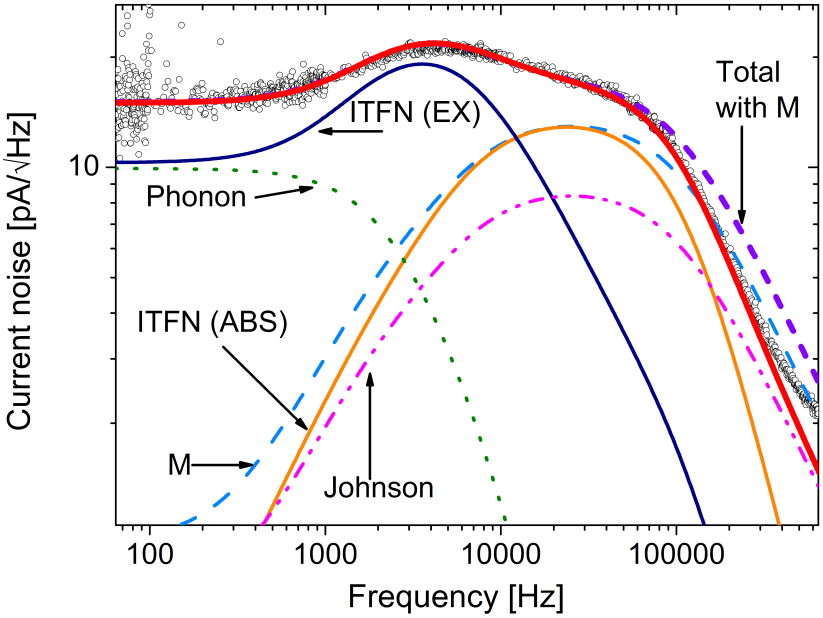

FIGURE 5.7 Measured noise spectrum (symbols) with theoretical noise terms (lines). It is clearly seen how the two ITFN components occur at different frequency ranges. Also evident is that a two body model alone could not explain this noise data. Notice that M and ITFN(ABS) are not included simultaneously. Instead, looking at the total noise with M (dashed line) and ITFN (solid red line) we see the small difference between M and ITFN in the roll-off of the high frequency noise.

5.3 Decoupling of N and S phases

We turn our attention now to the hanging part of the IH model that was unidentified so far. During this work a lot of fitting was done on data from various detectors, initially using a two body thermal model. It became evident that in order to explain the observed data by ITFN without an M noise term, in many cases there were certain general trends seen. First of all, C_{ABS} needed to be larger than C_{TES}, especially when operating low in the transition. The heat capacities also were not constant but

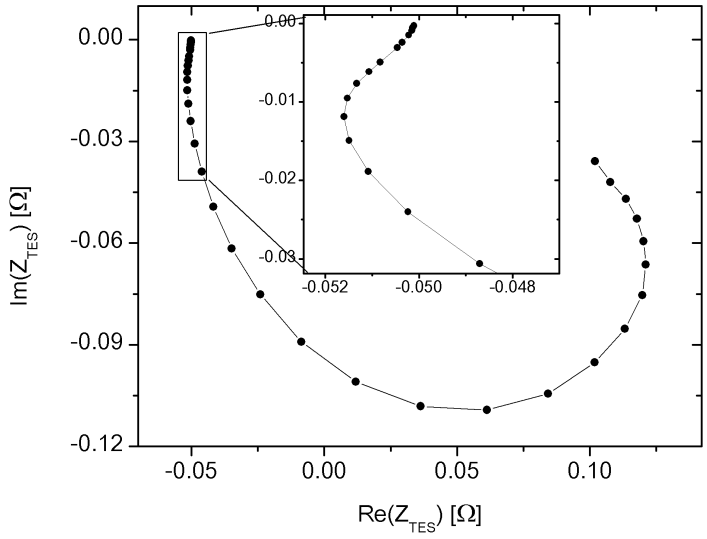

FIGURE 5.8 The presence of the intermediate body can be seen by zooming in on the low frequency Z data. The effect is not always as obvious, but can be seen in most of our data.

needed to change considerably. Often, when biased very low in transition, C_{TES} had to be surprisingly small. Additionally, a typical trend was that g_{TES} did not stay constant and most of the time needed to decrease when going towards superconducting state.

When such behaviour is observed in bare detectors where no extra features are added, one has to ask: apart from the N and S phases, what else do we have left that could explain the observations? We cannot find a better explanation and therefore conclude that we are observing the thermal decoupling of the superconducting regions of a TES from the normal state areas at high frequency. In this case the block that has been labeled as the TES would represent the normal state area inside the TES film, because Joule heating occurs there, and the hanging block models the superconducting part of the TES film. In section 6.3 we will review our recent result with the IH model that provide experimental evidence to support this picture.

An accurate theoretical explanation of what exactly is happening in a TES film biased in the superconducting transition is beyond the scope of this work. However, there have been recent advances in describing the transition using weak links [54, 55, 91]. Here we discuss on a more general level some aspects of the phenomenon. We note that the curious peak in noise that appeared in the calculations shown in Fig. 5.5 is regularly observed in experimental data. It arises naturally from our model due to a resonant-like interaction between the electrical and thermal circuits, and is observed when the decoupling of C_{ABS} begins at a frequency (given by time constant τ_{abs}) slightly below the electrical cut-off of the readout. Then, if

C_{TES} is very small and the TES has a large enough α, the TES response becomes extremely sensitive to fluctuations. The increased responsivity means that all noise sources develop a peak, including the Johnson noise as shown in Fig. 5.9.

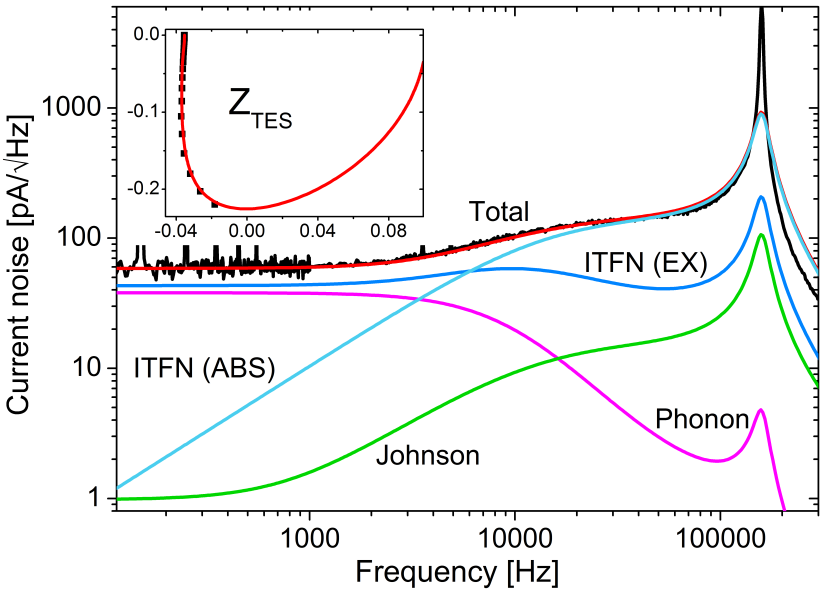

FIGURE 5.9 A resonant-like peak in the high frequency noise is often observed and can be explained by our model. The data shown here is the most extreme case measured, typically the peak is less pronounced. The data is from CTES 2 discussed in section 6.3.3, from fits the relevant parameters were: $\alpha \approx 430$ and C_{TES} = 17 fJ/K. Notice how all noise terms exhibit the peak. Inset: corresponding impedance data and IH model fit.

5.3.1 Hanging heat capacity C_{ABS}

According to the BCS theory, the heat capacity of a superconductor has a sudden jump at T_c where the value is 2.43 times that of the material at normal state [61]. On the other hand, according to Ref. [62], for thin proximity coupled bilayers the jump in heat capacity is reduced. For Ti/Au the jump should be 73 % of the BCS value. In fits to our data, C_{ABS} is a free parameter and when the obtained fitted values are plotted together with theoretical calculations we often find that the measured data is closer to the reduced BCS heat capacity.

It is straightforward to calculate the heat capacity in the case of a CorTES, because we know the volumes of the N and S phases from Eq. 3.1. With a square TES we do not really know how the superconducting transition develops, and it is not trivial to convert a measured resistance at any bias point to information about the volume of N and S phases. The transition can also behave differently for Ti and Mo based devices. If the S phase does not grow as one uniform region (when coming

from the N side to lower temperature) but instead has several separate S areas, it is unclear how accurately the (still quite simple) IH model can model a sum of the separate S volumes. In section 6.3.4 we have used a crude linear estimate for the transition of a square TES, where the ratio of the volumes of the N and S phases is given directly by the scaled TES resistance R/R_N. In our model it is thus expected that phase separation does inevitably occur inside the TES film.

5.3.2 Thermal link g_{TES}

The most difficult aspect of our model is to predict how the thermal conductance g_{TES} should behave as a function of bias point. A naive and straightforward guess would be to simply claim that it depends on the contact area between the two phases. For example, in a CorTES the contact area is the circumference of a circle given by the phase boundary radius r_b multiplied by film thickness. The contact area would then have an exponential dependence on TES resistance. In a square TES the situation would be more complicated to predict because we do not know the details of the transition.

The question then is, does such a contact area really exist? In terms of thermal conductance within the TES film, nothing dramatic should happen at the boundary as the thermal conductance of a superconductor at exactly T_c is the same as in the normal state. Because the boundary is at T_c, the superconducting gap Δ is zero and electrons are free to enter the superconductor, where they are either converted to Cooper pairs or remain as individual quasiparticles. The quasiparticles are responsible for the thermal conductance in the S phase but they do not participate in the current transport, which is now handled by the Cooper pairs. If there were a temperature gradient in the S phase (see next section), the thermal conductance would begin to slowly decrease when going deeper inside the superconducting region and simultaneously Δ would increase.

Whether g_{TES} is the transport between the phases or if it describes some effective internal thermal conductance in the S phase (or the whole TES), a fact is that there is an abrupt change at the phase boundary where the "excess" heat capacity appears. We will therefore settle to the notion that we have two separate systems, C_{TES} and C_{ABS} with a thermal link g_{TES} between them and leave a more exact theoretical inspection for possible future work.

5.3.3 Advanced thermal model

The hanging block in the IH model is naturally still a simplification, in reality there is also a thermal coupling from C_{ABS} directly to the bath or to C_{EX}. However, the

missing link, which we expect to have a magnitude of the order of g_0, is believed to have only minor effect for the devices studied here, where g_{TES} is much larger than g_0. Any effects of temperature gradients within the TES film are also not captured in this simple model. One consequence of using the IH model, where the S phase is assumed to be at temperature T_{TES}, could be that the obtained heat capacity value for C_{ABS} is an effective value that depends on the possible temperature gradient inside the S phase. Recalling that after the jump in heat capacity, BCS theory tells us that it decreases rapidly after T_c. Numerical estimates of the gradients within a CorTES device [35] have shown that the isothermal simplification is a reasonable assumption.

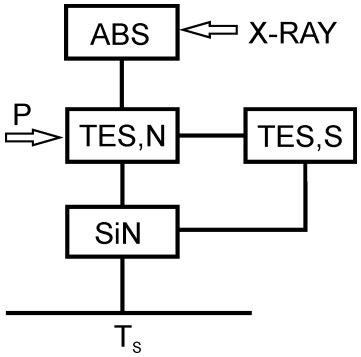

FIGURE 5.10 An advanced thermal model for a CorTES with an absorber and taking into account the link from S phase to SiN phonons.

In figure 5.10 we present a possible thermal model that could perhaps better describe a CorTES that has an absorber deposited on it. We have not derived the equations for this case and we suspect fitting such a model would be difficult. If the thermal links from the N phase to the absorber and S phase are comparable, it may be impossible to reliably extract heat capacity values, as the features caused by the different bodies would be overlapping. On the other hand, unless the absorber is clearly dominating the heat capacity, using the IH model on such a system might produce good looking fits but the heat capacity and thermal conductance values obtained from the fit would be lumped values that include both the absorber and the S phase.

To conclude, in order to probe the N-S decoupling physics it is preferable to use a geometry that allows us to calculate theoretical estimates and the use of any additional features on the TES should be avoided.

5.3.4 Reducing the noise

From the three theoretical plots in section 5.1.2 we can see how each of the important parameters affects the ITFN noise level. According to our model, when a TES is biased lower in the transition, C_{TES} decreases and C_{ABS} increases. Both effects cause the ITFN to have a higher magnitude. In addition, fits to our data often show that the value of g_{TES} decreases when going to lower bias points, which further raises the ITFN level. Thus, it seems that no matter what we do, the magnitude of this ITFN term is always increased if we want to bias near the bottom of the transition.

However, assuming it is possible to engineer the values, we could perhaps find a design where the effect is minimized. A combination of large g_{TES} and C_{TES} with C_{ABS} as small as possible would give the lowest ITFN noise. Thus, we need to somehow make sure most of the TES stays in normal state or even add extra layers of normal metal with good thermal conductivity and in good thermal contact to the TES film. This way, up to the decoupling frequency of the S phase (given by τ_{abs} in the IH model), the extra features are still coupled well enough to the TES that they can be thought of as part of the N phase. With increased C_{TES}, the sensitivity of the TES to the power fluctuations coming from C_{ABS} would then be reduced. There is of course a risk that any added features will eventually also decouple from the TES, but if the thermal link is good enough this effect should be small. We note that the best designs in terms of reported energy resolution [36, 92] do indeed employ extra normal metal features whose role could perhaps be understood in light of this theory.

The need for a good g_{TES} suggests that Mo -based detectors should have less ITFN noise than Ti -based ones because they have better thermal conductances within the TES film. Another factor that could be important in the two materials is the way the films turn superconducting. As is discussed in Ref. [78], the heat capacity of a Ti/Au TES was measured to be closer to superconducting values, whereas a Mo/Au TES was said to be closer to normal state heat capacity throughout the transition. A possible explanation was given [78] in terms of the excess noise in a Mo/Au TES being caused by a percolation mechanism. Our model can explain the result by the more favorable N/S volume ratio of the Mo/Au TES.

In order to verify if our model could explain the excess noise in Mo -based TESs, the time constant τ_{abs} needs to be such that decoupling occurs below the electrical cut-off frequency of the readout circuit to make the effect more visible. This could possibly be obtained by making Mo devices with purposely higher sheet resistance and thus lowering g_{TES}. Or alternatively, one needs a readout setup where the cut-off is at high enough frequency.

Chapter 6

Experimental results

6.1 About FSN

The FSN noise theory is presented in article A.I. It was already discussed in Ref. [35] and we shall not go through the details again. FSN theory was developed before the emergence of complex impedance as an analysis tool, and the problem with the original FSN model is that it failed to correctly take into account the thermal model. The results presented here show evidence of a significant amount of ITFN noise in the CorTES design, which is guaranteed to exist, given the observed features in the impedance data. Therefore, the amount of noise that can be attributed to FSN is significantly reduced.

The good feature about the FSN theory is how it predicts a quick increase in the noise when approaching the superconducting state. We still observe that behavior but can mostly explain it by an ITFN component. However, sometimes something extra is needed and we have simply used the M parameter to characterize the excess noise in such cases. This leaves a window of opportunity for the FSN to bounce back into the picture, but so far we have not given any effort in updating the FSN model. Therefore we just leave it as a possible explanation for any M we encounter. We also note that in Ref. [93] the FSN was predicted to have a smaller effect than in our model.

In his work, Luukanen [35] discussed about a way to reduce the FSN effect by breaking the correlation of fluctuations. This can be achieved by cutting an OTES into parallel slices as we have done with the STES and XTES designs. FSN should decrease with the number N of parallel parts as $N^{-1/3}$ so for an XTES with 8 parallel slices we would expect to see FSN noise level halved and for STES it should be reduced by 0.63.

In figure 6.1 we plot data measured on O,S and XTES that were fabricated on

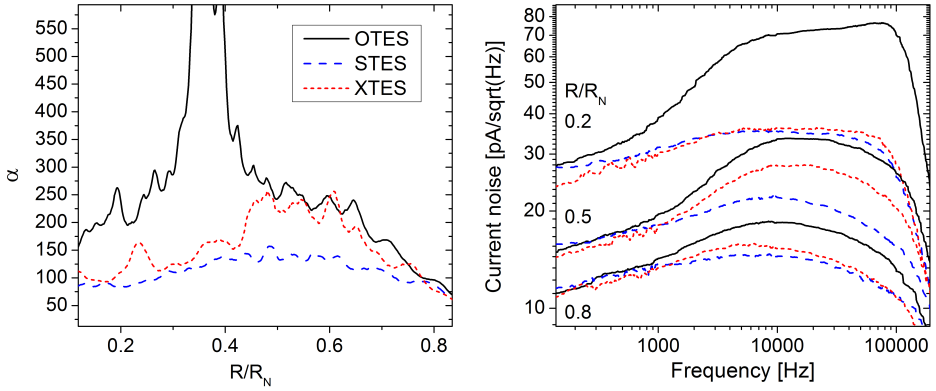

FIGURE 6.1 Comparison of the different CorTES geometries. Data is taken at 60 mK. Left: measured $\alpha_{tot,IV}$. Right: measured current noise at three different bias settings.

the same chip and thus should have identical Ti/Au films. We see the typical result that for some reason STES has the lowest $\alpha_{tot,IV}$. There are some places on the I-V where S and X have similar $\alpha_{tot,IV}$ and their noise levels are consequently very close. Rather than following the prediction about the effect of parallel parts, the noise level would appear to correlate more with $\alpha_{tot,IV}$.

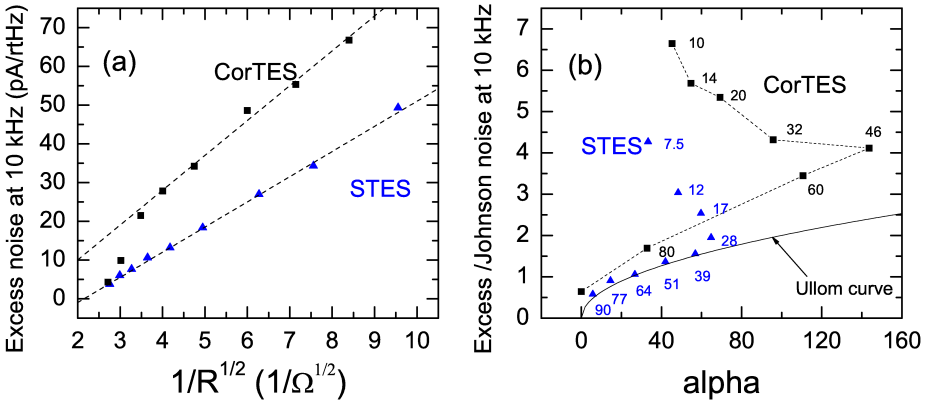

FIGURE 6.2 Old data from article A.II, comparing observed excess noise in OTES and STES. Alpha in (b) is the total alpha calculated from I-V. The "Ullom curve" refers to the phenomenological $M = 0.2\sqrt{\alpha}$ result from Ref. [34].

The results reported in article A.II could perhaps be seen as supporting the predicted reduction of FSN noise. Unfortunately we do not have impedance data on those detectors. It is hard to draw conclusions based on $\alpha_{tot,IV}$ alone, but the STES appears to have lower excess noise. However, after reviewing the data we have a reason to suspect that the I-V data is erroneous due to a failed temperature regulation during the I-V sweep, which affected the calculated $\alpha_{tot,IV}$. We cannot completely rule out the results of paper A.II but in light of our more recent result it is more difficult to understand. Those pixels did have somewhat lower R_N than

later ones and unlike all the CorTES pixels that we have Z data on, the old ones had a full Nb top layer without the hole. The old results on excess noise are presented in figure 6.2. In conclusion, no solid evidence for reduction of excess noise which resulted directly from the slicing has been seen.

6.2 Unexpected effect of the AlOx layer

Before diving into the thermal model fitting, let us first discuss a recent finding reported in article A.VI, that helps in understanding some older data. The CorTES design relies on the insulating AlOx layer to prevent the TES film from getting in contact with the top Nb layer. We had assumed that the AlOx layer has a low thermal conductivity and has negligible heat capacity compared to the TES, and consequently it was believed that it should have minimal effect on the performance of the TES. However, in paper A.VI we show that this assumption is not true. After having trouble explaining all the noise characteristics of the CorTES, we wanted to test if we could affect the noise properties of a square TES by adding AlOx on top of it. By what now seems like a fortunate mistake, in one sample the AlOx layer was too big so that it touched the bulk Si, as shown in figure 6.3. More crucially, even after realizing the error we still decided to do a noise measurement on this TES.

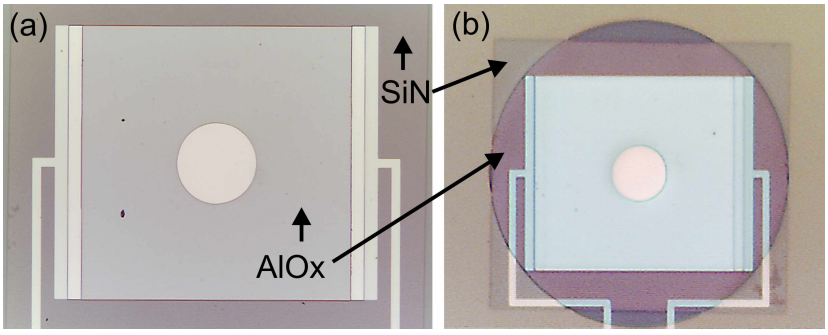

FIGURE 6.3 Optical microscope image of a square TES with a covering AlOx layer. (a) This TES has AlOx only on top of the TES. (b) AlOx extends over the SiN membrane. TES size is 300 μm and in both TESs the SiN and AlOx layer thicknesses were 750 nm and 120 nm, respectively.

What we found out was that the AlOx layer seems to have a surprisingly high heat conductivity. The 120 nm thick AlOx layer touches bulk Si only in certain regions and seems to have higher thermal conductance than the much thicker (750 nm) SiN. G_{dyn} curves shown in figure 6.4 compare the TES of Fig. 6.3b to an identical TES without AlOx. Furthermore, $\alpha_{tot,IV}$ was very different and showed large peaks with AlOx.

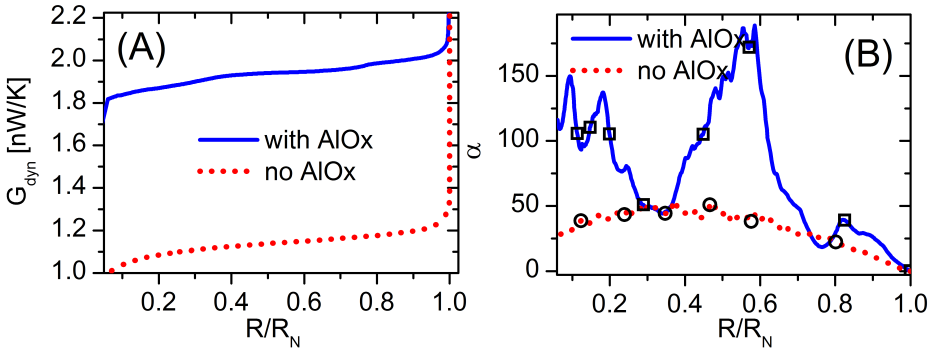

FIGURE 6.4 Dynamic thermal conductance (A) and total α (B) calculated from I-V measurement. The open symbols correspond to bias values where the noise spectra of Fig. 6.5 were measured.

As explained in paper A.VI, we calculated a crude estimate for the thermal conductance and got a value of $\kappa \sim 4.5 \cdot 10^{-6}$ W/cmK for AlOx and $\kappa \sim 1 \cdot 10^{-6}$ W/cmK for SiN. We are not aware of existing 0.1 K thermal conductivity measurements for AlOx but the obtained value is in the range that most amorphous glasses should fall in ($1 \cdot 10^{-5} - 1 \cdot 10^{-6}$ W/cmK at 0.1 K), according to Ref. [94].

Figure 6.5 shows the measured electrical noise of the pixels. Immediately obvious are the very large noise bumps in the pixel with large AlOx. They are related to the high values of α. Around the $R/R_N = 0.3$ bias point, the pixels have similar $\alpha_{tot,IV}$ but the AlOx pixel seems to have a slightly higher noise level. The feature around 10 kHz is similar to what we usually see in the Corbino devices. However, in a CorTES they are not quite so pronounced and center closer to 1 kHz, possibly because in a CorTES the AlOx layer that extends over the membrane is a narrow strip, making thermal conductance lower.

The TES where AlOx was only on top of the TES film is unfortunately more difficult to comment on because the AlOx deposition made T_c lower. Some change in $\alpha_{tot,IV}$ was observed such that the transition seemed to become smoother and less steep. The measured noise shown in figure 6.6 does not have any obvious extra features and in general looks similar to a bare TES.

If we consider the layer structure of a CorTES and include the new knowledge about AlOx, we can construct an improved thermal block model for a CorTES. Figure 6.7 shows perhaps the simplest possible model. Very likely it would be more correct to describe the AlOx layer with a distributed model. However, even the "simple" model would be quite difficult to model properly. In any case, now we can begin to understand why the Corbino devices can sometimes be difficult to fit with the IH model, as discussed in next section.

Another thing that is explained by this finding is the effect on n. From CorTES

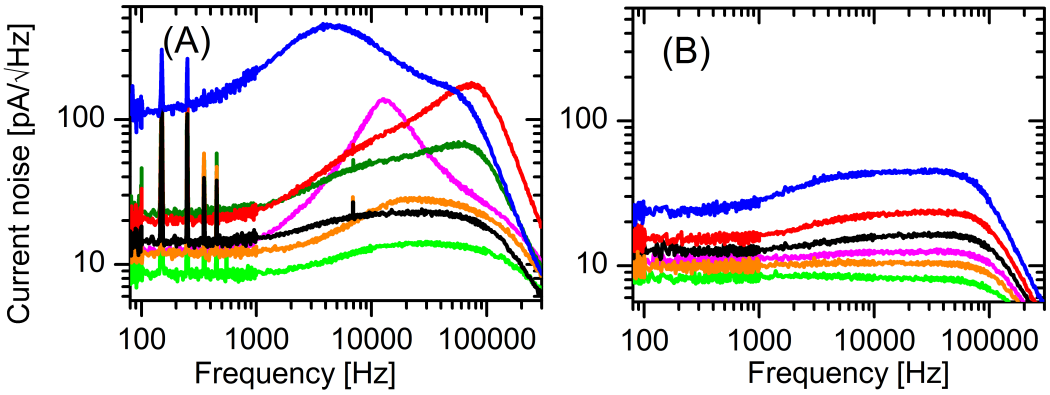

FIGURE 6.5 Measured electrical noise of a TES with (A) and without (B) AlOx layer. The bias points are indicated in Fig. 6.4(b). The curves with same colors correspond to roughly similar bias points. Noise levels increase when going lower in the R-T curve. Black curves are measured near 30 % bias.

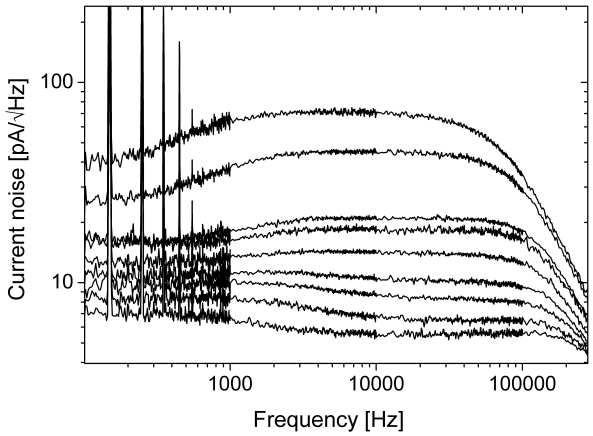

FIGURE 6.6 Measured noise spectra at 60 mK for the pixel with AlOx only on TES surface (figure 6.3a).

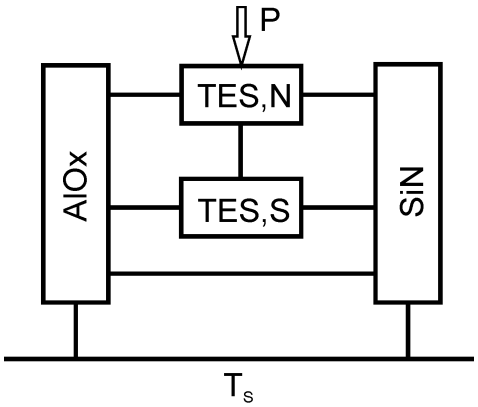

FIGURE 6.7 A possible thermal block model to describe the effect of an AlOx layer on a CorTES.

measurements we often get values that are typically below 3.5 whereas a device without AlOx on similar membrane often has values closer to 4. If the phononic heat transport in AlOx is diffusive (n = 3) and in SiN mostly ballistic (n = 4), their parallel combination will give n somewhere in between.

If we look at the data presented in article A.VII, we can also find evidence that AlOx has significant heat capacity. There we find C_{EX} values for the intermediate block of the IH model, which for a CorTES are clearly higher than a pixel without AlOx on a similar SiN membrane.

Finally, we note that some groups use TES designs where SiOx is used as an insulator inside the TES [95]. It could be that SiOx is a better insulator and problems are avoided but it might be worthwhile to actually do an experiment to check it. It would be simple to test by improving our accidental design to have a more controlled geometry and depositing SiOx on top of a bare TES on a membrane.

6.3 N-S decoupling as the source of ITFN

Here we review the results reported in article A.VII, where several different detectors were characterized and the IH model was used to fit the Z and noise data. Parameters for the studied detectors are given in table 6.1. We will try to find evidence on our suggestion that ITFN noise in a TES is caused by the normal and superconducting phases decoupling at high frequencies.

TABLE 6.1 Device parameters for the TESs presented in paper A.VII.

TES	Ti/Au [nm]	T_c [mK]	R_N [mΩ]	SiN [μm]
CorTES	40/55	98	200	0.30×800×750
STES	40/55	99	220	0.30×800×750
Slice 1	71/105	126	166	0.30×830×730
Slice 2	58/83	162	220	0.75×830×730
Square	48/70	156	425	0.75×460×410

6.3.1 OTES

We start by looking at CorTES data, measured from an OTES whose T_c was 98 mK and R_N = 200 $\mathrm{m}\Omega$. The TES is placed on a $0.3 \times 800 \times 750$ SiN membrane. After data was taken on the OTES, an absorber with 200 nm Au and 2 μm Bi was added on top of it, as shown schematically in figure 3.5(b) and the measurements were repeated. Unfortunately, the critical temperature was shifted down to 85 mK and transition steepness was reduced during absorber deposition so direct comparison is difficult.

Examples of OTES data are shown in figure 6.8. We only look at two bias points that adequately illustrate the difficult shapes of the impedance curves. Now that we know about the AlOx effect, we can identify frequency regions where both Z and noise do not fit well, and one could imagine that those features could be explained by the more complex thermal model discussed earlier (Fig. 6.7). Of course it is entirely possible that the absorber also adds an extra thermal body to the system, such as the one shown in figure 5.10. We emphasize that no M term was needed in fitting the OTES noise.

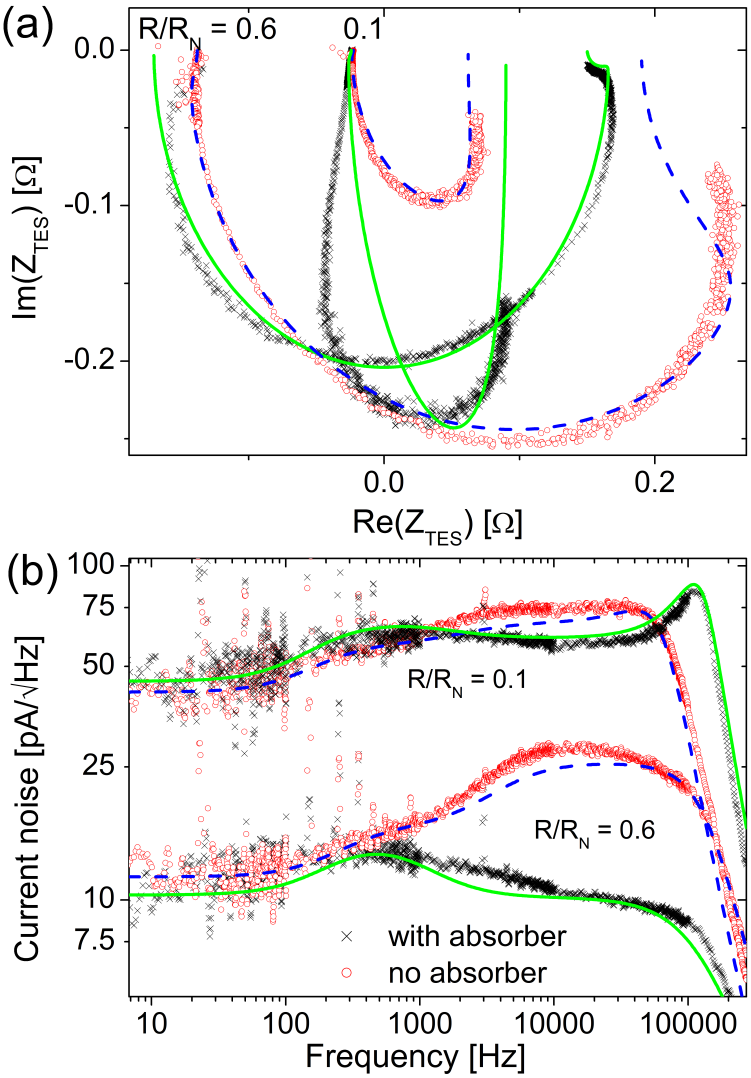

FIGURE 6.8 (a) Impedance and (b) noise data at two representative bias points from an OTES before (black crosses) and after (red circles) an absorber was deposited on it. The lines are best fits to the data using the IH model.

After seeing the data and the quality of the fits it probably comes as no surprise that there is some inevitable scatter in the obtained C values, shown in figure 6.9.

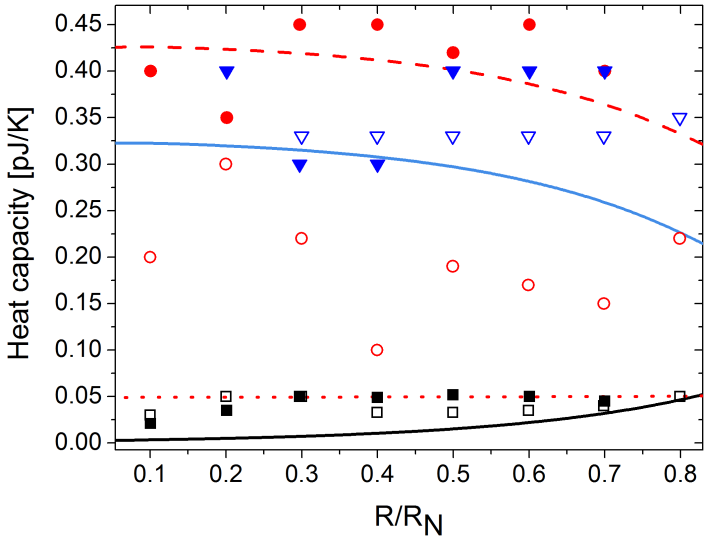

FIGURE 6.9 Heat capacity values obtained from the fits for OTES. Squares: C_{TES}, circles: C_{ABS} and triangles: C_{EX} Open symbols are before absorber and closed symbols with absorber. Solid black line is theoretical prediction for C_{TES} and solid blue line for C_{ABS}. Dotted red line is the calculated heat capacity of the Au layer in the absorber and dashed line is the sum of C_{ABS} and full absorber (Bi + Au). The temperature T_{EX} of the intermediate block varied between 90 mK and 88 mK.

There is, however, consistency to be found. C_{TES} is essentially unchanged but C_{ABS} has clearly increased after the addition of the absorber. The scatter in C_{EX} is largely due to the impedance data being dominated by the high frequency component. We should remember that the values shown here can include contributions from the AlOx layer but it is hard to say in which block it is most likely to have the most effect.

For the theoretical predictions we use our assumption that C_{TES} is the normal part of the TES and C_{ABS} is the superconducting region with heat capacity given by the BCS theory. While the fitted values do not fall exactly on the calculated ones, they at least show a clear division into a small C_{TES} coupled to a larger C_{ABS}.

Looking at figure 6.10 we realize why the noise level is lower with absorber at the 0.6 bias point – α is very small. The 0.1 bias is more interesting. Because $\alpha_{tot,IV}$ seems to be roughly equal, one could argue that the lower high frequency noise with absorber is explained by the lower TES temperature.

From the fitted thermal conductances we can make one interesting observation. Even though G_{dyn} decreased as expected for the lower T_c with the absorber, g_0 has actually increased. The increased conductance could imply an enhancement in electron-phonon coupling due to increased volume. A less impressive explanation would be the low conductance of Bi lumping it partly into the intermediate block. Nevertheless, this is something that could be investigated further.

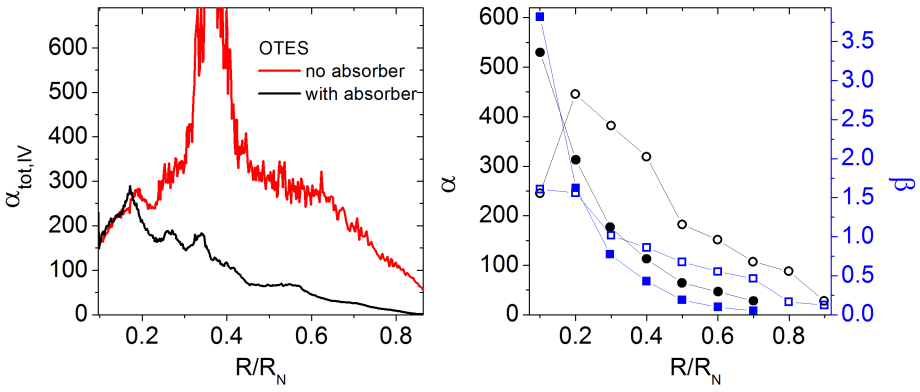

FIGURE 6.10 Left: total α calculated from IV. Right: α (circles) and β (squares) from Z data. Closed symbols are with absorber and open symbols without.

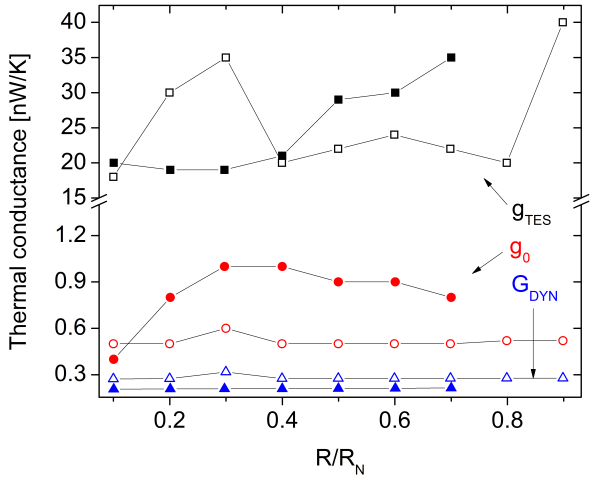

FIGURE 6.11 Fitted thermal conductances. Closed symbols are with absorber and open symbols without.

About g_{TES} we can comment that at least with the absorber, there seems to be a decreasing trend when approaching superconducting state. An estimate using Wiedemann-Franz law gives roughly 10 nW/K for the whole device in the normal state. If g_{TES} models only the superconducting phase, then the expected value is higher, which is consistent with the data.

In order to find possible dependencies of the high frequency noise on other parameters, we did a set of fits where all of the noise was accounted for by M. That is, set C_{ABS} to zero and use M as a way to quantify the level of excess noise. We plot the resulting M versus three different parameters in figure 6.12. With the absorber the α dependency seems weaker, and surprisingly linear behavior versus voltage is observed.

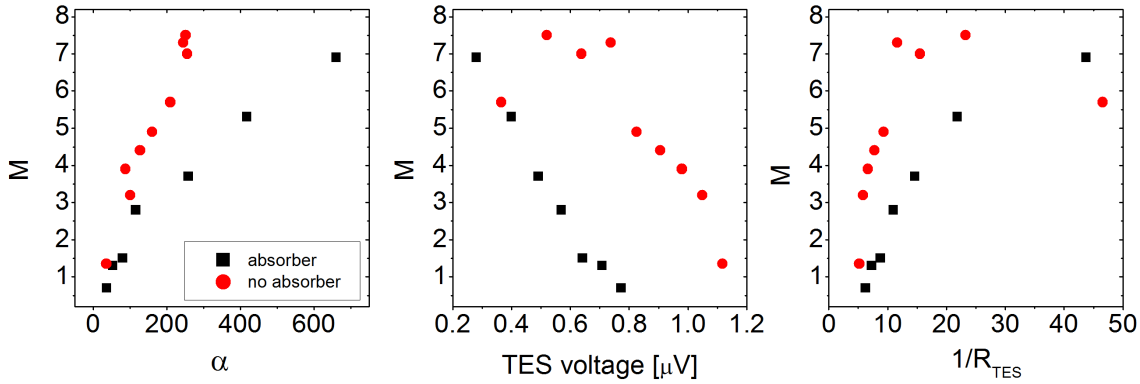

FIGURE 6.12 High frequency noise quantified by the M parameter.

6.3.2 STES

The STES under study was fabricated on the same chip and identical SiN membrane as the OTES discussed in previous section. It has T_c = 99 mK and R_N = 220 mΩ. A selection of the measured STES data together with the IH model fits is given in figure 6.13. In this TES, the impedance curves are less distorted probably thanks to a lower α (see Fig. 6.14). Both Z and noise data are quite well fitted by the IH model, except for some issue with the high frequency noise cut-off. The M parameter was not used in any of the fits for this pixel.

The fitted parameters are given in figure 6.15. We have again calculated the heat capacities based on the N-S phase separation idea. As with OTES, C_{TES} is lower than C_{ABS} but only approaches our predicted values in the lower part of the transition. The intermediate block has a large heat capacity, most likely because of the AlOx layer. It is possible that because the more realistic thermal circuit is so complicated (Fig. 6.7), using the IH model on the system gives us incorrect values for C_{TES}, for example. Notice that here we plot for the first time the reduced BCS heat capacity as predicted in [62]. Although C_{ABS} is mostly near that value, we do not want to jump into conclusions at this stage.

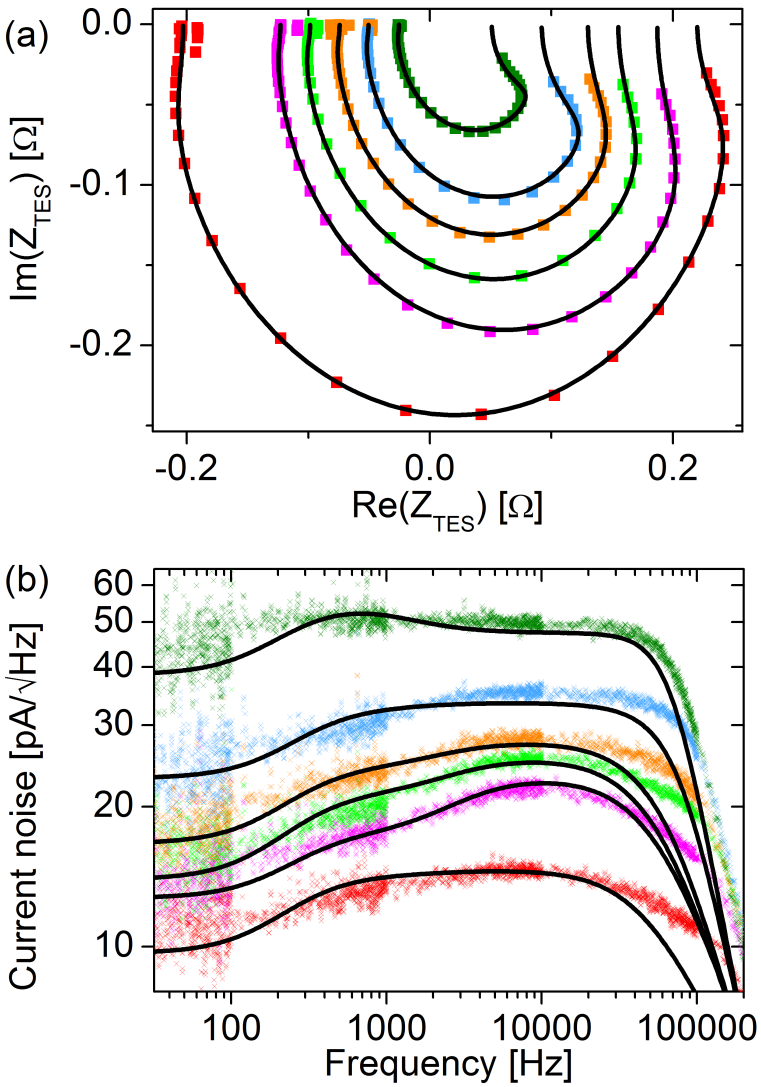

FIGURE 6.13 Measured (symbols) and fitted (lines) (a) impedance and (b) noise in an STES at bias points R/R_N = 0.8, 0.5, 0.4, 0.3, 0.2, 0.1, rest are omitted for clarity. The effect of decreasing bias is to move up in the noise curves and inwards in impedance.

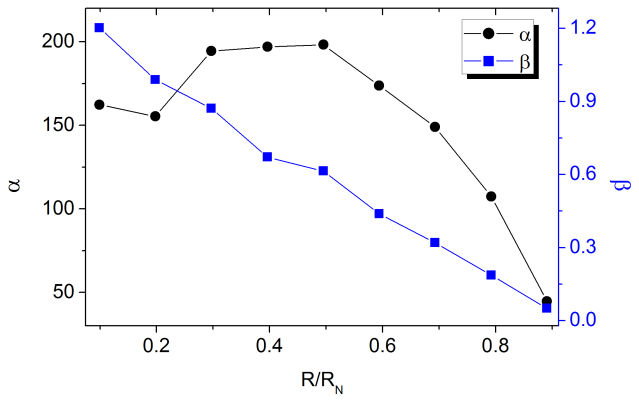

FIGURE 6.14 Parameters α and β for STES from impedance fits.

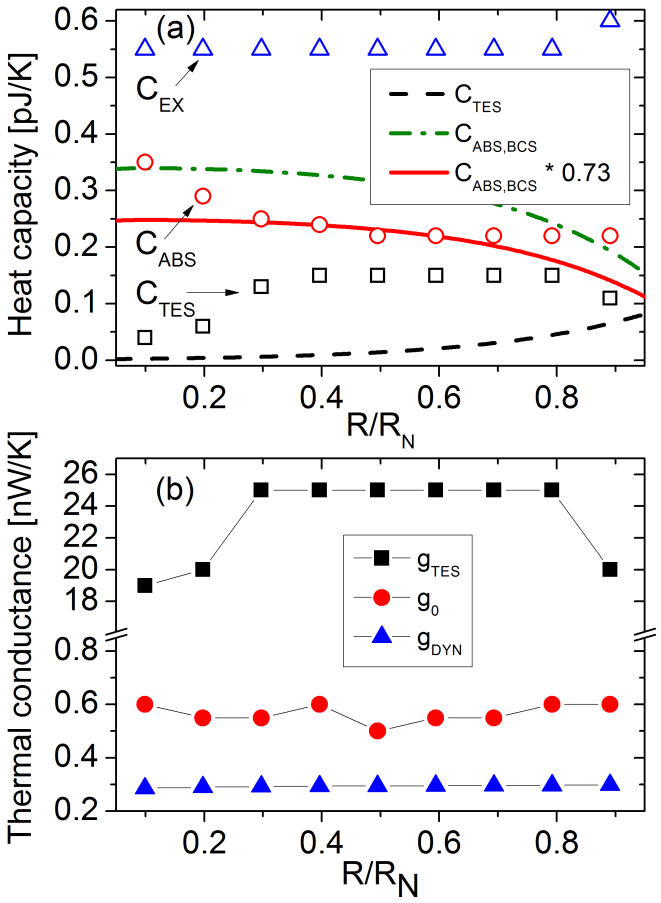

FIGURE 6.15 Fitted parameters for STES. (a) Heat capacity, symbols are measured data and lines theoretical calculations. Solid red line indicates a reduced value for the heat capacity jump in a Ti/Au bilayer. (b) Thermal conductances. The temperature T_{EX} of the intermediate block was 85 mK for all bias points.

6.3.3 CTES

As was evident in the previous section, we would like to remove the AlOx layer and the unknown effects it may have on our CorTES design, but hopefully still retain the possibility to calculate a prediction for the N and S phase heat capacity. This can be achieved with the CTES design. Here we present data for two such pixels with slightly different Ti/Au and SiN layer thicknesses.

CTES 1

The pixel that we shall refer to as CTES 1 has 71/105 nm Ti/Au layers with T_c = 126 mK and R_N = 166 mΩ. It is deposited on a similar SiN membrane as the previous CorTES pixels. This TES turned out to have rather unspectacular impedance features as shown in figure 6.16, likely due to a relatively low α throughout the transition. Because the Z data looks so basic, one might suspect that even a simpler thermal

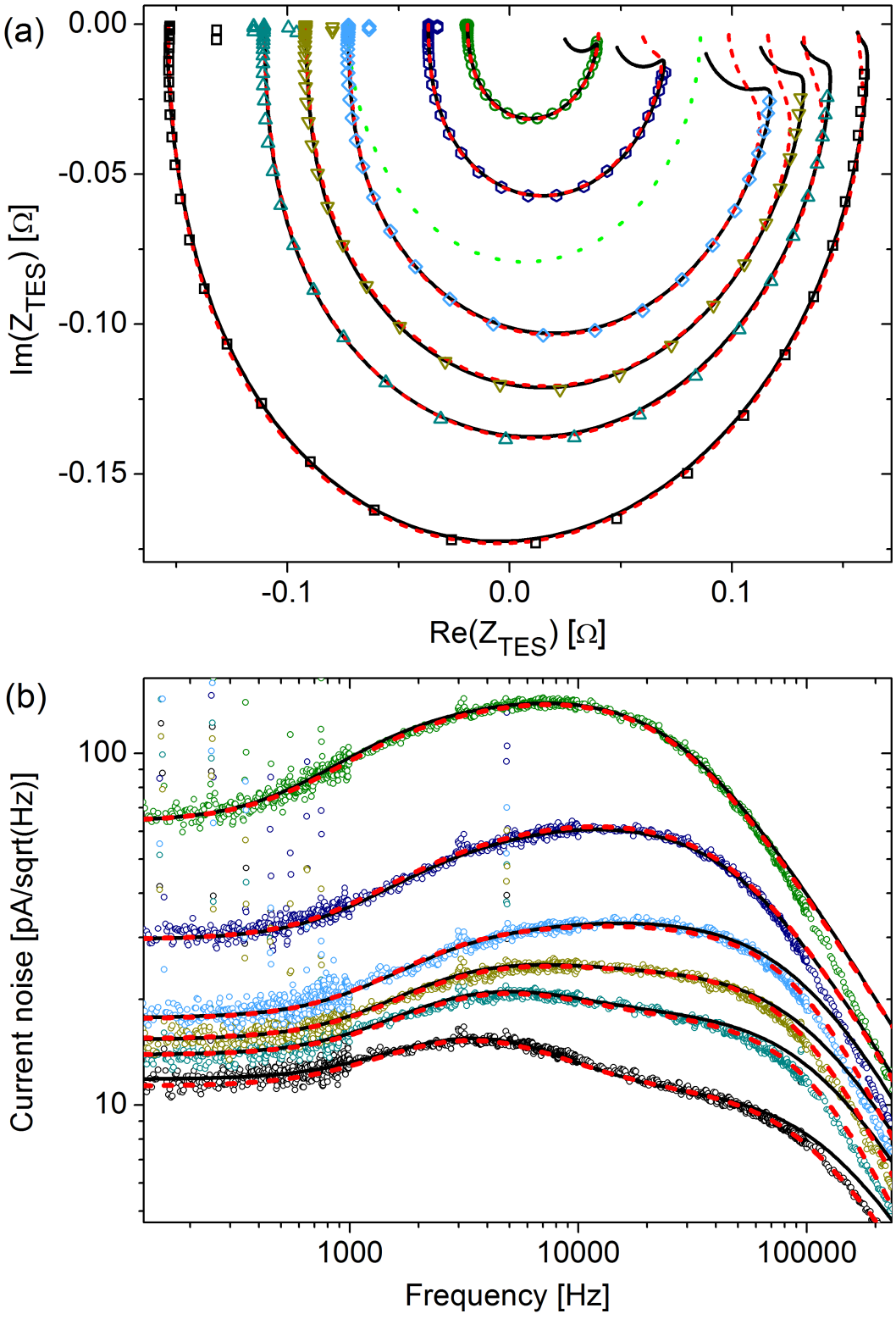

FIGURE 6.16 Comparison of fit cases 1 and 2 at R/R_N = 0.1, 0.2, 0.4, 0.5, 0.6, 0.8, rest omitted for clarity. Symbols: data, solid black line: case 1 fits and dashed red line: case 2 fits. The dotted green line gives the impedance according to a simple 1 block model to demonstrate how much case 1 deviates from it. The data is measured at a bath temperature of 60 mK.

model could fit the impedance and indeed it is the case. That does not mean we have to settle for an easy solution. Instead, we use this opportunity to make a point about the dangers of using any thermal model to fit data that *appears* to be simple.

What we shall do here is to look at three possible methods that all produce practically identical impedance fits. In fitting case 1 we force C_{TES} to the theoretically calculated values based on I-V data, again assuming the N-S decoupling. For case 2 we allow C_{TES} to be a free parameter also. In case 3 we use the M noise to fit all high frequency noise and set C_{ABS} to zero, making this a two-block model case of TES and intermediate block.

In figure 6.16 we compare cases 1 and 2. Both of them provide good fits to impedance and noise. Minor differences can be seen near the maximum measurement frequency where case 2 fits slightly worse on Z, but gives better noise roll-off match. Case 1 develops a sharp kink in Z just outside the measurement range.

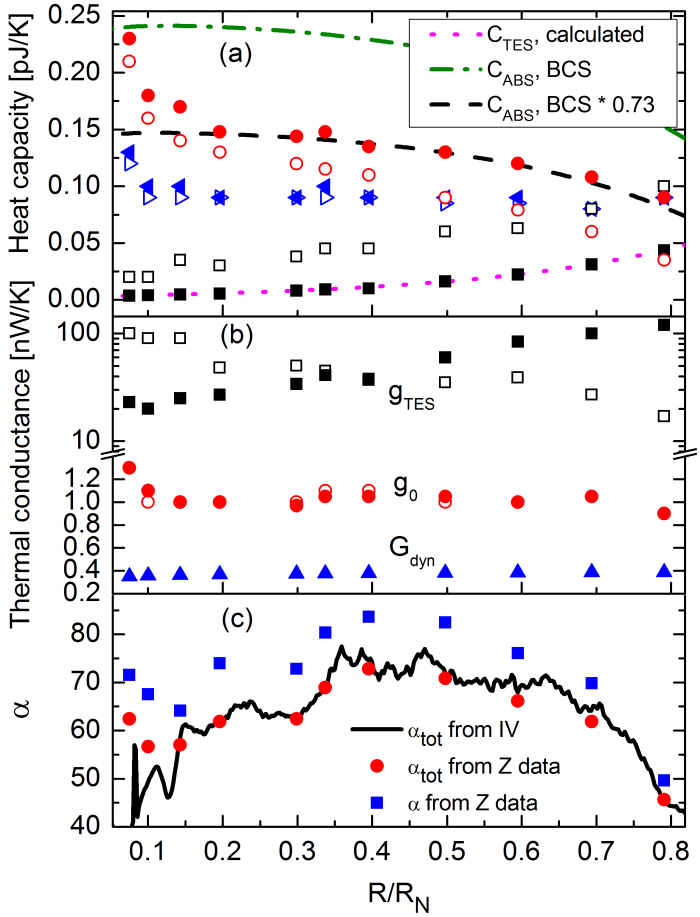

FIGURE 6.17 Parameters obtained from fits in Fig. 6.16. Filled symbols: case 1. Open symbols: case 2. Top: squares - C_{TES}, triangles - C_{EX} and circles - C_{ABS}. Lines are theoretical calculations. The temperature T_{EX} of the intermediate block was 129 mK for all bias points.

Looking at the obtained parameter values, presented in figure 6.17, we begin to see differences in the two fitting methods. Very interesting with case 1 is that as C_{TES} is forced to the theoretical value, C_{ABS} closely follows the reduced BSC value, except at the lowest bias points where it quickly increases for some reason. For case 2 the heat capacity values are somewhat different but follow the same general trend. As expected, without an AlOx layer C_{EX} has been greatly reduced in comparison to a full CorTES. Because we do not really understand how the thermal conductance g_{TES} is supposed to behave, it is difficult to make any strong statements. It would be tempting to claim that for case 1 we are seeing the conductance decrease when going down in transition because of the changing contact area between N and S phases which should be seen as a linear trend on a log scale. It is harder to find justification for the opposite behaviour of g_{TES} in case 2.

In contrast to the earlier CorTES fits, here we needed to include M in order to fit the noise data low in the transition. In case 1, M was needed below 30 % bias and for case 2 below 50 %. This pixel had a curious anomaly in the noise in a narrow bias range, where a large mid-frequency peak appeared. This happened at the 34 and 30 % points and coincides with a sudden drop in α. The extra noise peak is presented in figure 6.18 where it is also shown that the peak cannot be explained by M noise. Many variations of parameters were tried but it appears to be impossible to have the intermediate block generate such a noise in the IH model. The only explanation we have come up with so far are vortex-related effects. Varying the external magnetic field should be tried in future experiments to see if vortices are indeed involved. Another possible explanation might come from using a more complex thermal model where a link between C_{ABS} and C_{EX} is taken into account but we have not done any calculations using such model yet.

To confuse the situation further, we have sometimes observed a similar noise peak in a full CorTES. In one particular case, shown in Fig. 6.19, the extra noise feature was first seen, but then after an overnight standby of the cryostat, it had disappeared and was not found again at any bias settings. We do not have a solid explanation for this phenomenon.

For the fitting case 3 we settle on showing representative plots at two bias points because the message should become clear with those – the other bias points do not look any different. Figure 6.20 shows a comparison between case 3 and case 1 impedance fits, the noise fits look very similar to case 1. As expected, case 3 gives good impedance fits also and in the experiments frequency range we would not be able to tell the models apart from each other.

As we have shown, the same data was successfully fitted using models that produce noticeable variation in obtained TES parameters and would lead to very

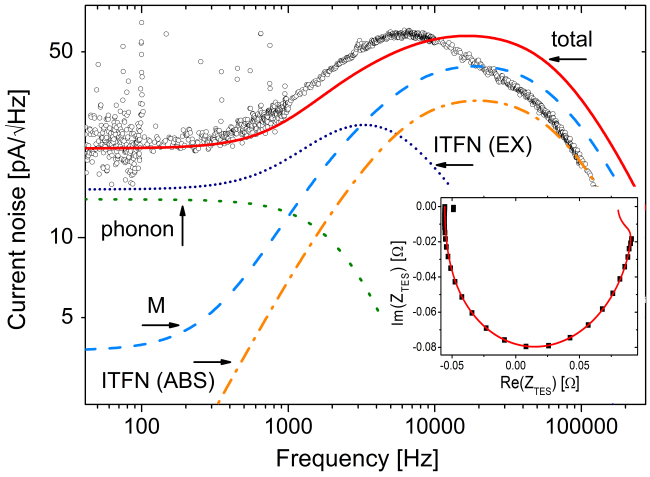

FIGURE 6.18 Anomalous mid-frequency noise peak was observed in a narrow bias range. The M noise is included in the noise calculation to demonstrate that it fails to explain the noise. Inset: the related Z curve does not show any strange features and can be fitted well.

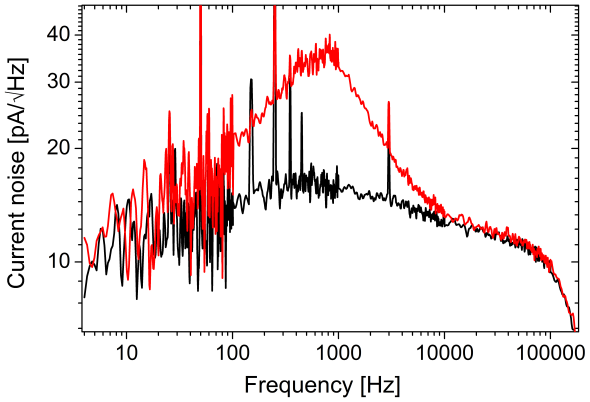

FIGURE 6.19 An excess mid-frequency noise bump measured in an OTES (red line). The feature was not seen on the next day (black line, same bias setting and bath temperature).

different ideas about the underlying TES model and physics. For example, in some cases β may be an important design parameter and if a wrong model is used, the obtained values could be surprisingly far from the correct one, assuming there is no alternative method available to extract accurate values for β.

Figure 6.21 compares parameters between all three cases. Perhaps the most interesting result is the good agreement of the total heat capacity (excluding C_{EX}) between the cases. The fact that case 3 follows the others tells us that the rapid increase low in the transition is probably real and not due to bad parameter choices in an attempt to avoid having to resort to M noise. Notice also how varied the β values are. We actually also did a fourth alternative fit where C_{TES} was held constant at 0.1 pJ/K, but we do not show the results here because the obtained fits look practically

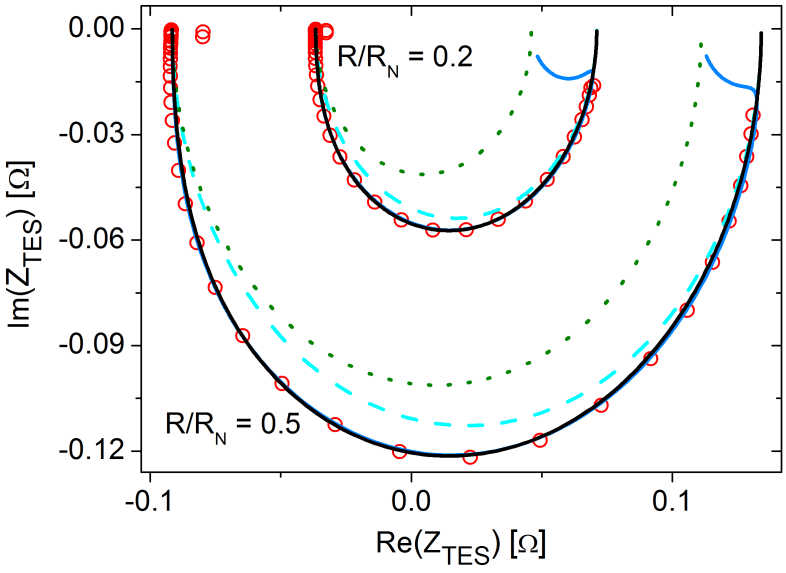

FIGURE 6.20 Fitting cases 3 (black line) and 1 (blue line) compared. The dashed and dotted lines are the corresponding Z curves for a simple thermal model.

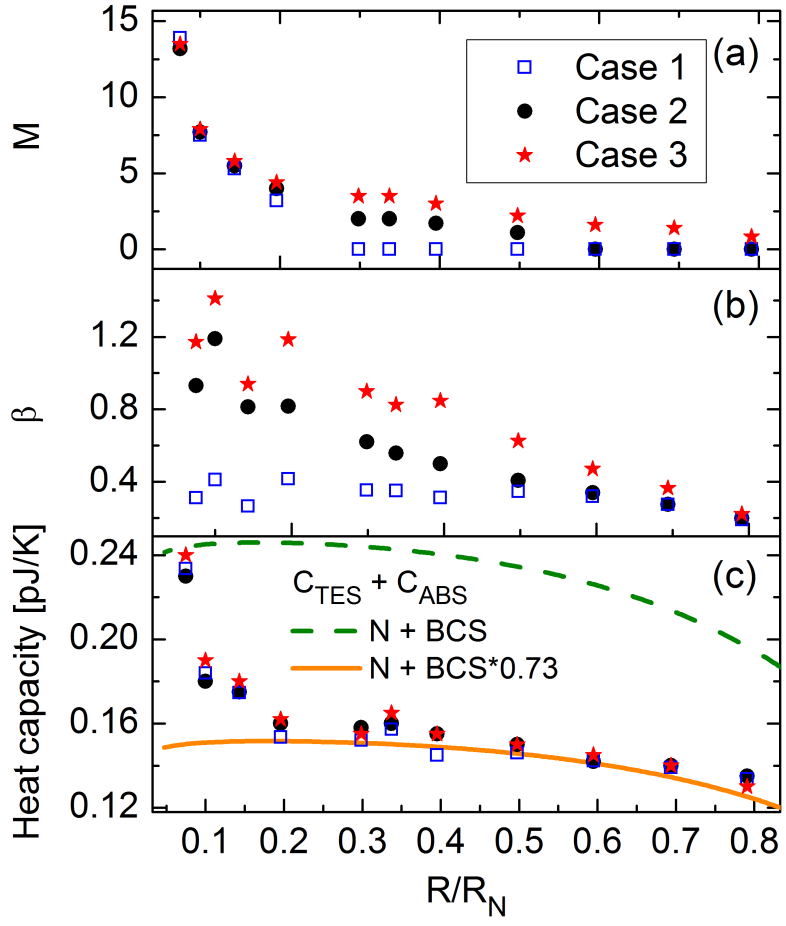

FIGURE 6.21 Comparison of parameters between different fit cases for CTES 1. Symbols: fitted values. Line: calculated total C. In case 3 $C_{ABS} = 0$ and total C comes from C_{TES} alone.

identical and again the total C was the same as the other cases.

To see if any trends in the noise could be observed using M from case 3, we refer to the selected plots in figure 6.22. These graphs again show how something strange happens near the 34 % bias but before that roughly linear trends can be seen.

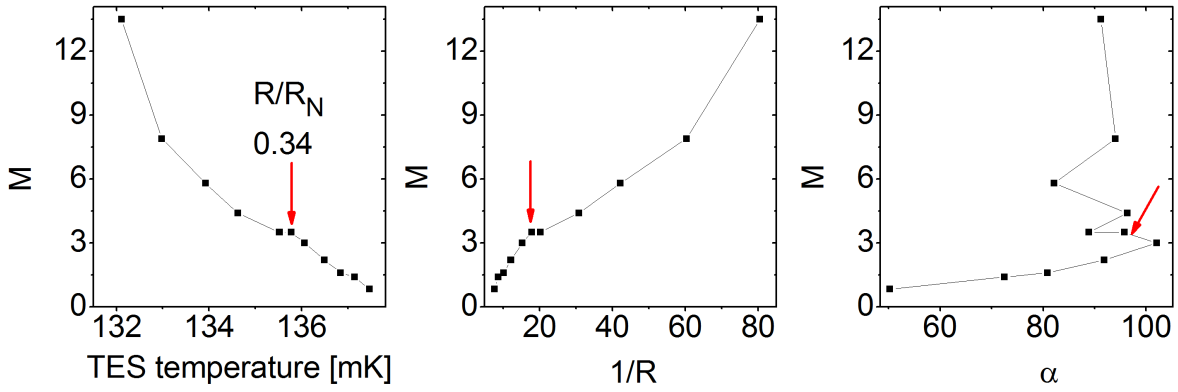

FIGURE 6.22 M noise from case 3 fits for CTES 1. Arrow indicates the R/R_N = 0.34 bias point.

CTES 2

The second slice TES will be referred to as CTES 2. It has 58/83 nm thick Ti/Au layers which produces a T_c of 162 mK and the TES sits on a $0.75 \times 830 \times 730$ μm SiN membrane. In contrast to CTES 1, CTES 2 featured a more complicated transition with very large peaks in $\alpha_{tot,IV}$ as shown in the inset of Fig. 6.23. The high values of α produces complicated impedance features and high noise levels. CTES 2 was measured at four different bath temperatures: 140 mK, 110 mK, 85 mK and 60 mK. Fig. 6.23 shows the data measured at a bath temperature of 140 mK.

Looking at the complex shapes of the Z data, we argue that fitting case 3 from previous section is out of the question. Because there is no reason to expect two identical geometries to have different thermal circuits, it is our conclusion that case 3 is not the correct fit method for CTES 1 either. For CTES 2 data we allowed all fit parameters to be free (i.e. case 2).

Again, the main features of both Z and noise data are captured with the IH model. However, at bias points where α is very large it was more difficult to find good fits, and determination of Z_∞ is more uncertain. The inevitable result of this is more scatter in the fitted parameters. In Fig. 6.24 all the results from all four bath temperature runs are plotted in one graph, as C_{TES}, C_{ABS} and g_{TES} should not depend on T_{bath} at all according to the thermal model (C_{EX} is affected by T_{bath}, thus we show only 60 mK values of C_{EX} to match CTES 1 data). Comparing to CTES 1, we

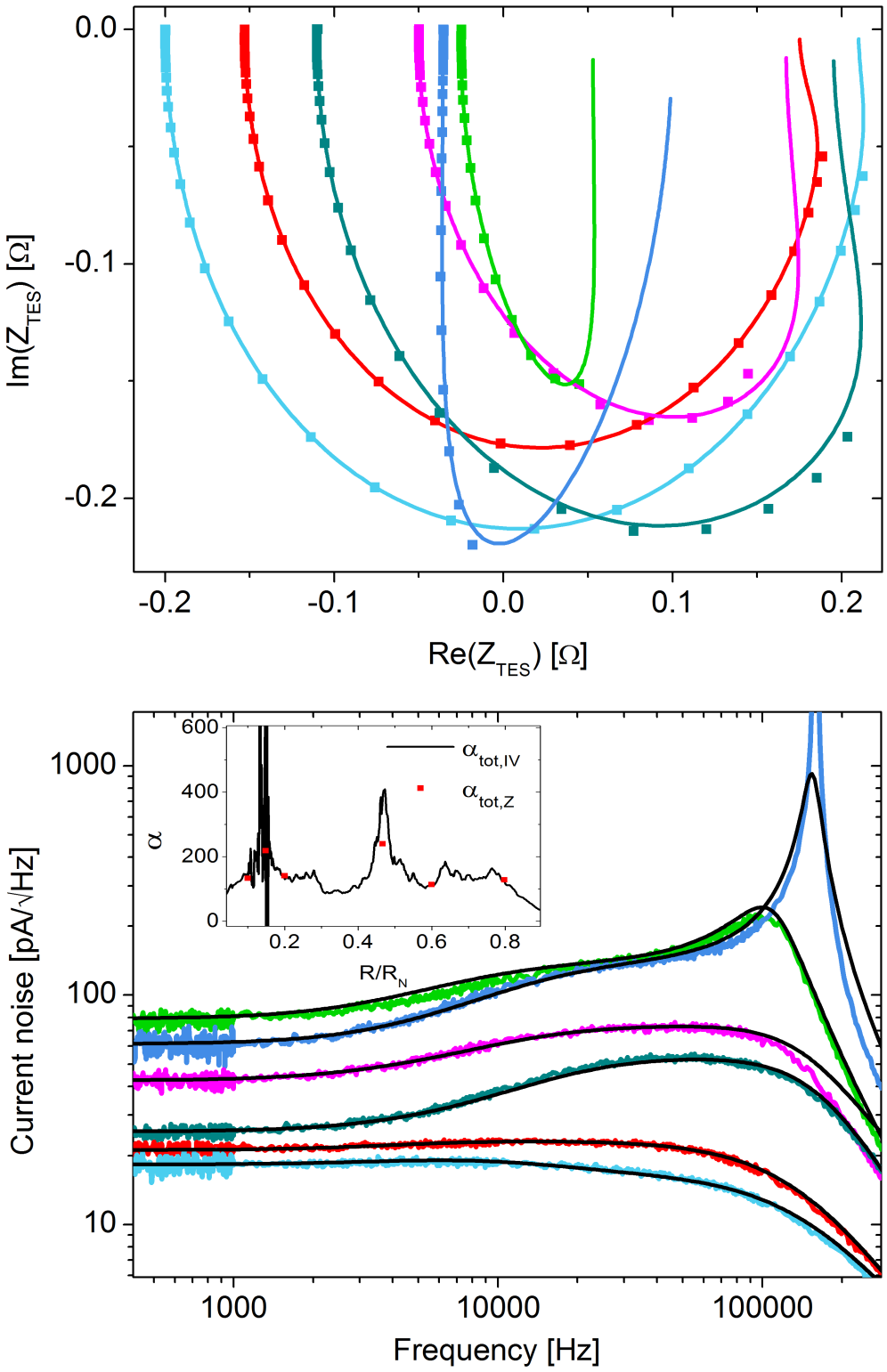

FIGURE 6.23 Measured impedance and noise data and fits using IH model (lines) for CTES 2 at 140 mK. Data is measured at R/R_N = 0.8, 0.6, 0.47, 0.2, 0.15 and 0.1. In impedance the highest bias point corresponds to the outer Z curve and in noise it is the lowest lying curve. In the noise plot black lines are the fits. Inset: total α calculated from I-V and Z data.

see that C_{TES} and C_{ABS} have the same trends, and roughly same values; the increase of T_c is partly compensated by thinner films. On the other hand, C_{EX} is three times larger. This again supports the picture that C_{EX} originates from the SiN membrane, as it is 2.5 times thicker for CTES 2. g_{TES} is of the same order of magnitude, and does not follow a monotonous trend throughout the whole transition. Most of the noise data for CTES 2 did not require any additional M-noise, at 140 mK shown here it was only needed at 20 % bias, and it immediately shows as a bad fit to the roll-off of the noise at high frequency compared to other measured bias points.

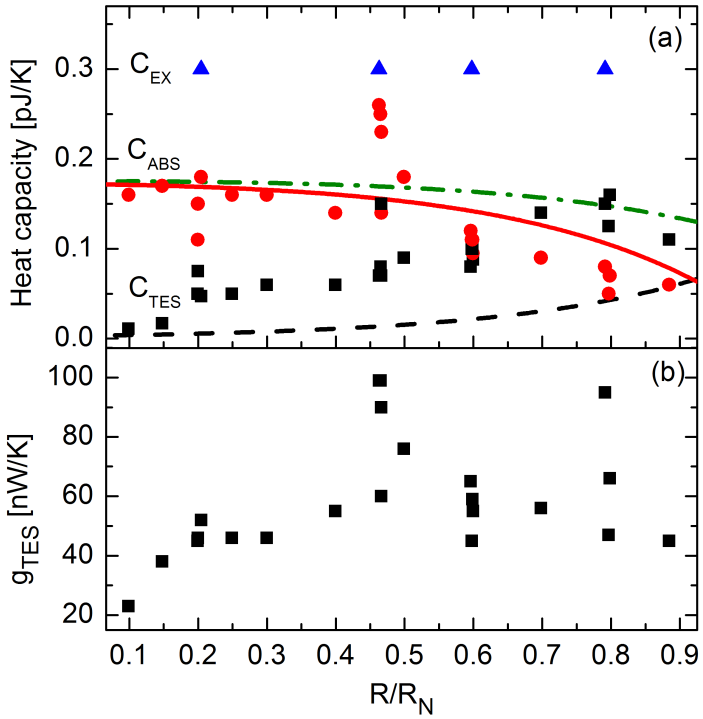

FIGURE 6.24 Obtained fit parameter values for CTES 2 at four different bath temperatures, except C_{EX} for which only 60 mK data is shown. The lines show theoretical heat capacity for C_{TES} (black dashed line) and reduced BCS value for C_{ABS} (solid red line). Green dash-dotted line is their sum. Data for thermal conductance g_0 is not shown because it depends on bath temperature. For comparison with CTES 1, at 60 mK and 50 % bias CTES 2 had g_0 1.1 nW/K and G_{dyn} = 0.97 nW/K. The temperature T_{EX} of the intermediate block was 147, 145 and 130 mK at 140, 110 and 60 mK bath temperature, respectively.

If we look closely at what happens with C_{TES} and C_{ABS}, we notice that higher in the transition the value of C_{TES} is closer to the total N+S heat capacity while C_{ABS} starts smaller than predicted, and then reaches the reduced BCS value near the bottom of the transition. We speculate that this might suggest that initially both N and S phases are sufficiently well coupled to act as one entity. If the volume of S phase that is "near" the N phase should rather be included in the heat capacity C_{TES}, it

could explain why the fitted values for C_{TES} only reach the predicted values very low in the transition. An alternative explanation could be that in the slice TES the transition does not develop as we expect. Instead of a purely radial phase boundary, superconductivity could perhaps proceed along one of the edges slightly faster than the other, due to inhomogeneity caused by the self-field of the bias current, for example. To spare the reader from further wild speculation we conclude that the theoretical understanding of the situation is not sufficient at the moment.

6.3.4 Square TES

To conclude the review of article A.VII, we present data from a basic, bare square TES (TTES). The TES has 48/70 nm Ti/Au thickness with T_c = 156 mK, R_N = 425 $\mathrm{m}\Omega$ and sits on a $0.75 \times 460 \times 410$ μm SiN window. In Fig. 6.25 we plot the measured and fitted impedance and noise data. Again, the shapes of the impedance curves shows that the model without a hanging block (case 3 with CTES 1) will not work here either. The IH model produces good fits for both Z and noise, which gives us confidence that the noise in the square TES can be explained by the same mechanism as in the other geometries. Note that no M parameter was needed in these fits.

Figures 6.26 and 6.27 show the relevant parameters from the fits. The heat capacity data is consistent with our model of thermal decoupling of the N and S regions. To calculate some estimate for the N and S phase heat capacities, we use a crude model of a linear transition, where the ratio of the volumes is given directly by R/R_N, so for example in the middle of the transition we would have exactly half of the device in the superconducting state. This model produces a correct order of magnitude for C_{TES} and C_{ABS}, but naturally no real agreement, although the parameter values do seem to change linearly with R, as our overly simple model predicts. The values of thermal conductances are also consistent with the Corbino devices, and g_{TES} does not show any simple dependence on R.

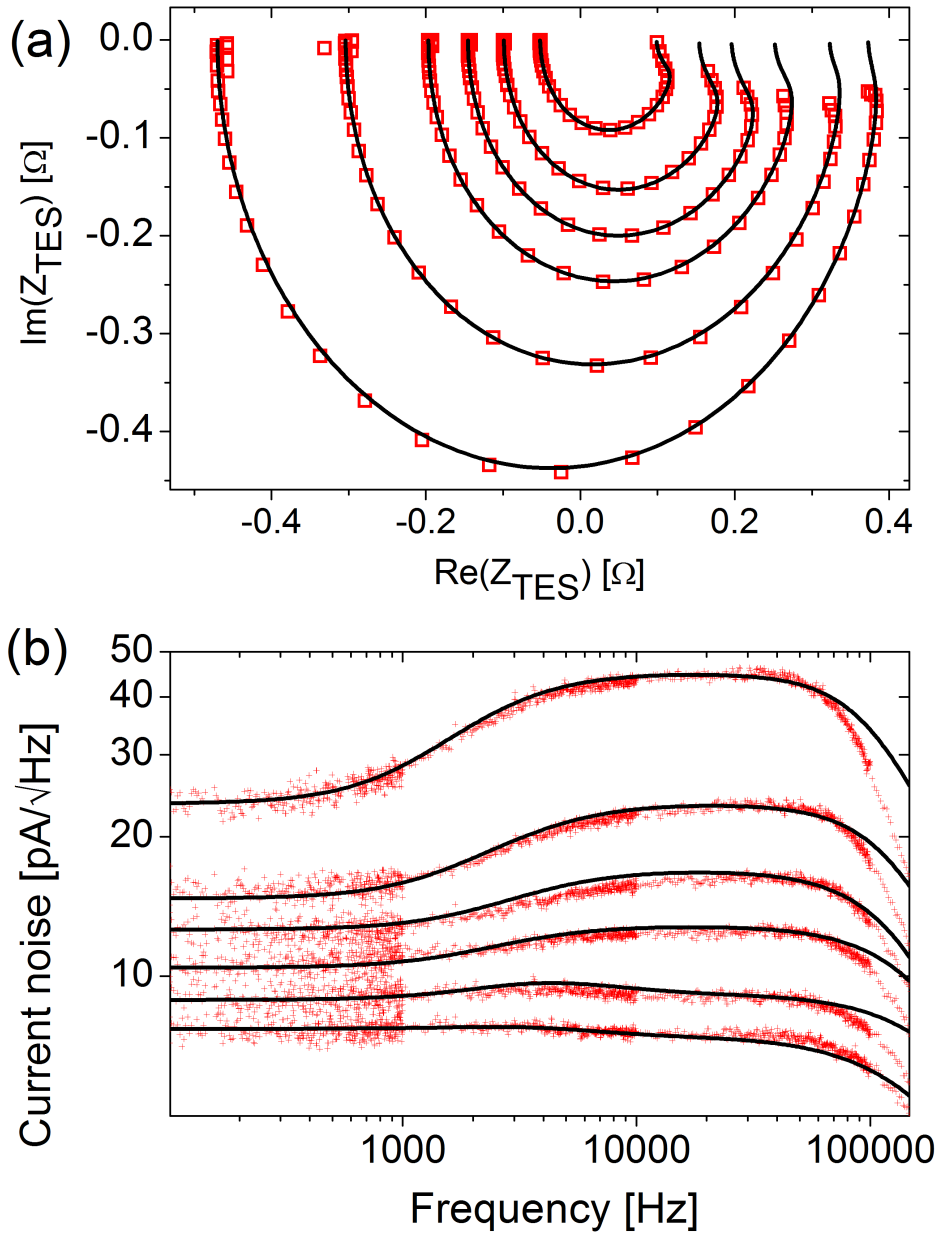

FIGURE 6.25 Measured square TES data (symbols) and IH model fits (lines). The bias points are R/R_N = 0.8, 0.6, 0.4, 0.3, 0.2, 0.1.

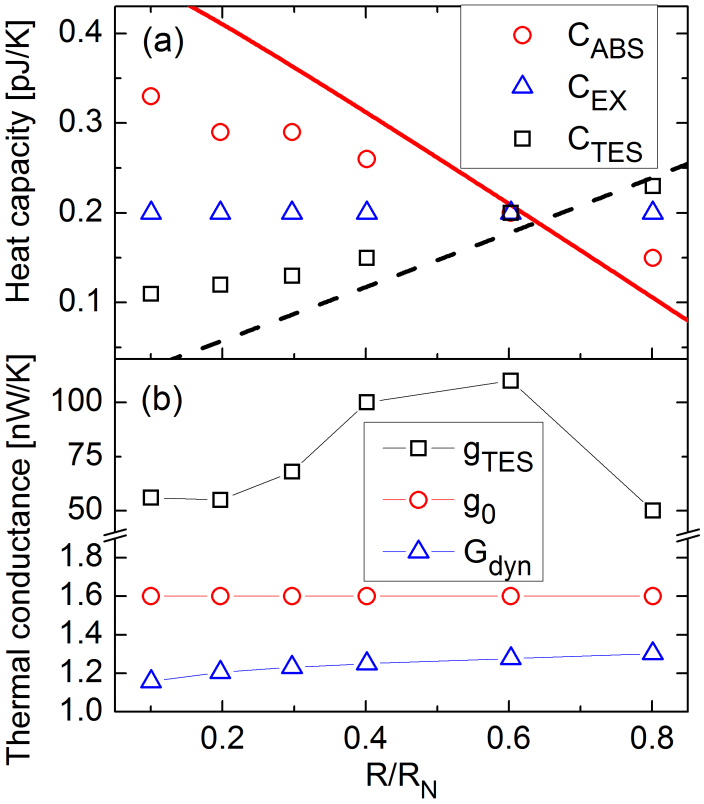

FIGURE 6.26 Parameters from the fits in Fig. 6.25. Lines show simple linear estimates for C_{TES} (dashed) and C_{ABS} (solid). The temperature T_{EX} of the intermediate block was 130 mK for all bias points.

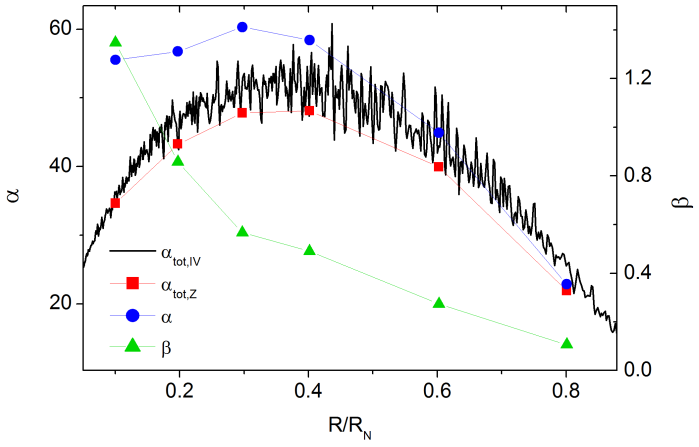

FIGURE 6.27 α and β parameters for the square TES.

6.4 Other TES data

Now that the main results of this work have been presented, we also review various older measurements on slightly different square TES geometries.

6.4.1 Square TES with dot-coupled absorber

The results discussed in this section were published in article A.III. The TES in question, labeled TTES16/06, was our basic 300 μm square with a T_c of 131 mK and was on a 0.7×700×700 SiN membrane. A Cu + Bi absorber was deposited on the TES as shown in Fig.6.28.

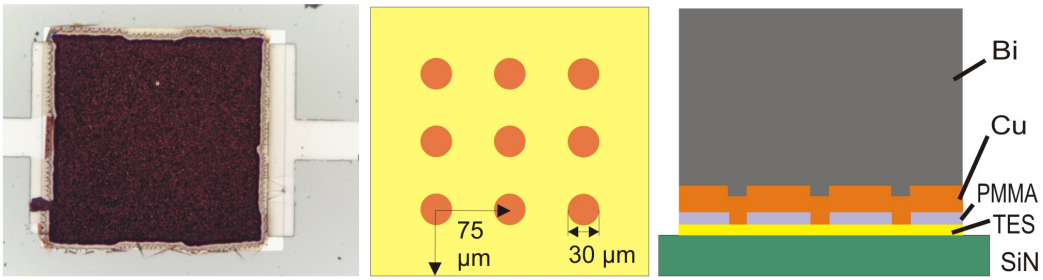

FIGURE 6.28 Left: optical microscope image of the TES with 300 nm Cu + 3 μm Bi absorber coupled to the TES via 9 Cu pillars. The e-beam resist used to pattern the pillars was hardened during absorber deposition and was not removed in acetone. Middle, right: schematic view of the design.

The problem with the absorber coupling is that it allows an alternative low resistance path for TES current parallel to the TES, which may lead to unpredictable current distribution inside the device. The uneven current density promotes a separation into N and S phases or into normal regions with different temperatures, causing ITFN noise to appear. This TES had specific points in the transition where $\alpha_{tot,IV}$ was very large and the noise at those bias points was extremely high. So high in fact that it prompted the invention of a new imaginary noise term – Infernal Fluctuation Noise, IFN.

At this point we had not started doing impedance measurements so all the information was gathered from I-V curve and experimenting with different fits to the measured noise. For this case, we used the equations for ITFN noise given by Refs. [96, 97]. A sample of the measured noise together with fits is shown in figure 6.29. It is obvious that this TES needed a mid-frequency ITFN term, likely originating from the SiN membrane as observed in other detectors. A large part of the high frequency noise was quantified by the M noise term, but as we have learned from the later experiments, this could probably be explained by ITFN also. With-

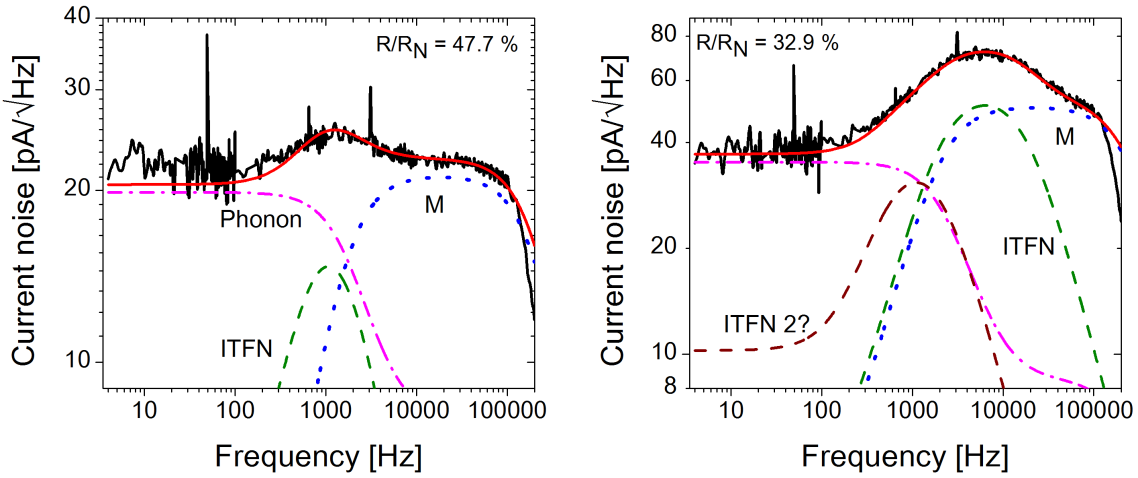

FIGURE 6.29 Noise spectra at two different bias points from TTES16/06. The different noise components are indicated in the figures and solid red line is the total calculated noise.

out Z data we cannot be sure, though. The need for a second ITFN term shown in the 32.9 % bias point data was justified by the slope on the rising edge of the large peak which we were unable to fit with just one ITFN component. It is unclear if the M noise term is truly needed in addition to the two ITFN terms, because the kink near the high frequency roll-off could have been caused by improper settings of the readout electronics.

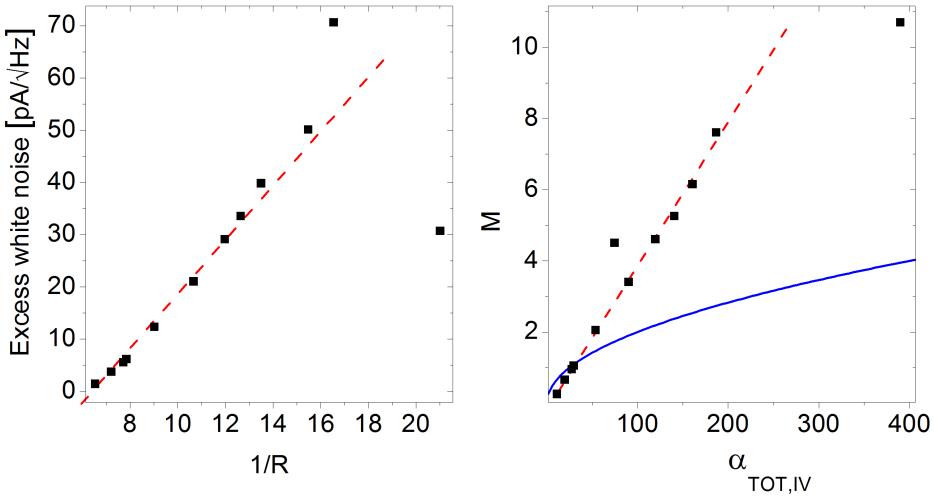

FIGURE 6.30 (A): Maximum value of the excess noise at 15 kHz versus the inverse of TES resistance. (B): M versus $\alpha_{tot,IV}$. Solid line is the $M = 0.2\sqrt{\alpha}$ result from Ref. [34].

Figure 6.30(a) shows the observed excess noise level versus inverse of resistance and except for the lowest biast points where $\alpha_{tot,IV}$ was low it is linear. In figure 6.30(b) the M parameter is plotted against $\alpha_{tot,IV}$.

6.4.2 Square TES with dot-coupled absorber by SRON

During this thesis work a substantial amount of time was spent characterizing two pixels fabricated by SRON, within an ESA project (XEUS) collaboration. They also had dot coupled absorbers like our TTES16/06 described in previous section. The difference was that now the absorber made contact to the TES only in a central line perpendicular to the current, so the current cannot choose a path through the absorber. In addition to the Cu pillars for coupling to the absorber, the TES surfaces were patterned with extra Cu dots to tune transition properties, as illustrated in Fig. 6.31. The difference between the pixels was the amount of the extra Cu dots. In the one labeled pixel 11 there were 6×5 dots with 10 μm diameter and the other, labeled pixel 13 (they were part of a larger array), had 10×7 dots. Data on other similar pixels is given in Ref. [95].

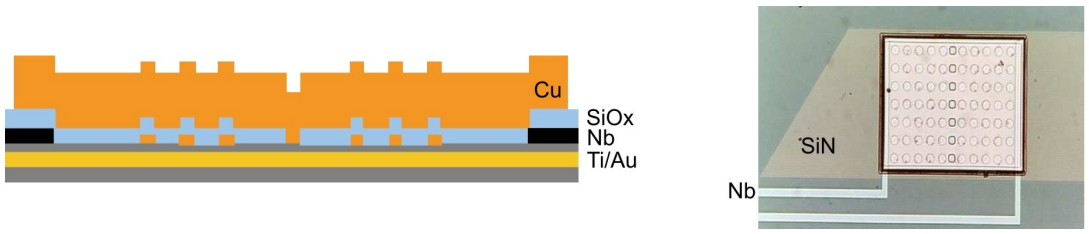

FIGURE 6.31 Left: schematic side view of the SRON TES. Right: optical microscope image of pixel 13. The size of the TES is 186×150 μm^2 and the absorber is 206×162×1 μm^3.

The rather massive absorber ($C_{ABS} \approx 0.4$ pJ/K at $T_c \approx 125$ mK) can be expected to add ITFN noise, especially considering the limited thermal contact area it has with the TES. Another source of ITFN could come from within the TES film itself, due to inhomogeneities created by the Cu dots. The uneven current distribution caused by the normal metal features would either create a phase separation to N and S areas inside the TES or just N regions with different heat capacity, α and current density, as discussed in Ref. [97]. A thermal block model of the system could be close to the one shown in Fig. 5.10.

Initially, a two block thermal model was used in fitting to Z and noise data. Both pixels had quite complicated impedance features, and especially Pixel 11 had higher values of α, making fits very difficult. It became obvious that the two block model was not sufficient to fully explain the measured data. The efforts with the two block model can be condensed into figure 6.32. If we choose to distrust or simply ignore the high frequency data we emulate the results of Ref. [79] where Z was measured up to 30 kHz.

We present one more plot from the two-block model fits using M in Fig. 6.33. The interesting observation here is the clear difference between the two pixels. Be-

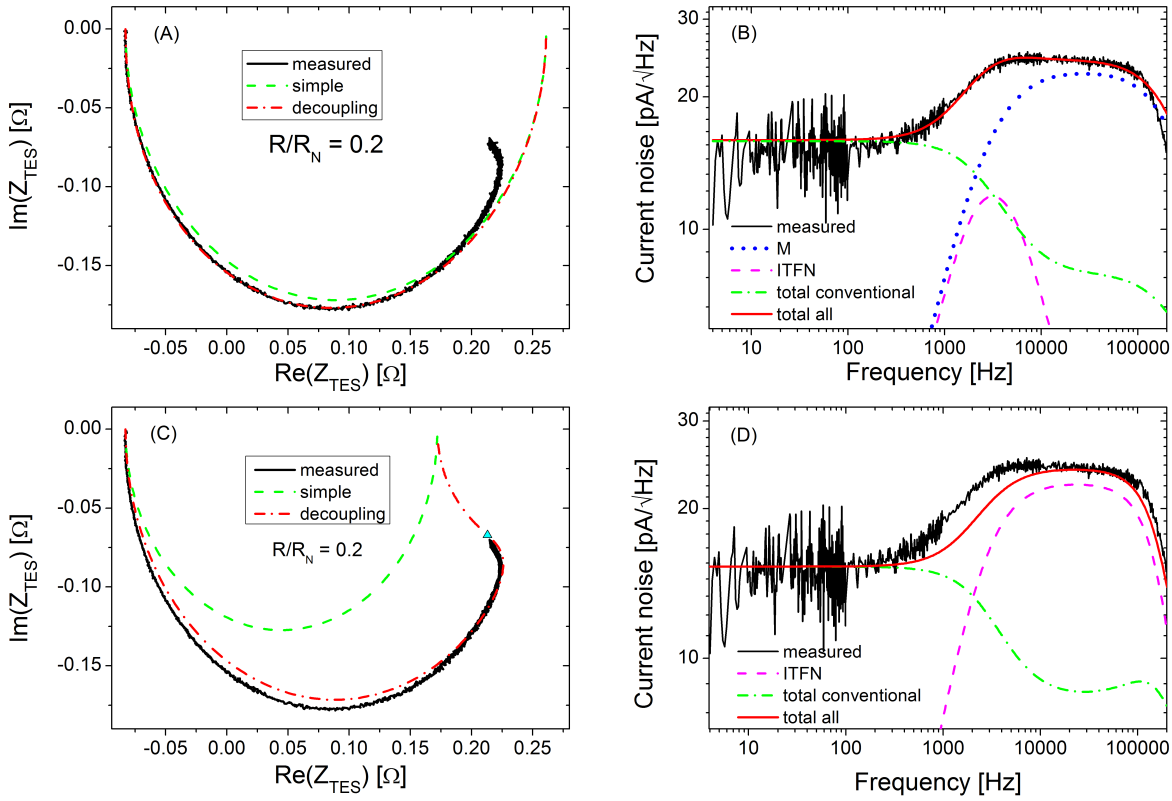

FIGURE 6.32 An example of two different ways to fit pixel 13 data with two-block models. Top: ignore high frequency Z data and explain noise by M. Bottom: ITFN from the absorber causes high frequency features and intermediate frequency fit is poor.

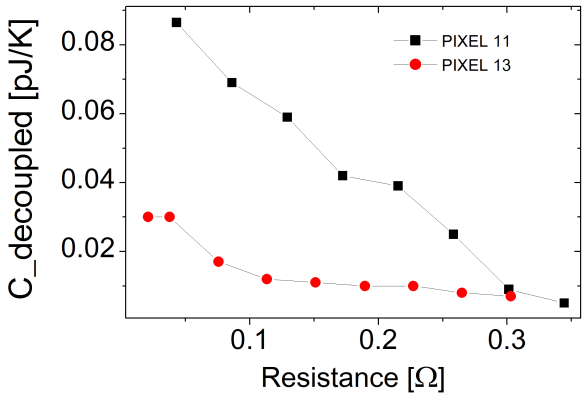

FIGURE 6.33 Fitted values for decoupled heat capacity when M is used to explain high frequency noise. $C_{decoupled} = C_{ABS}$ and it is responsible for the mid frequency noise in Fig. 6.32(b).

cause pixel 11 has less TES area covered by the Cu dots, it can have more volume in the superconducting phase than pixel 13. Thus N-S decoupling could explain this result. Even though the noise bump is in the mid-frequency range that we have later designated to an intermediate block due to the SiN membrane, it was one of the original motivations for us to pursue the idea of N-S decoupling.

In article A.V we have used our three-block models on pixel 13 data to show that it is indeed rather well explained by the IH model. The improved quality of fits compared to a two-block model is shown in Fig 6.34. We also did the fits using the 2H model. The resulting fits are equal in quality, only the values of the fitted parameters change slightly between the models as shown in figure 6.35. The theoretical estimate for C_{TES} includes both N and (reduced BCS) S heat capacity and C_{ABS} is the calculated Cu absorber value. The large C_{ABS} dominates and we cannot say if N-S decoupling is also present.

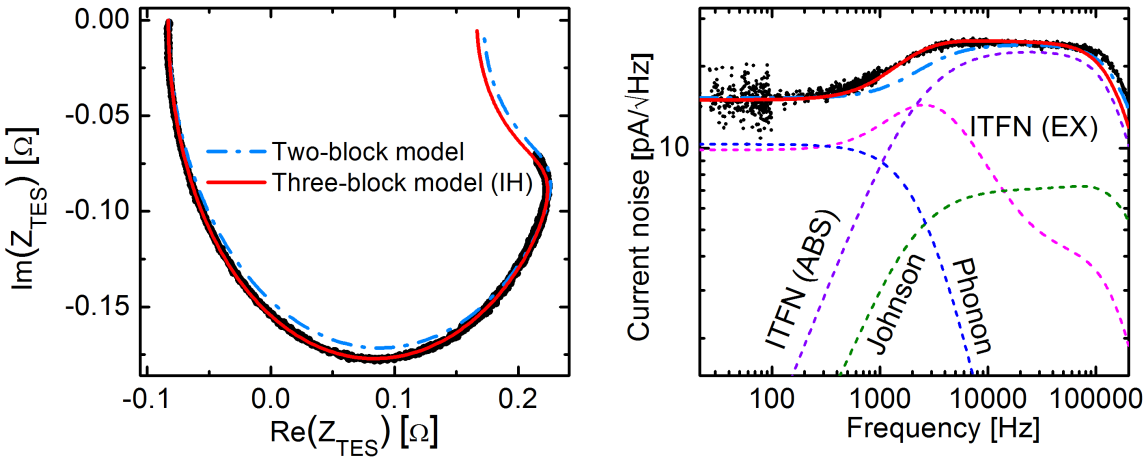

FIGURE 6.34 Comparison of two and three-block model fit results for pixel 13 at 20 % bias. All the measured features are well explained by the IH model. Right: dotted lines are the noise terms from IH model and the solid and dash-dotted lines are the total noise from IH and two-block model, respectively.

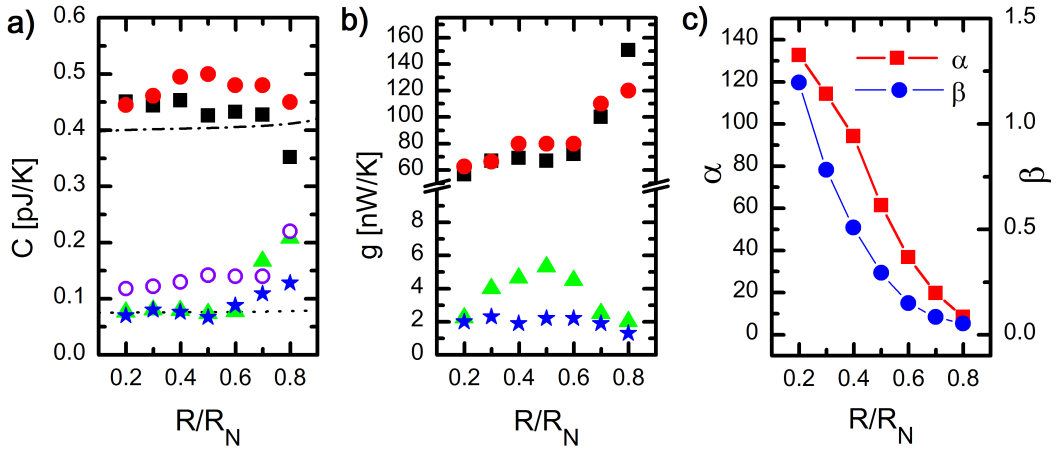

FIGURE 6.35 Some of the parameters from both IH and 2H models vs. bias point. a) C_{TES} (IH triangles, 2H stars), C_{ABS} (IH squares, 2H circles) and C_{EX} (IH open circles) and the estimated theoretical values as dashed lines. b) g_{TES} (IH squares, 2H circles), g_0 (IH triangles) and g_{EE} (2H stars). c) α and β.

6.4.3 KTES

One TES design we have fabricated that was not mentioned in chapter 3 was a rather strange one, called KTES. The design is presented in Fig. 6.36. It did not quite behave in the way we expected, but some curious noise data was obtained as shown in Fig. 6.37.

As the I-V curve shows (inset of Fig. 6.37), there were three clearly separate transitions observed with roughly equal resistance steps which probably means that each vertical slice goes superconducting separately. The first two transitions were very sharp and especially the first one was difficult to bias on. As seen from the noise data, there was a large noise peak found at the higher transitions. The noise peaks seem to be centered around underlying interference lines that are clearly seen in the lowest transition noise data. The worrying question that arises from the noise feature is: does an external disturbance generate the rather broad and very high noise peak and does the frequency where that happens depend on TES resistance? Looking closely one can see a slight bump in the noise at 1 kHz from the lowest transition. Is that identical to ITFN noise coming from an intermediate block (or similar) or is it caused by the same mechanism as the large peaks at higher resistance and is simply less obvious due to lower α? This might correspond to the anomalous mid-frequency noise discussed in section 6.3.3.

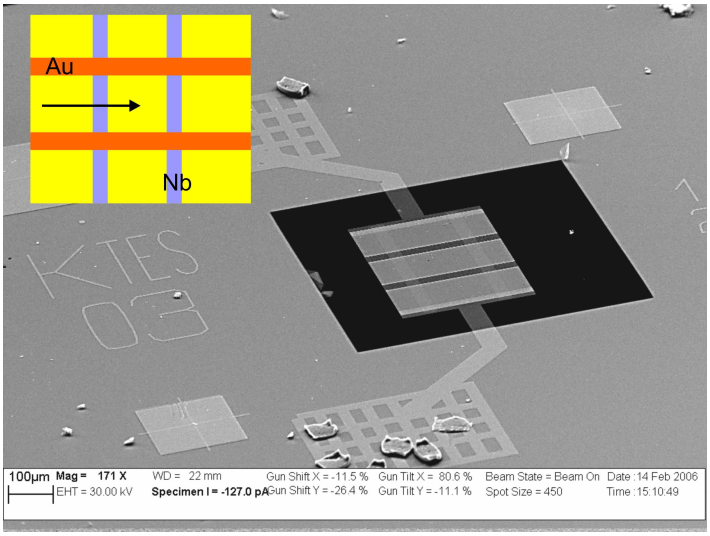

FIGURE 6.36 Scanning electron microscope image of a KTES. The TES film is divided in three sections by Nb strips and extra Au bars extend over the TES parallel to direction of bias current flow, as illustrated in the schematic inset.

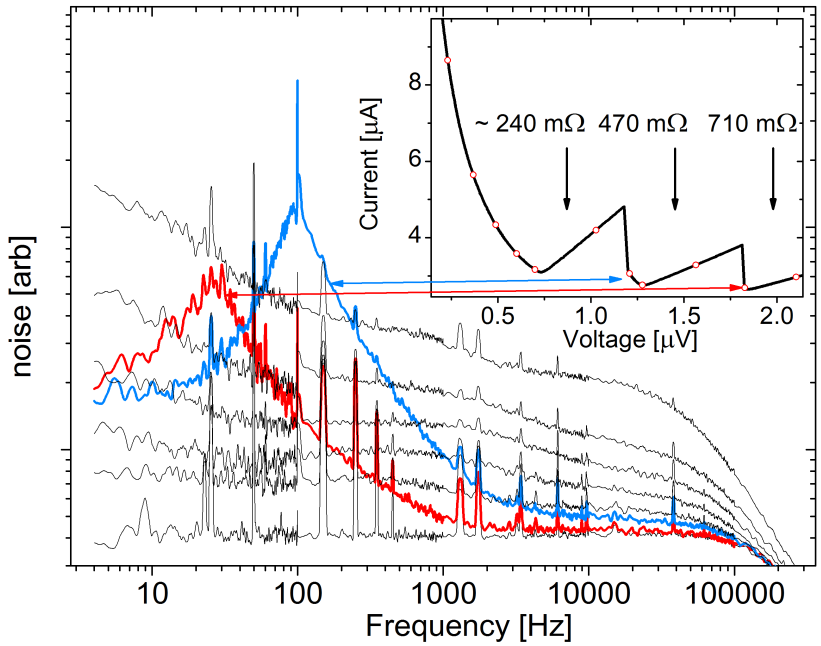

FIGURE 6.37 Measured noise data from a KTES. The interesting features are shown by the red and blue lines and they correspond to points in the I-V curve (inset) as indicated by the arrows.

6.5 SiN properties

6.5.1 Thermal transport mechanism

It can be argued that the thermal transport in a SiN membrane at the TES operating temperatures and film thicknesses at or below 1 μm is not fully understood yet. It is not even exactly clear if the phononic heat transport in the membranes is ballistic or diffusive, or something in between [73,98–102]. Using TES I-V data to extract values for thermal parameters n and K does not necessarily give data on SiN purely. Rather, it may be an effective value that holds for the combination of TES + membrane and includes contribution from electron-phonon coupling or Kapitza boundary resistance. Furthermore, the obtained values are not necessarily constant throughout the transition. If we assume that the membrane is (almost) ballistic, one may wonder how the temperature profile is affected by a TES that is often almost as large as the underlying SiN window. We have seen that for nominally identical membranes, we get scatter in n depending possibly on membrane size, TES design and T_c. So far we have never obtained n = 4 from TES data, although in some cases it has been quite close to that.

We have done experiments using NIS tunnel junctions (Normal metal - Insulator - Superconductor) in a symmetric SINIS configuration as thermometers to measure the thermal conductance of the SiN membranes. Very briefly explained, the tunnel junctions are current biased so that the voltage over them depends on temperature [103]. Once a calibration sweep of voltage against cryostat temperature is performed, we go to a low temperature and use a heater in the middle of the membrane to heat it up and measure the temperature of the SINIS thermometers that are placed at different distances from the heater.

When the SINIS experiment was planned and performed, the assumption was that the SiN membrane would be diffusive. In that case there would be a temperature gradient on the membrane which could be measured and thermal conductivity estimated using that information. Now that the situation looks more complex, the layout of the thermometers, shown in the inset of Fig. 6.38) was not ideal. As was found in Ref. [102, 104], on a mostly ballistic membrane one should use only one thermometer, otherwise the scattering of phonons caused by other structures on the membrane can affect the reading of a SINIS. This effect was also seen in our measurements; when we plotted the temperature of each SINIS versus heater power, the results made little sense (if assuming diffusive transport). However, if we scale the power seen by each thermometer at radius r_i from the heater to be a fraction of the

total radiated power, given by

$$P_{scaled,i} = P_{total} \frac{w}{2\pi r_i} \tag{6.1}$$

where w is the width of a SINIS, we get the result of Fig. 6.38.

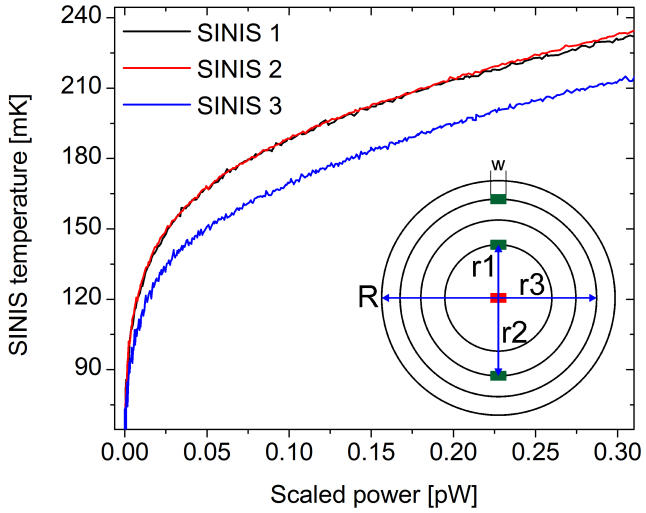

FIGURE 6.38 Results of a measurement where a heater is placed in the middle of a membrane and SINIS thermometers at varying distances from it, as shown in the inset. Membrane is approximated by a circle with radius R. The scaled power is the fraction of emitted total power incident on each thermometer. The SiN membrane used in this measurement was 1 μm thick and was fabricated by MESA.

Now the two thermometers that are on opposite sides of the heater show very good agreement. The third SINIS gives a lower temperature because it does not "see" the power it should. SINIS 1 sits between SINIS 3 and the heater, scattering phonons so that the flux arriving on SINIS 3 is reduced. This result would seem to confirm that the SiN membrane used in this measurement was indeed ballistic. There was some data (not shown) where a SINIS placed on the membrane but very close to bulk Si did not follow the ballistic scaling and would instead show a temperature closer to bath temperature than expected. This can either be caused by error from the approximation of a circular membrane or by the membrane not being fully ballistic. In a partially ballistic case the temperature profile near any edges such as bulk Si or TES is slightly modified as shown in Ref. [105].

Results from other measurements done in Jyväskylä using SINIS thermometers suggest that in the film thickness and temperature ranges used for TES detectors, SiN may actually be in a region where the heat transport is undergoing a transition in dimensionality [102,104]. An interesting theoretical and experimental finding is that by reducing membrane thickness a global minimum in thermal conductance

is reached and for thinner films it starts to increase again [102,106,107]. The effect of membrane thickness on detector speed and resolution was studied theoretically in Ref. [108].

6.5.2 Heat capacity

The heat capacity of the SiN membrane is an essential design parameter. As we have already discussed, it seems to be responsible for the intermediate heat capacity which causes unwanted noise to the system. In our work we have been more interested in the source of the ITFN noise coming from inside the TES itself. Therefore, we have merely accepted that an intermediate heat capacity is there, and that it seems to originate from the membrane but we have not explicitly tried to look for the actual source of it. From results of paper A.VII we can find some information but we refrain from making firm statements at this point. There seems to be consistency in the scaling of the heat capacity with respect to both SiN area and thickness. Compared to an estimated Debye heat capacity, the values obtained from our fits are orders of magnitude higher. A larger than expected heat capacity has been reported by several groups [83,84,109].

6.6 X-ray results

Because our work has concentrated more on studying the physics of transition-edge sensors, we have not really put effort in obtaining X-ray spectra. But a TES exists for the purpose of detecting radiation, so a few times we performed experiments with an X-ray source installed in the cryostat. The problem in our setup has been temperature stability of the cryostat, which makes it difficult to obtain good quality X-ray data. The data shown in this section was measured without proper temperature regulation, but even when regulated, the cryostat temperature has fast fluctuations.

When calculating the energy resolution from the pulse integral, our best result is shown in figure 6.39. Using a moving average over the pulses to detect pulse height resulted in slight improvement to roughly 29 eV at 5.9 keV. The actual resolution is probably better than shown, but due to the unfinished state of our X-ray data analysis software we cannot currently get the most out of our data. For example, we have not used the optimal filter [21,110] which is often found to produce best results.

Perhaps the most useful lesson we can learn from our X-ray data, is by looking at the pulse shapes, and comparing two detectors with different Bi absorbers. The all-Bi, directly on TES version shown in figure 6.39 produced pulses (Fig. 6.40) that

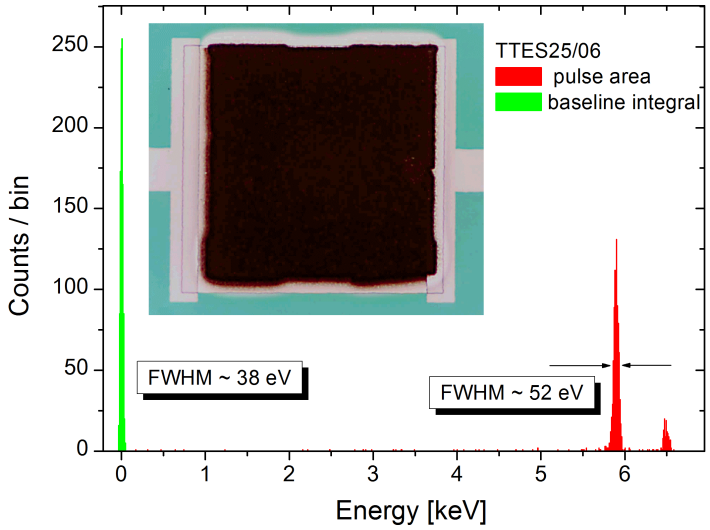

FIGURE 6.39 X-ray spectrum recorded using a TES with a Bi absorber directly on top of the TES (inset). This result was obtained by directly calculating the pulse areas.

had a sharp fast peak in the beginning and then quite a long decay time. We note that similar fast features with Bi absorbers have been reported by others [111]. The TES described in section 6.4.1 had a layer of Cu under Bi and the absorber was contacted to the TES vias Cu pillars. That TES did not have an obviously visible fast peak in the pulses (Fig. 6.41). It was, however, an extremely noisy design and produced even worse energy resolution than the other TES. The conclusion we can draw from the pulse shapes is that the fast feature is likely due to the vertical versus lateral thermalization times of Bi. The lack of the spike when a Cu thermalization layer is present supports our discussion of how to design a good absorber using Bi.

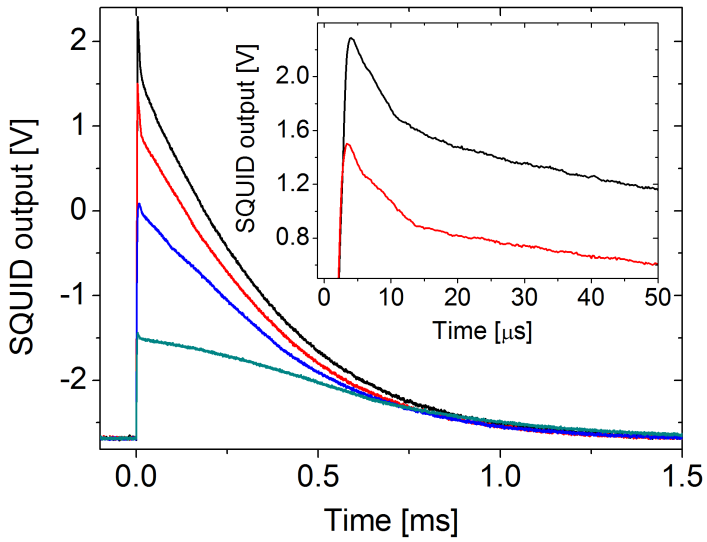

FIGURE 6.40 Recorded X-ray pulses at different bias settings, measured using a TES with a 3 μm Bi absorber directly on top of the TES film. Notice the fast peak at the beginning of the pulse, zoomed in the inset.

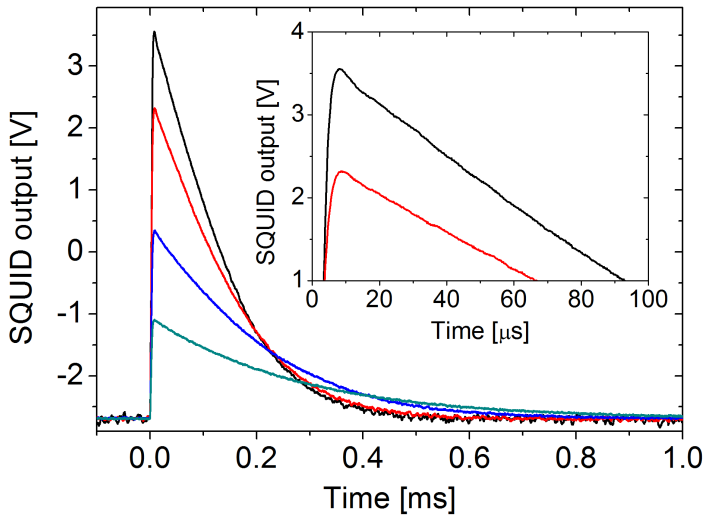

FIGURE 6.41 Recorded X-ray pulses at different bias settings, measured using a TES with a Cu thermalization layer under Bi. Fast peak is greatly reduced or not present at all.

Chapter 7

Summary

The main part of this work concentrates on finding explanations for the excess noise observed in transition-edge sensors. A related effort is the investigation of thermal models that can be probed with the help of noise and complex impedance data. It was found that most of the noise can be explained by internal thermal fluctuation noise, but in some cases unknown noise remained especially when biased low in the transition.

A detector using a novel Corbino-geometry was developed and studied. The CorTES has certain benefits compared to the more common square geometry, such as the possibility to model the transition analytically and being able to control the detector resistance with geometry. In term of modeling, clear separation into normal and superconducting phases is a good thing.

A new theory for excess noise in a CorTES was developed, which was based on correlated critical fluctuations of superconductivity at the boundary between normal and superconducting phases. The application of the FSN theory to other geometries may be possible but difficult to do in practice. Based on a prediction that it should be possibly to reduce the FSN noise level by breaking the TES in parallel slices, two such designs were fabricated and characterized. Instead of correlation between noise and number of slices, it was found that the noise level seemed to depend more on the transition steepness parameter α.

When the measurement of frequency dependent complex impedance was shown by others to be a valuable tool in characterizing TES devices, we also began applying the technique in our experiments. During this work it has become clear to us that in order to explain the measured impedance and noise data of our detectors, a thermal model with at least three bodies is required. A large part of this work was then spent on trying to identify the physical origins of those bodies. An intermediate thermal block related to the Si_3N_4 membrane was found to be one likely component of the model.

One problem in analyzing the complex impedance data has typically been the difficulty in fixing the high frequency limit, Z_∞. Because it would be very helpful to accurately know that value, we came up with a measurement scheme where Z_∞ could be extracted using DC data only. Unfortunately the method is rather sensitive to several parameters and it is uncertain at this point if the method can produce reliable estimates of Z_∞. It could, however, be used in a reverse way to obtain very accurate measurements of the important material dependent thermal parameter, n.

When it became evident that the CorTES data was more complicated than one would expect, we suspected the insulating Al_2O_3 layer used in the CorTES was to blame. We performed measurements on a test structure that proved the assumption correct. Our insulator film was in fact a surprisingly good conductor of heat and in later measurements it was also shown that the heat capacity of the insulator was larger than expected.

The main result of this thesis is the identification of the decoupling between normal and superconducting phases as the source of the large high frequency noise component. The fitted values of heat capacity and (to some degree) thermal conductance from several different geometries followed the predictions of our model. Calculations show that the magnitude of this noise will likely always increase when trying to bias lower in the transition. Our work also indicates design choices that are expected to minimize the noise. Additionally, some of the observed differences between Ti and Mo based detectors can be explained using our model, but we note that further theoretical work is needed.

Bibliography

[1] IRWIN, K. D. AND HILTON, G. C., *Transition-edge sensors*, in *Cryogenic particle detection*, edited by C. Enss, Topics in Applied Physics (Springer, Berlin, 2005).

[2] MEIER, J., EGELHOF, P., FISCHER, C., HIMMLER, A., KIRCHNER, G., KIENLIN, A., KRAUS, G., HENNING, W., AND SHEPARD, K. W., *Energy sensitive detection of heavy ions with transition edge calorimeters*. J. Low Temp. Phys. **93** (1993) 231–238.

[3] HORANSKY, R. D., ULLOM, J. N., BEALL, J. A., HILTON, G. C., IRWIN, K. D., DRY, D. E., HASTINGS, E. P., LAMONT, S. P., RUDY, C. R., AND RABIN, M. W., *Superconducting calorimetric alpha particle sensors for nuclear nonproliferation applications*. Applied Physics Letters **93** (2008) 123504.

[4] ANDREWS, D. H., W. F. BRUCKSCH, J., ZIEGLER, W. T., AND BLANCHARD, E. R., *Attenuated superconductors i. for measuring infra-red radiation*. Rev. Sci. Instr. **13** (1942) 281–292.

[5] ANDREWS, D. H., FOWLER, R. D., AND WILLIAMS, M. C., *The effect of alpha-particles on a superconductor*. Phys. Rev. **76** (1949) 154–155.

[6] CLARKE, J. AND BRAGINSKI, A., *The SQUID handbook: Volume 1: Fundamentals and Technology of SQUIDs and SQUID systems* (Wiley, 2004).

[7] FAGALY, R., *Superconducting quantum interference device instruments and applications*. Rev. Sci. Instr. **77** (2006).

[8] IRWIN, K. D., *An application of electrothermal feedback for high resolution cryogenic particle detection*. Applied Physics Letters **66** (1995) 1998–2000.

[9] IRWIN, K. D., HILTON, G. C., WOLLMAN, D. A., AND MARTINIS, J. M., *X-ray detection using a superconducting transition-edge sensor microcalorimeter with electrothermal feedback*. Applied Physics Letters **69** (1996) 1945–1947.

[10] DUNCAN, W., HOLLAND, W., AUDLEY, D., KELLY, D., PEACOCK, T., HASTINGS, P., MACINTOSH, M., IRWIN, K., NAM, S. W., HILTON, G., DEIKER, S., WALTON, A., GUNDLACH, A., PARKES, W., DUNARE, C., ADE, P., AND ROBSON, I., *Scuba-2: Application of ltd technology*. AIP Conf. Proc. **605** (2002) 577–580.

[11] WIKUS, P., DORIESE, W. B., ECKART, M. E., ADAMS, J. S., BANDLER, S. R., BREKOSKY, R. P., CHERVENAK, J. A., EWIN, A. J., FIGUEROA-FELICIANO, E., FINKBEINER, F. M., GALEAZZI, M., HILTON, G., IRWIN, K. D., KELLEY, R. L., KILBOURNE, C. A., LEMAN, S. W., MCCAMMON, D., PORTER, F. S., REINTSEMA, C. D., RUTHERFORD, J. M., AND TROWBRIDGE, S. N., *The detector and readout systems of the micro-x high resolution microcalorimeter x-ray imaging rocket*. AIP Conf. Proc. **1185** (2009) 434–437.

[12] BAVDAZ, M., BLEEKER, J. A., HASINGER, G., INOUE, H., PALUMBO, G. G., PEACOCK, A. J., PARMAR, A. N., TURNER, M. J. L., TRUEMPER, J. E., AND SCHIEMANN, J., *X-ray evolving universe spectroscopy mission (xeus)* (SPIE, 1999), vol. 3766, pp. 82–93.

[13] WOLLMAN, D., IRWIN, K., HILTON, L., G. AMD DULCIE, NEWBURY, D., AND MARTINIS, J., *High-resolution, energy-dispersive microcalorimeter spectrometer for x-ray microanalysis*. Journal of Microscopy **188** (1997) 196–223.

[14] MILLER, A. J., NAM, S. W., MARTINIS, J. M., AND SERGIENKO, A. V., *Demonstration of a low-noise near-infrared photon counter with multiphoton discrimination*. Applied Physics Letters **83** (2003) 791–793.

[15] HELISTÖ, P., LUUKANEN, A., GRÖNBERG, L., PENTTILÄ, J., SEPPÄ, H., SIPOLA, H., DIETLEIN, C., AND GROSSMAN, E., *Antenna-coupled microbolometers for passive thz direct detection imaging arrays*, in *European Microwave Integrated Circuits Conference, 2006. The 1st* (2006), pp. 35 –38.

[16] BUNKER, G., *Introduction to XAFS* (Cambridge University Press, 2010).

[17] UHLIG, J., *To be published*, Ph.D. thesis, Lund University, Sweden.

[18] JOHANSSON, S., CAMPBELL, J., AND MALMQVIST, K. (eds.), *Particle-induced X-ray emission spectrometry (PIXE)* (John Wiley and Sons, 1995).

[19] REINTSEMA, C. D., BEYER, J., NAM, S. W., DEIKER, S., HILTON, G. C., IRWIN, K., MARTINIS, J., ULLOM, J., VALE, L. R., AND MACINTOSH, M., *Prototype system for superconducting quantum interference device multiplexing of large-format transition-edge sensor arrays*. Rev. Sci. Instr. **74** (2003) 4500–4508.

[20] MATHER, J. C., *Bolometer noise: nonequilibrium theory*. Appl. Opt. **21** (1982) 1125–1129.

[21] MOSELEY, S. H., MATHER, J. C., AND MCCAMMON, D., *Thermal detectors as x-ray spectrometers*. Journal of Applied Physics **56** (1984) 1257–1262.

[22] GALEAZZI, M. AND MCCAMMON, D., *Microcalorimeter and bolometer model*. Journal of Applied Physics **93** (2003) 4856–4869.

[23] MCAMMON, D., *Thermal equilibrium calorimeters - an introduction*, in *Cryogenic particle detection*, edited by C. Enss, Topics in Applied Physics (Springer, Berlin, 2005).

[24] LINDEMAN, M., *Microcalorimetry and the transition-edge sensor*, Ph.D. thesis, University of California at Davis (2000).

[25] FIGUEROA FELICIANO, E., *Theory and development of position-sensitive quantum calorimeters*, Ph.D. thesis, Stanford University (2001).

[26] IRWIN, K. D., HILTON, G. C., WOLLMAN, D. A., AND MARTINIS, J. M., *Thermal-response time of superconducting transition-edge microcalorimeters*. Journal of Applied Physics **83** (1998) 3978–3985.

[27] IRWIN, K., *Thermodynamics of nonlinear bolometers near equilibrium*. Nucl. Instr. and Meth. A **559** (2006) 718 – 720.

[28] BOYLE, W. S. AND JR., K. F. R., *Performance characteristics of a new low-temperature bolometer*. J. Opt. Soc. Am. **49** (1959) 66–69.

[29] HOEVERS, H. F. C., BENTO, A. C., BRUIJN, M. P., GOTTARDI, L., KOREVAAR, M. A. N., MELS, W. A., AND DE KORTE, P. A. J., *Thermal fluctuation noise in a voltage biased superconducting transition edge thermometer*. Journal of Applied Physics **77** (2000) 4422–4424.

[30] KNOEDLER, C. M., *Phase-slip shot noise contribution to excess noise in superconducting bolometers*. Journal of Applied Physics **54** (1983) 2773–2776.

[31] FRASER, G., *On the nature of the superconducting-to-normal transition in transition edge sensors*. Nucl. Instr. and Meth. A **523** (2004) 234 – 245.

[32] LINDEMAN, M., ANDERSON, M., BANDLER, S., BILGRI, N., CHERVENAK, J., CROWDER, S. G., FALLOWS, S., FIGUEROA-FELICIANO, E., FINKBEINER,

F., IYOMOTO, N., KELLEY, R., KILBOURNE, C., LAI, T., MAN, J., MCCAMMON, D., NELMS, K., PORTER, F., ROCKS, L., SAAB, T., SADLEIR, J., AND VIDUGIRIS, G., *Percolation model of excess electrical noise in transition-edge sensors*. Nucl. Instr. and Meth. A **559** (2006) 715 – 717.

[33] CELASCO, E., BAGLIANI, D., CELASCO, M., EGGENHÖFFNER, R., GATTI, F., FERRARI, L., AND VALLE, R., *Correlated avalanches in transition edge sensor noise power spectra*. Journal of Statistical Mechanics: Theory and Experiment **2009** (2009) P01043.

[34] ULLOM, J. N., DORIESE, W. B., HILTON, G. C., BEALL, J. A., DEIKER, S., DUNCAN, W. D., FERREIRA, L., IRWIN, K. D., REINTSEMA, C. D., AND VALE, L. R., *Characterization and reduction of unexplained noise in superconducting transition-edge sensors*. Applied Physics Letters **84** (2004) 4206–4208.

[35] LUUKANEN, A., *High performance microbolometers and microcalorimeters: from 300 K to 100 mK*, Ph.D. thesis, University of Jyväskylä (2003).

[36] ULLOM, J. N., BEALL, J. A., DORIESE, W. B., DUNCAN, W. D., FERREIRA, L., HILTON, G. C., IRWIN, K. D., REINTSEMA, C. D., AND VALE, L. R., *Optimized transition-edge x-ray microcalorimeter with 2.4 ev energy resolution at 5.9 kev*. Applied Physics Letters **87** (2005) 194103.

[37] LITA, A., ROSENBERG, D., NAM, S., MILLER, A., BALZAR, D., KAATZ, L., AND SCHWALL, R., *Tuning of tungsten thin film superconducting transition temperature for fabrication of photon number resolving detectors*. IEEE Trans. Appl. Supercond. **15** (2005) 3528 – 3531.

[38] LUUKANEN, A. AND PEKOLA, J. P., *A superconducting antenna-coupled hot-spot microbolometer*. Applied Physics Letters **82** (2003) 3970–3972.

[39] SILVERT, W., *Theory of the superconducting proximity effect*. J. Low Temp. Phys. **20** (1975) 439.

[40] HEIKKILÄ, T., *Superconducting proximity effect in mesoscopic metals*, Ph.D. thesis, Helsinki University of Technology (2002).

[41] YOUNG, B. A., SAAB, T., CABRERA, B., CROSS, J. J., CLARKE, R. M., AND ABUSAIDI, R. A., *Measurement of t_c suppression in tungsten using magnetic impurities*. Journal of Applied Physics **86** (1999) 6975–6978.

[42] HAUSER, J. J., THEUERER, H. C., AND WERTHAMER, N. R., *Superconductivity in cu and pt by means of superimposed films with lead*. Phys. Rev. **136** (1964) A637–A641.

[43] BRAMMERTZ, G., GOLUBOV, A. A., VERHOEVE, P., DEN HARTOG, R., PEACOCK, A., AND ROGALLA, H., *Critical temperature of superconducting bilayers: Theory and experiment*. Applied Physics Letters **80** (2002) 2955–2957.

[44] PORTESI, C., TARALLI, E., ROCCI, R., RAJTERI, M., AND MONTICONE, E., *Fabrication of au/ti tess for optical photon counting*. J. Low Temp. Phys. **151** (2008) 261–265.

[45] YEFREMENKO, V., WANG, G., NOVOSAD, V., DATESMAN, A., PEARSON, J., DIVAN, R., CHANG, C. L., DOWNES, T. P., MCMAHON, J. J., BLEEM, L. E., CRITES, A. T., MEYER, S. S., AND CARLSTROM, J. E., *Low temperature thermal transport in partially perforated silicon nitride membranes*. Applied Physics Letters **94** (2009) 183504.

[46] RIDDER, M., BRUIJN, M., HOEVERS, H., GERMEAU, A., BAARSA, N., KROUWER, E., VAN BAARB, J., AND WIEGERINK, R., *Thermal design issues and performance of microcalorimeter arrays at sub-kelvin temperatures*, in *Sensors, 2003. Proceedings of IEEE* (2003), vol. 1, pp. 353 – 357 Vol.1.

[47] MOROZOV, D., MAUSKOPF, P. D., ADE, P., BRUIJN, M., DE KORTE, P. A. J., HOEVERS, H., RIDDER, M., KHOSROPANAH, P., DIRKS, B., AND GAO, J.-R., *Ultrasensitive tes bolometers for space based fir astronomy*. AIP Conf. Proc. **1185** (2009) 48–51.

[48] RAI-CHOUDHURY, P. (ed.), *Handbook of Microlithography, Micromachining, and Microfabrication. Volume 1: microlithography* (SPIE-International Society for Optical Engineering, 1997).

[49] THOMPSON, L., WILLSON, C., AND BOWDEN, M. (eds.), *Introduction to microlithography* (American chemical society, 1994), 2nd ed.

[50] FRANSSILA, S., *Introduction to microfabrication* (McGraw-Hill, Singapore, 1996), 2nd ed.

[51] SADLEIR, J. E., SMITH, S. J., ROBINSON, I. K., FINKBEINER, F. M., CHERVENAK, J. A., BANDLER, S. R., ECKART, M. E., AND KILBOURNE, C. A., *Proximity effects and nonequilibrium superconductivity in transition-edge sensors*. Phys. Rev. B **84** (2011) 184502.

[52] LINDEMAN, M. A., BANDLER, S., BREKOSKY, R. P., CHERVENAK, J. A., FIGUEROA-FELICIANO, E., FINKBEINER, F. M., SAAB, T., AND STAHLE, C. K., *Characterization and reduction of noise in mo/au transition edge sensors*. Nucl. Instr. and Meth. A **520** (2004) 348 – 350.

[53] HILTON, G., MARTINIS, J., IRWIN, K., BERGREN, N., WOLLMAN, D., HUBER, M., DEIKER, S., AND NAM, S., *Microfabricated transition-edge x-ray detectors*. IEEE Trans. Appl. Supercond. **11** (2001) 739 –742.

[54] SADLEIR, J. E., SMITH, S. J., BANDLER, S. R., CHERVENAK, J. A., AND CLEM, J. R., *Longitudinal proximity effects in superconducting transition-edge sensors*. Phys. Rev. Lett. **104** (2010) 047003.

[55] KOZOREZOV, A., GOLUBOV, A., MARTIN, D., DE KORTE, P., LINDEMAN, M., HIJMERING, R., AND WIGMORE, J., *Microscopic model of a transition edge sensor as a weak link*. IEEE Trans. Appl. Supercond. **21** (2011) 250 –253.

[56] PALOSAARI, M., *Transition-Edge Sensor Array Development*, Master's thesis, University of Jyväskylä (2009).

[57] ASHCROFT, N. W. AND MERMIN, N. D., *Solid state physics* (Saunders College, 1976).

[58] BANDLER, S., BREKOSKY, R., BROWN, A.-D., CHERVENAK, J., FIGUEROA-FELICIANO, E., FINKBEINER, F., IYOMOTO, N., KELLEY, R., KILBOURNE, C., PORTER, F., SADLEIR, J., AND SMITH, S., *Performance of tes x-ray microcalorimeters with a novel absorber design*. J. Low Temp. Phys. **151** (2008) 400–405.

[59] URL `http://henke.lbl.gov/optical_constants/`.

[60] ZINK, B. L., ULLOM, J. N., BEALL, J. A., IRWIN, K. D., DORIESE, W. B., DUNCAN, W. D., FERREIRA, L., HILTON, G. C., HORANSKY, R. D., REINTSEMA, C. D., AND VALE, L. R., *Array-compatible transition-edge sensor microcalorimeter gamma-ray detector with 42 ev energy resolution at 103 kev*. Applied Physics Letters **89** (2006) 124101.

[61] TINKHAM, M., *Introduction to Superconductivity* (McGraw-Hill, Singapore, 1996), 2nd ed.

[62] KOZOREZOV, A., GOLUBOV, A., MARTIN, D., VERHOEVE, P., AND WIGMORE, J. K., *Proximity effect in tes structures*. AIP Conf. Proc. **1185** (2009) 27–30.

[63] KOZOREZOV, A., *Energy down-conversion and thermalization in metal absorbers*. J. Low Temp. Phys. 1–1210.1007/s10909-011-0426-1, URL http://dx.doi.org/10.1007/s10909-011-0426-1.

[64] INCROPERA, F. AND DEWITT, D., *Fundamentals of heat and mass transfer* (John Wiley and Sons, 1996), 4th ed.

[65] SAAB, T., FIGUEROA-FELICIANO, E., IYOMOTO, N., BANDLER, S. R., CHERVENAK, J. A., KELLEY, R. L., KILBOURNE, C. A., PORTER, F. S., AND SADLEIR, J. E., *Determining the thermal diffusivity in microcalorimeter absorbers and its effect on detector response*. Journal of Applied Physics **102** (2007) 104502.

[66] BROWN, A.-D., BANDLER, S., BREKOSKY, R., CHERVENAK, J., FIGUEROA-FELICIANO, E., FINKBEINER, F., IYOMOTO, N., KELLEY, R., KILBOURNE, C., PORTER, F., SMITH, S., SAAB, T., AND SADLEIR, J., *Absorber materials for transition-edge sensor x-ray microcalorimeters*. J. Low Temp. Phys. **151** (2008) 413–417.

[67] PEKOLA, J. AND KAUPPINEN, J., *Insertable dilution refrigerator for characterization of mesoscopic samples*. Cryogenics **34** (1994) 843 – 845.

[68] POBELL, F., *Matter and Methods at Low Temperatures* (Springer, Germany, 1996), 2nd ed.

[69] LOUNASMAA, O., *Experimental principles and methods below 1 K* (Academic press, 1974).

[70] SEPPÄ, H., KIVIRANTA, M., SATRAPINSKI, A., GRÖNBERG, L., SALMI, J., AND SUNI, I., *A coupled dc squid with low 1/f noise*. IEEE Trans. Appl. Supercond. **3** (1993) 1816.

[71] KIVIRANTA, M. AND SEPPÄ, H., *Dc-squid electronics based on the noise cancellation scheme*. IEEE Trans. Appl. Supercond. **5** (1995) 2146.

[72] CHERVENAK, J. A., IRWIN, K. D., GROSSMAN, E. N., MARTINIS, J. M., REINTSEMA, C. D., AND HUBER, M. E., *Superconducting multiplexer for arrays of transition edge sensors*. Journal of Applied Physics **74** (1999) 4043–4045.

[73] LINDEMAN, M., BARGER, K., BRANDL, D., CROWDER, S., ROCKS, L., AND MCCAMMON, D., *Accurate thermal conductance and impedance measurements of transition edge sensors*. J. Low Temp. Phys. **151** (2008) 180–184.

[74] LINDEMAN, M. A., BANDLER, S., BREKOSKY, R. P., CHERVENAK, J. A., FIGUEROA-FELICIANO, E., FINKBEINER, F. M., LI, M. J., AND KILBOURNE, C. A., *Impedance measurements and modeling of a transition-edge-sensor calorimeter*. Rev. Sci. Instr. **75** (2004) 1283–1289.

[75] LINDEMAN, M. A., BARGER, K. A., BRANDL, D. E., CROWDER, S. G., ROCKS, L., AND MCCAMMON, D., *Complex impedance measurements of calorimeters and bolometers: Correction for stray impedances*. Rev. Sci. Instr. **78** (2007) 043105.

[76] FOLKNER, W. M., MOODY, M. V., RICHARD, J.-P., CARROLL, K. R., AND TESCHE, C. D., *Instrumentation of a resonant gravitational radiation detector with a planar thin-film dc squid*. Journal of Applied Physics **65** (1989) 5190–5196.

[77] PLEIKIES, J., *Strongly coupled, low noise dc-SQUID amplifiers*, Ph.D. thesis, University of Twente, The Netherlands (2009).

[78] LINDEMAN, M., BARGER, K., BRANDL, D., CROWDER, S., ROCKS, L., MCCAMMON, D., AND HOEVERS, H., *The superconducting transition in 4-d: Temperature, current, resistance and heat capacity*. J. Low Temp. Phys. **151** (2008) 190–194.

[79] TAKEI, Y., GOTTARDI, L., HOEVERS, H., DE KORTE, P., VAN DER KUUR, J., RIDDER, M., AND BRUIJN, M., *Characterization of a high-performance ti/au tes microcalorimeter with a central cu absorber*. J. Low Temp. Phys. **151** (2008) 161–166.

[80] BENNETT, D. A., HORANSKY, R. D., AND ULLOM, J. N., *Two-body models for analyzing complex impedance*. AIP Conf. Proc. **1185** (2009) 737–740.

[81] AKAMATSU, H., ISHISAKI, Y., HOSHINO, A., EZOE, Y., OHASHI, T., TAKEI, Y., YAMASAKI, N. Y., MITSUDA, K., OSHIMA, T., AND TANAKA, K., *Impedance measurement of a gamma-ray tes calorimeter with a bulk sn absorber*. AIP Conf. Proc. **1185** (2009) 191–194.

[82] SAAB, T., BANDLER, S., CHERVENAK, J., FIGUEROA-FELICIANO, E., FINKBEINER, F., IYOMOTO, N., KELLEY, R., KILBOURNE, C., LINDEMAN, M., PORTER, F., AND SADLEIR, J., *Determination of complex microcalorimeter parameters with impedance measurements*. Nucl. Instr. and Meth. A **559** (2006) 712 – 714.

[83] ZHAO, Y., APPEL, J., CHERVENAK, J., DORIESE, W., AND STAGGS, S., *Study of excess heat capacity and suppressed kapitza conductance in tes devices*. IEEE Trans. Appl. Supercond. **21** (2011) 227 –231.

[84] GOLDIE, D. J., AUDLEY, M. D., GLOWACKA, D. M., TSANEVA, V. N., AND WITHINGTON, S., *Thermal models and noise in transition edge sensors*. Journal of Applied Physics **105** (2009) 074512.

[85] GOLDIE, D. J., VELICHKO, A. V., GLOWACKA, D. M., AND WITHINGTON, S., *Ultra-low-noise mocu transition edge sensors for space applications*. Journal of Applied Physics **109** (2011) 084507.

[86] OSHIMA, T. AND YOSHITAKE, H., *Optimization method for tes microcalorimeters with absorbers*. IEEE Trans Appl. Supercond. **19** (2009) 465 –468.

[87] LINDEMAN, M., DIRKS, B., VAN DER KUUR, J., DE KORTE, P., DEN HARTOG, R., GOTTARDI, L., HIJMERING, R., HOEVERS, H., AND KHOSROPANAH, P., *Relationships between complex impedance, thermal response, and noise in tes calorimeters and bolometers*. IEEE Trans Appl. Supercond. **21** (2011) 254 –257.

[88] MAASILTA, I., *Impedance and noise of complex thermal models*. To be published .

[89] JETHAVA, N., ULLOM, J., BENNETT, D., IRWIN, K., HORANSKY, R., BEALL, J., HILTON, G., VALE, L., HOOVER, A., BACRANIA, M., AND RABIN, M., *Characterization of thermal cross-talk in a γ-ray microcalorimeter array*. AIP Conf. Proc. **1185** (2009) 34.

[90] IYOMOTO, N., BANDLER, S., BREKOSKY, R., BROWN, A.-D., CHERVENAK, J., FIGUEROA-FELICIANO, E., FINKBEINER, F., KELLEY, R., KILBOURNE, C., PORTER, F., SADLEIR, J., AND SMITH, S., *Heat sinking and crosstalk for large, close-packed arrays of microcalorimeters*. J. Low Temp. Phys. **151** (2008) 506–512.

[91] KOZOREZOV, A., GOLUBOV, A. A., MARTIN, D. D. E., DE KORTE, P. A. J., LINDEMAN, M. A., HIJMERING, R. A., VAN DER KUUR, J., HOEVERS, H. F. C., GOTTARDI, L., KUPRIYANOV, M. Y., AND WIGMORE, J. K., *Modelling the resistive state in a transition edge sensor*. Applied Physics Letters **99** (2011) 063503.

[92] IYOMOTO, N., BANDLER, S. R., BREKOSKY, R. P., BROWN, A.-D., CHERVENAK, J. A., FINKBEINER, F. M., KELLEY, R. L., KILBOURNE, C. A., PORTER, F. S., SADLEIR, J. E., SMITH, S. J., AND FIGUEROA-FELICIANO, E., *Close-packed arrays of transition-edge x-ray microcalorimeters with high spectral resolution at 5.9 kev*. Applied Physics Letters **92** (2008) 013508.

[93] SEIDEL, G. AND BELOBORODOV, I., *Intrinsic excess noise in a transition edge sensor*. Nucl. Instr. and Meth. A **520** (2004) 325 – 328.

[94] POHL, R. O., LIU, X., AND THOMPSON, E., *Low-temperature thermal conductivity and acoustic attenuation in amorphous solids*. Rev. Mod. Phys. **74** (2002) 991–1013.

[95] HOEVERS, H., BRUIJN, M., DIRKS, B., GOTTARDI, L., DE KORTE, P., VAN DER KUUR, J., POPESCU, A., RIDDER, M., TAKEI, Y., AND TAKKEN, D., *Comparative study of tiau-based tes microcalorimeters with different geometries*. J. Low Temp. Phys. **151** (2008) 94–99.

[96] TIEST, W. B., BRUIJN, M., HOEVERS, H., DE KORTE, P., VAN DER KUUR, J., AND MELS, W., *Understanding tes microcalorimeter noise and energy resolution*. Nucl. Instr. and Meth. A **520** (2004) 329 – 332.

[97] BERGMANN TIEST, W., *Energy resolving power of transition-edge X-ray microcalorimeters*, Ph.D. thesis, Utrecht University (2004).

[98] LEIVO, M. M. AND PEKOLA, J. P., *Thermal characteristics of silicon nitride membranes at sub-kelvin temperatures*. Applied Physics Letters **72** (1998) 1305–1307.

[99] HOLMES, W., GILDEMEISTER, J. M., RICHARDS, P. L., AND KOTSUBO, V., *Measurements of thermal transport in low stress silicon nitride films*. Applied Physics Letters **72** (1998) 2250–2252.

[100] HOEVERS, H. F. C., RIDDER, M. L., GERMEAU, A., BRUIJN, M. P., DE KORTE, P. A. J., AND WIEGERINK, R. J., *Radiative ballistic phonon transport in silicon-nitride membranes at low temperatures*. Applied Physics Letters **86** (2005) 251903.

[101] ZINK, B. AND HELLMAN, F., *Specific heat and thermal conductivity of low-stress amorphous si-n membranes*. Solid State Communications **129** (2004) 199 – 204.

[102] KARVONEN, J., *Thermal properties in low dimensional structures below 1 K*, Ph.D. thesis, University of Jyväskylä (2009).

[103] GIAZOTTO, F., HEIKKILÄ, T., LUUKANEN, A., SAVIN, A., AND PEKOLA, J., *Opportunities for mesoscopics in thermometry and refrigeration: Physics and applications*. Rev. Mod. Phys. **78** (2006) 217.

[104] KARVONEN, J., KÜHN, T., AND MAASILTA, I., *Temperature profile for ballistic and diffusive phonon transport in a suspended membrane with a radially symmetric heat source*. Chin. Journal Phys. **49** (2011) 435.

[105] KLITSNER, T., VANCLEVE, J. E., FISCHER, H. E., AND POHL, R. O., *Phonon radiative heat transfer and surface scattering*. Phys. Rev. B **38** (1988) 7576–7594.

[106] KÜHN, T. AND MAASILTA, I., *Ballistic phonon transport in dielectric membranes*. Nucl. Instr. and Meth. A **559** (2006) 724.

[107] KÜHN, T. AND MAASILTA, I., *Maximizing phonon thermal conductance for ballistic membranes*. Journal of Physics: Conference Series **92** (2007) 012082.

[108] MAASILTA, I. AND KÜHN, T., *Effect of thin ballistic membranes on transition-edge sensor performance*. J. Low Temp. Phys. **151** (2008) 64.

[109] KENYON, M., DAY, P., BRADFORD, C., BOCK, J., AND LEDUC, H., *Heat capacity of absorbers for transition-edge sensors suitable for space-borne far-ir/submm spectroscopy*. IEEE Trans. Appl. Supercond. **19** (2009) 524.

[110] WHITFORD, C., TIEST, W. B., AND HOLLAND, A., *Practical considerations in optimal filtering of tes signals*. Nucl. Instr. and Meth. A **520** (2004) 592 – 594.

[111] MORITA, U., YAMAKAWA, Y., FUJIMORI, T., ISHISAKI, Y., OHASHI, T., TAKEI, Y., YOSHIDA, K., YOSHINO, T., MITSUDA, K., YAMASAKI, N., FUJIMOTO, R., SATO, H., MINOURA, Y., TAKAHASHI, N., HOMMA, T., SHOJI, S., KURODA, Y., AND ONISHI, M., *Evaluation of 256-pixel tes microcalorimeter arrays with electrodeposited bi absorbers*. Nucl. Instr. and Meth. A **559** (2006) 539 – 541.